

AN ABSTRACT OF THE THESIS OF

Diane L. Foster for the degree of Doctor of Philosophy in Civil Engineering
presented on June 13, 1996.

Title: Dynamics of the Nearshore Wave Bottom Boundary Layer

Redacted for Privacy

Abstract approved: _____


Robert A. Holman

This thesis presents an examination of the nearshore wave bottom boundary layer under conditions of significant sediment response. Using both field observations and simple models, the response of the bottom boundary layer to random waves is shown to have a complex behavior. First, the linearized wave bottom boundary layer governing equation is solved with a transformation of the cross-shore velocity to a distorted spatial domain, resulting in an analytic expression for the temporal and vertical structure of the cross-shore velocity under an arbitrary wave field. Model predictions of the bed shear velocity are in good agreement with laboratory measurements. The model is limited by assuming zero velocity at a fixed bed and that turbulence generation is solely due to bottom shear.

Next, a comprehensive set of near bed cross-shore velocity, sediment suspension, and bed elevation observations, collected in 2 m water depth on the North Carolina coast, are presented. The observations show a cross-shore velocity structure which decays with increasing proximity to the bed as predicted by simple theory. Bottom shears based on rms amplitude decay and time-averaged phase shifts are lower than model predictions and may be indicative of more rapid mixing of momentum than assumed in the above model. Also, frequency-dependent estimates of the phase and amplitude vertical structure show a nonlinear response of the wave bottom boundary layer over the incident band. Through most flow phases, estimates of turbulent kinetic energy increase linearly from the bed, however under large wave crests, enhanced turbulence levels are observed and are well correlated to active sediment suspension events. Estimates of dissipation rates are significantly less than those observed in an actively breaking surf zone wave, and

significantly greater than those observed in ocean boundary layers, and continental shelf current boundary layers.

Finally, an Oregon coast field experiment showed an intermittent high frequency velocity variance structure which was correlated to suspended sediment events. A linear shear instability analysis determined that during the period of flow reversal there exists a potential for generating turbulence due to shear instabilities of the vertical structure of cross-shore velocity.

**Dynamics of the Nearshore
Wave Bottom Boundary Layer**

by

Diane L. Foster

A THESIS

submitted to

Oregon State University

in partial fulfillment of
the requirements for the
degree of

Doctor of Philosophy

Completed June 13, 1996

Commencement June 1997

Doctor of Philosophy Thesis of Diane L. Foster
presented on June 13, 1996

APPROVED:

Redacted for Privacy

Major Professor representing Civil Engineering

Redacted for Privacy

Chair of the Department of Civil Engineering

Redacted for Privacy

Dean of Graduate School

I understand that my thesis will become part of the permanent collection of Oregon State University Libraries. My signature below authorizes release of my thesis to any reader upon request:

Redacted for Privacy

Diane L. Foster, Author

ACKNOWLEDGMENTS

As I think about my time at Oregon State, I am struck with how truly fortunate I am to have been involved with so many terrific individuals. First and foremost, I'd like to thank Rob Holman for serving as my chief mentor over these five years. I'm not sure if Rob realized exactly how challenging it would be to teach this engineer to think, but I hope he realizes how much I gained from the experience. Reg Beach gets the credit for proposing to do this work and for setting a great example of how to bring the data home. Also much thanks to my committee members: Dr. Sollitt, who served as my chief liaison with the ocean engineering group and has provided numerous good ideas over the years, Dr. Yim and Bill Lunch. In addition to my committee, I'd like to acknowledge two individuals who have also made significant contributions to both me and my work: Ed Thornton has served as a surrogate advisor/father-figure/cheerleader during my visits to NPS and Ron Guenther has repeatedly given me appreciation for mathematics and encouragement for womankind.

Much thanks to Jim Moum for his patient insight into the turbulence world, Dick Sternberg for his wisdom in the field, adjectively-challenged Mike Freilich for his uncompromising science, and Tony Bowen for knowing the answer (but not telling before I try and figure it out). The NPS gang (Ed, Tim Stanton, Tom Herbers, and all the rest) graciously adopted me by providing space, resources, and hospitality during my numerous (and what they likely thought to be lengthy) visits with Tom in Monterey. More recently, the hospitality of Edie Gallagher, and Michele Okihiro (sorry about mokumanu) have made my visits to Scripps productive, most of the time. The CIL folks (Todd, John, Nathaniel, Mike, Hilary, Eric, Kathy, Kathelijne, and Amanda) certainly get the award for experiencing me at my dumbest, messiest, and least coherent and I will certainly miss them more than they will miss me (or my dirty clothes). Specifically, I'll miss the science talks with and statistics education by Todd and Nathaniel, watching Hilary come into her own, discovering the SGI tools with Hilary and Kathy, waiting for Eric to do the things he does (and Amanda to point those things out), and watching John be a nice guy (when he thinks no one is looking). Without the technical expertise, teasing, and humor of John Stanley, Tom Leach, Chuck Sears, Bruce Marler, Curt Vandetta, the FRF staff, Rex Johnson, Marica Turnbull, and Sue Pullen my time at OSU would have been infinitely more difficult and significantly less interesting. In learning to collect field data, and fall onto the frontiers of science, I have come across numerous individuals not mentioned above and who for various reasons ought to be acknowledged: Andrea Ogston (for being my field roommate, cohort, and good friend), Casey Church (for being Casey), Alex Hay (for asking tough questions and being a formidable sparring partner), John Allen and Bob Hudspeth (for

toughening me up), Priscilla Newberger (for her time and interest), Dan Hanes (for hints on determining the thermal conductivity of sediment-laden fluids), Doug Caldwell (for recalling his boundary layer days), Mark Lorang (for his sensitive Montanan geologist ways), Peter Howd (for his big-brotherly pestering), Nick Pias, and Ricardo Letelier, (for their hallway bantering) and Jack Barth (for teaching me how to tie a taut line hitch in 60 seconds).

My numerous engineering buddies (Simo, Bill, John, Chrispy, Mark (Chester), Crystal, Joyce, and Leslie) have kept me in touch with the real world and provided motivation for me to stay in school. Following in Tom's footsteps, I have had the honor to mooch meals and good times from the greatest bunch of people I know: Shiela and Nathaniel (and Kathryn), Sue and Jim (and Ed), Carrie, Mark and Vicki (and Ian and Maddy), Irene, Lynn, my 'way-cool' roomies Pete and Cait, the Monday night Burger Crew, and Peter and Kathryn Howd (who I didn't get the opportunity to mooch from, but I'm sure I would have if they were in town). When I first saw the garbage in her car five years ago, I knew Carrie Walch and I were destined to become good friends, I thank her for the Relative Kink Instability, occasional attitude adjustments, and Punda. Shiela's haircuts, chocolate chip cookies, child rearing tips, and analysis sessions will certainly be missed. While in Monterey, Tom and I have had the good fortune of finding great friends in Tom Herbers, and Ad (and Stella) Reniers. My co-FOB, Dave Murray, and the rest of the Salmon Fly fishermen have provided numerous laughs and good times over the past few years. Leaving town is easier knowing that Big Red will be in Sue's great hands.

Beyond all the folks mentioned above, the folks to whom I am most indebted to are my family (Mom, Dad, Kim, Gram, Unc, Aunt Brenda, Kris, and Amy): I never realized how truly fortunate we (Amy, Kris, Kim, and I) are to have been able to grow up with such a fantastic family until I moved 'out west'. I'd like to acknowledge: the family matriarch, better known as Gram, for being the best human alarm clock a granddaughter could ask for, Kim for her warped sense of humor and tell-it-like-she-sees-it way, Mom for her fun loving and supportive nature, and Dad for helping form the core of who I am and what I stand for. I am honored to have a part of each of you in me. Fortunately for me, my family circle has increased over the past few years by the addition of the Lippmann family. I hope they realize how much their home-away-from-home and distinctive sense of humor means to me. Finally, until I met Tom, I never thought I would find someone who could fish with the best, provide a last minute edit on a paper, have such notable taste in fashion, make me laugh at the drop of a dime, and be my best friend and husband.

This dissertation was supported by funding from the Office of Naval Research, Coastal Sciences Program, and from a fellowship by the American Society for Engineering Education. Special thanks to Mark Abbott for making available the IBM RS6000 SP computer provided by an IBM Shared University Research Project grant.

TABLE OF CONTENTS

CHAPTER I: GENERAL INTRODUCTION	1
CHAPTER II: AN ANALYTIC SOLUTION TO THE WAVE BOTTOM BOUNDARY LAYER GOVERNING EQUATION UNDER RANDOM WAVE FORCING.....	5
Abstract.....	5
II-1. Introduction	5
II-2. Governing Equation.....	7
II-3. Solution	8
II-4. Shear Velocity Formulation	14
II-5. Results and Discussion.....	15
II-6. Conclusions.....	33
CHAPTER III: RESPONSE OF THE WAVE BOTTOM BOUNDARY LAYER TO SURF ZONE WAVE CONDITIONS: OBSERVATIONS AND MODEL EVALUATIONS.....	35
Abstract.....	35
III-1. Introduction.....	35
III-2. Models	37
III-2.1 WBBL Theory	37
III-2.2 WBBL Velocity under a Single Monochromatic Wave.....	38
III-2.3 WBBL Theory under a Random Wave Field	38
III-3. Observations.....	40
III-3.1 Deployment.....	40
III-3.2 Instrumentation.....	40
III-3.3 Hot Film Calibration and Data Quality	44

Table of Contents, Continued

III-4. Results.....	49
III-4.1 Evidence of the WBBL.....	49
III-4.2 Statistical Boundary Layer Scalings	54
III-4.3 Frequency Structure	63
III-5. Conclusion.....	64
CHAPTER IV: OBSERVATIONS OF TURBULENCE IN THE NEARSHORE WAVE BOTTOM BOUNDARY LAYER	68
IV-1. Introduction	68
IV-1.1 Motivation.....	68
IV-1.2 Objectives	70
IV-2. Observations	70
IV-3. Results	73
IV-3.1 Concentration.....	75
IV-3.1 Shear Stress.....	75
IV-3.1 Turbulent Kinetic Energy	78
IV-3.1 Dissipation Rate	82
IV-4. Conclusions	86
CHAPTER V: SEDIMENT SUSPENSION EVENTS AND SHEAR INSTABILITIES IN THE BOTTOM BOUNDARY LAYER	88
Abstract	88
V-1. Introduction	88
V-2. Theory	89
V-3. Model Formulation	92
V-4. Field Study	94
V.4.1 Location.....	94
V.4.1 Hot Film Calibration.....	95

Table of Contents, Continued

V-5. Results and Discussion	95
V-6. Summary	101
CHAPTER VI: CONCLUSIONS	103
BIBLIOGRAPHY	105
APPENDICES	107
Appendix A.....	108
Appendix B.....	111
Appendix C.....	114

LIST OF FIGURES

<u>Figure</u>	<u>Page</u>
II.1	Sketch of the boundary layer structure..... 9
II.2	Sketch of the transformed boundary layer structure..... 11
II.3	Temporal and spatial structure of predicted cross-shore velocity for the first four modes: a) input free stream velocity, U_∞ ; b) temporal amplitude, $a_n(t)$; c) spatial eigenfunction, $\Psi_n(z)$; $T=5$ s, $u_o=100$ cm/s, $z_o=0.1$ cm, $d=20$ cm, number of spatial steps =501. 16
II.4	Predicted cross-shore velocity, $u(z,\theta)$ at several wave phase: a) $0^\circ < \theta < 180^\circ$; b) $180^\circ < \theta < 360^\circ$ 17
II.5	Predicted velocity, $\partial u/\partial z$ at several wave phase: a) $0^\circ < \theta < 180^\circ$; b) $180^\circ < \theta < 360^\circ$ 18
II.6	a) Series convergence is assumed when the rms of a given mode amplitude ($a_{n,rms}$) is less than 1% of the rms of the first mode amplitude ($a_{1,rms}$), $a_{n,rms}/a_{1,rms} < 1\%$. b) Solution convergence is assumed when the rms deviation of the bed shear velocity between two consecutive iterations $((u_{*oi}-u_{*oi-1})_{rms})$ is less than 1% of the rms of the first iteration (u_{*orms}), $(u_{*oi}-u_{*oi-1})_{rms}/u_{*orms} < 1\%$ 20
II.7	Comparison between (—) model and (...) measured [Jonsson and Carlsen, 1976] cross-shore velocities over the wave phase..... 21
II.8	Good agreement is shown between the rms velocity calculated a) over the elevation at each wave phase, $u_{rms}(\theta) \pm u_{rmsd}(\theta)$; and b) over the wave phase at each elevation, $u_{rms}(z) \pm u_{rmsd}(z)$; (*) model results and (°)measurements [Jonsson and Carlsen, 1976]..... 22
II.9	The bed shear velocity, u_{*o} , over the wave phase: (o) measurements; and (—) model. 23
II.10	Bed shear velocity, , for each of the three cases: (—) Case 1, $u_o=100$ cm/s, $T=5$ s; (- -) Case 2, $u_o=50$ cm/s, $T=5$ s; (- · -) Case 1, $u_o=100$ cm/s, $T=10$ s; 24
II.11	Energy density spectra for each of the three cases at three elevations: Case 1, $u_o=100$ cm/s, $T=5$ s; Case 2, $u_o=50$ cm/s, $T=5$ s; Case 1, $u_o=100$ cm/s, $T=10$ s..... 27

List of Figures, Continued

<u>Figure</u>	<u>Page</u>
II.12 The predicted amplitude of the first harmonic of velocity (top panel). The predicted relative amplitude of the third (middle panel) and fifth (bottom panel) harmonics to the first harmonic.	28
II.13 Frequency domain EOF of the cross-shore velocity at the first (top panels), third (middle panels), and fifth (bottom panels) harmonic of velocity: a-c) amplitude; d-f) phase.	29
II.14 Four separate input wave velocities (top panel) and the model predicted bed shear velocity (middle panels).	31
II.15 Distribution of a) rms free stream acceleration, $(\partial u_{\infty}/\partial t)_{rms}$; b) predicted relative bed velocity of the third harmonic, $u(3)/u(1)$; c) rms bed shear velocity, u^*_{rms} ; d) relative net suspended sediment transport $\langle u_{\infty} \tau_0 u_{\infty} \rangle / \rho g$; over free stream velocity skewness and asymmetry values ranging from 0 to 0.6 and 0 to 1.2, respectively.	32
III.1 Photo of instrumentation deployment, Aug 94, (Photo courtesy of Bill Birkemeier).	43
III.2 Diagram of cantilever and instrumentation.	44
III.3 Coherence and phase between the calibrated derectified cross-shore velocity as measured by hot film sensors 1-4 (—) and cross-shore velocities as measured by the electromagnetic current meter (- -).	47
III.4 Comparison of the cross-shore velocities as measured by the electromagnetic current meter (EMCM) and the calibrated, derectified cross-shore velocities as measured by hot film sensors (HF1-HF4)	48
III.5 Time varying mean velocity at five elevations above the bed over consecutive 128 second windows (top panel).	50
III.6 A 2 minute time series of the derectified calibrated velocity as measured by 4 hot film anemometers within the wave bottom boundary layer and in the free stream as measured by an EMCM.	51
III.7 An example 20 second time series of the near bed velocities showing the amplitude decay and phase lead in the lower sensors which is consistent with the simple wave bottom boundary layer theory.....	52
III.8 Vertical structure of low passed cross-shore velocity at the five 0.25 s intervals (I, II, III, IV, V) as specified in Figure 8.	53

List of Figures, Continued

<u>Figure</u>	<u>Page</u>
III.9 Energy density spectra as a function of frequency over segments A (top) and C (bottom).....	55
III.10 The root mean square (rms) velocity over each segment (A-E) of the data (o), the Smith model (- -) and the FGH model (—).	56
III.11 A 30 second time series of velocity (top panel) and concentration (bottom panel) showing a temporary bed fluidization under several crests.	57
III.12 The time lag at maximum correlation between the EMCM and each HF over each segment (A-E) of the data, the Smith model and the FGH model.	61
III.13 The ratio of the shear length scale to the boundary layer thickness, (top panel) boundary layer thickness (middle panel), and bed shear velocity (bottom panel), of the rms velocities of the two regression models and two WBBL models for each segment (A-E).	62
III.14 The complex domain empirical orthogonal function (CEOF) of the cross spectral matrix at several frequencies within the wave frequency band.....	65
IV.1 An example 60 second time series near bed cross-shore velocity as measured by four hot film anemometers and the free stream velocity as measured by the EMCM (top panel); high frequency VITA velocity variance at four elevations above the bed (middle panel); and concentration at 4 elevations above the bed (bottom panel).	72
IV.2 The phase space distribution of free stream velocity versus acceleration from 295 to 315 seconds.	74
IV.3 The phase space average distribution of concentration versus the sensor elevation of the five 256 second WBBL segments.	76
IV.4 The phase space average distribution of shear stress versus the sensor elevation of the five 256 second WBBL segments.	79
IV.5 The phase space average distribution of velocity energy density spectrum at 4 cm above the bed versus frequency during one 256 second record.	80
IV.6 The phase space average distribution of frequency slopes versus the sensor elevation of the five 256 second WBBL segments.	81
IV.7 The phase space average distribution of turbulent kinetic energy versus the sensor elevation of the five 256 second WBBL segments.....	83

List of Figures, Continued

<u>Figure</u>	<u>Page</u>
IV.8 The phase space average distribution of energy dissipation rate versus the sensor elevation of the five 256 second WBBL segments.	85
V.1 Oscillatory velocities as a function of height above the bed for phase angles from 0° to 360°.	90
V.2 Boundary layer geometry showing the three regions of the linear analysis.	93
V.3 Sketch of instrumentation deployment on 26 Sept 93, shows the configuration of 3 OBS concentration sensors(C1, C2, & C3), 3 ducted impeller current meters (SM1, SM2, & SM3), 2 Hot Film Anemometers (HF1 & HF 2), 1 electromagnetic current meter(EM1),.....	95
V.4 Five minute time series, as recorded on 26 Sept 93, of: a)velocity at SM1 and EM1 b)speed at SM1 (rectified) c)speed at HF1 and HF2 d)variance partitioned at HF1 e)variance partitioned at HF2 f)concentration at C1 g)concentration at C2.	97
V.5 One minute time series, as recorded on 26 Sept 93, of: a)velocity at SM1 and EM1 b)speed at SM1 (rectified) c)speed at HF1 and HF2 d)variance partitioned at HF1 e)variance partitioned at HF2 f)concentration at C1 g)concentration at C2.	98
V.6 Velocity versus acceleration of 0.5 Hz filtered EM1 sensor at the initiation of: a)suspended sediment events & b)variance events.	99
V.7 Time series as recorded on 26 Sept 93 of: a)velocity of EM1 & boundary layer model approximation of EM1 b)predicted growth rates c)variance partitioned at HF2 d)concentration at C1.	100
A-1 The relative increase in output voltage of theoretical hot film probe in seawater and sediment with given concentration to output voltage in seawater only at zero fluid speed (top panel) and the relative increase in output voltage of theoretical hot film probe in seawater and sediment with given concentration to output voltage in seawater only at each speed (bottom panel).	113

LIST OF TABLES

<u>Table</u>	<u>Page</u>
II-1 Input wave period, T, and amplitude, u_0 , conditions and rms free stream velocity, $(u_\infty)_{rms}$, and rms acceleration, $(\frac{\partial u_\infty}{\partial t})_{rms}$, for three independent wave cases. Also given is the characteristic boundary layer thickness and shear velocity as predicted by the Smith model and the rms, mean, and maximum bed shear velocity as predicted by the model presented in this paper.	25
III-1 Hot film calibration coefficients, α and β , for each hot film sensor. The F statistic between the logarithmic transfer function and each hot film sensor yields significance levels of at least 97% in sensors 1-4.....	46
III-2 Depth root mean square deviations between two models (u_{FGH} and u_S) and the data (u_D) $z=z\pm\Delta z$ of the rms velocity in the five segments A-E. $z-\Delta z$ indicates the sensor array is Δz closer to the bed and $z+\Delta z$ indicates the sensor array is Δz away from the bed.....	59
III-3 Depth averaged temporal root mean square deviations between the FGH model (u_{FGH}) and the data (u_D) $z=z\pm\Delta z$ of the time varying velocity in the five segments A-E. $z-\Delta z$ indicates the sensor array is Δz closer to the bed and $z+\Delta z$ indicates the sensor array is Δz away from the bed	60
B-1 Assumed physical properties of seawater and sediment. ϕ is the relative sediment volume and ϕ is the relative sediment weight. (* Cheng and Vachon, 1970; ** CRC Handbook of Physics and Chemistry).....	112

DYNAMICS OF THE NEARSHORE WAVE BOTTOM BOUNDARY LAYER

CHAPTER I: GENERAL INTRODUCTION

As deep water waves propagate over the ocean towards a beach they eventually reach a depth where they will be significantly transformed by the bottom topography. This region of the coastal oceans is called the nearshore. The evolving fluid motions which are being transformed by the bottom topography are simultaneously transforming this same topography. This nonlinear feedback between the fluid motions and the topography occur over several spatial and temporal scales. Coastlines change over tens of kilometers and decades, while sandbars change on the order of 100 meters and weeks. The smallest recognized fluid-sediment interactions is that of fluid turbulence and sediment suspension occurring over scales of 1-10 cm and 10^{-3} - 10^{-1} s. The work presented here will exclusively focus on these smallest scales.

Sediment transport is commonly partitioned into two separate mechanisms, bed load and suspended load [Bagnold, 1963]. Bed load is defined as the fraction of the total load which is in continuous contact with the bed and consequently is only a few grain diameters thick. Suspended load is the fraction of sediment which is sustained by fluid turbulence and is not in contact with the bed. Thus far, investigations of sediment transport have largely focused on the suspended load transport [Jaffe *et al.*, 1984; Huntley and Hanes, 1987; Hanes, 1988; Beach and Sternberg, 1992]. Surprisingly, research has so far been unable to show a direct link between the surface gravity waves and the sediment suspensions [Beach and Sternberg, 1992]. The wave bottom boundary layer (WBBL) is the region of fluid where the flow is in transition from potential flow due to surface gravity waves to no flow at the bed. Its thickness is limited by the oscillatory motion of the wave and scales as the bed shear velocity over the wave frequency (u_* / ω) [Smith, 1977; Grant and Madsen, 1979]. In the surf zone, where waves are assumed to be vertically uniform, WBBL scales are generally of order 10 cm or less. Because the WBBL is the physical link between the sea bed and the water column, its role in the sediment suspension process is crucial. The momentum required to suspend sediment must be diffused within it and sediment is subsequently suspended through it. Intuition suggests that suspension events should be correlated to the turbulence introduction into the near bed region. The generation of these turbulence events may be attributed to bottom shear, shear instabilities

of the wave bottom boundary layer, and/or downward advection of surficial turbulence associated with wave breaking processes.

By definition, the boundary layer is the region of fluid which is affected by the velocity shear produced at a boundary. The many years of research have been motivated by the need to understand processes such as flow over an airfoil, the convective heat transfer of a fin, and the exchange of momentum and energy at the atmosphere ocean interface. The present investigation was motivated by the need to understand the role of the wave bottom boundary layer in the sediment suspension process.

Theoretical investigations of the oscillatory boundary layer began with the laminar flow solution [Batchelor, 1967], which suggest that the cross-shore velocity will undergo an amplitude decay and a phase shift within the layer. Subsequent investigations considered turbulent flow with vertically varying mixing and rough beds [Smith, 1977; Grant and Madsen, 1979]. More recent investigations have incorporated rippled sea beds [see review by Sleath, 1990], more detailed turbulence modelling [Justesen, 1988], and random waves [Beach and Sternberg, 1992]. These improvements are motivated by the need to adequately predict the bottom boundary layer dynamics in the coastal ocean environment.

The controlled environment of the laboratory makes tank studies attractive for fundamental oscillatory bottom boundary layer observations. One of the first, and perhaps most referenced wave bottom boundary layer study is that of Jonsson and Carlsen [1976]. They examined the temporal and vertical structure of a monochromatic oscillatory bottom boundary layer. More recently, laboratory investigations addressed the turbulence variations over a smooth bed under monochromatic surface waves [Hino *et al.*, 1983; Jensen *et al.*, 1989]. While these laboratory studies contribute to our understanding of wave bottom boundary layer (WBBL) under monochromatic waves, the extrapolation of these studies to a natural random sea, environment has not yet been achieved. A comprehensive review of experimental and theoretical wave bottom boundary layer studies by Sleath [1990], concluded that the paucity of field data have forced theoretical evaluations to rely solely on laboratory measurements and that the conclusions based on these comparisons will probably require substantial modification as field data becomes available.

Because of the energetic and transitory nature of the surf zone, incident and turbulent wave bottom boundary layer velocity observations are much less easily obtained than their laboratory counterparts and limited by the need to find non-intrusive, high frequency response, durable instrumentation. However, in recent years the success in making these field WBBL measurements has increased. Using hot film anemometers and visual observations, Conley and Inman [1992] identified stages in the development of the

fluid-granular boundary layer. Conley and Inman concluded that observed asymmetries in the fluid-granular boundary layer development were not directly related to asymmetries in the free stream wave velocity. WBBL observations on a dissipative Oregon beach showed that observed sediment suspension and turbulence variance events primarily occurred during the transition between offshore and onshore flow [Foster *et al.*, 1994]. Both of these investigations highlight the complex and presently unpredictable response of the wave bottom boundary layer to skewed and asymmetric surface waves in the natural environment. The first field observations of the WBBL vertical structure are given in Trowbridge and Agrawal [1995]. Using a vertical profiling Laser Doppler Velocimeter, they examined two realizations of the wave bottom boundary layer cross-shore velocity structure due to 9 s waves with a free stream root mean square (rms) wave velocity of 10 cm/s. In the cross-shore direction, the observed velocities showed an increase in phase lead and a slight decrease of variance with increasing proximity to the bed. They concluded that the observed scales were characteristic of simple theoretical wave bottom boundary models.

The objective of this thesis is to contribute to an improved understanding of the vertical and temporal structure of the wave bottom boundary layer. Chapter II presents an analytical solution to the linearized wave bottom boundary layer equation. The model predicts the vertical and temporal incident wave band cross-shore velocity structure within the wave bottom boundary layer. Turbulent closure is achieved with a time varying eddy viscosity. Weakly nonlinear interactions at the bed result in a transfer of energy to the odd harmonics. The solution is valid for a uniform known bottom roughness and a random free stream wave velocity. Work done on the sea bed by the flow is shown to increase with increasing free stream wave skewness. The amount of energy transferred to the odd harmonics is shown to increase with both increasing free stream wave skewness and asymmetry. This chapter will be submitted to Coastal Engineering and will be co-authored by Dr. Ron Guenther, who provided guidance on the mathematical solution, and Dr. Rob Holman, who provided advice on all chapters of this thesis.

Field observations from a North Carolina coast experiment are used to evaluate the dynamics and energetics of the incident and turbulent frequency bands. In Chapter III, observations and two simple models are used to investigate the amplitude and phase structure of the incident band dynamics of the WBBL, and evaluate the theoretical scalings of boundary layer thickness, bed shear velocity, and bottom roughness. The predicted shear velocity length scale of the observations is an order of magnitude less than the boundary layer thickness estimates. In Chapter IV, the turbulent band motions are investigated. The turbulent band energy is shown to evolve over the wave phase. The

evolution of the turbulent kinetic energy, dissipation, and shear production over the wave phase is compared with simple estimates of stress and observations of sediment concentration. In addition to Dr Holman, Dr Reg Beach provided guidance on the collection and interpretation of the observations and is a co-author on both of these chapters

In Chapter V, a potential mechanism for the generation of turbulence through a shear instability is investigated. A linear shear instability analysis of modelled temporally varying cross-shore velocity vertical structure is completed to determine if and when small perturbations become unstable. The time series of predicted growth rates of unstable perturbations are compared with sediment concentration observations made with optical back scatter sensors and high frequency velocity variance measurements made with near bed hot film anemometers all obtained during an Oregon coast experiment. The wave bottom boundary layer shear instability is found to be a plausible mechanism for the generation of turbulence. This chapter appeared in the Coastal Dynamics, 1994, conference proceedings and was co-authored with Dr. Reg Beach and Dr. Rob Holman.

Finally, conclusions are summarized in Chapter six.

CHAPTER II: AN ANALYTIC SOLUTION TO THE WAVE BOTTOM BOUNDARY LAYER GOVERNING EQUATION UNDER RANDOM WAVE FORCING

Abstract

Existing models of the wave bottom boundary layer have focused on the vertical and temporal dynamics associated with monochromatic forcing. While these models have made significant advances, they do not address the more complicated dynamics of random wave forcing, commonly found in natural environments such as the surf zone. In this solution, the eddy viscosity is assumed to vary temporally with the bed shear velocity and linearly with depth; however, the solution technique is valid for any eddy viscosity which is separable in time and space. A transformation of the cross-shore velocity to a distorted spatial domain leads to time independent boundary conditions, allowing for the derivation of an analytic expression for the temporal and vertical structure of the cross-shore velocity under an arbitrary wave field. Model calculations of the bed shear velocity are in good agreement with laboratory measurements made by Jonsson and Carlsen (1976). A variety of monochromatic, skewed, and asymmetric wave forcing conditions, characteristic of those found in the surf zone, are used to evaluate the relative effects on the bed shear. Because the temporal variation of the eddy viscosity is assumed proportional to the bottom shear, a weakly nonlinear interaction is created, and a fraction of the input monochromatic wave energy is transferred to the odd harmonics. For a monochromatic input wave, the ratio of the third harmonic of velocity at the bed to the first is less than 10%. However, for a skewed and asymmetric input wave, this ratio can be as large as 30% and is shown to increase with increasing root-mean-square input wave acceleration. The work done by the fluid on the bed is shown to be a maximum under purely skewed waves and is directed onshore. Under purely asymmetric waves, the work done is significantly smaller and directed offshore.

II-1. Introduction

The region of fluid near a boundary is termed the boundary layer and has been the subject of much research over this past century. The importance of the boundary layer has been recognized in fields ranging from aeronautical engineering to oceanography. In wave dominated coastal environments, the wave bottom boundary layer plays an important role in the suspension and transport of sediment (Beach and Sternberg, 1992) and in the estimation of bottom friction for mean currents (Grant and Madsen, 1979; Haines and

Sallenger, 1994; Trowbridge and Agrawal 1994). Because the flow reverses each half wave period and the introduction of turbulence is unsteady, traditional unidirectional flow boundary layer solution techniques are not valid.

Historically, turbulent wave bottom boundary layer models have been forced with monochromatic waves and have approximated Reynolds stresses with time invariant eddy viscosity models as is done in unidirectional steady turbulent boundary layers (Grant and Madsen, 1979; Smith, 1977). Trowbridge and Madsen, 1984b, (herein TM84) included the second harmonic along with the fundamental frequency in the free stream forcing and a time and depth dependent eddy viscosity model. A semi-analytic solution for an oscillatory boundary layer due to monochromatic tidal fluctuations considering a time and depth dependent separable eddy viscosity model is presented by Lavelle and Mojfeld (1983). In Lavelle and Mojfeld, a solvable boundary value problem results from transforming a monochromatic cross-shore velocity to a time distorted coordinate system, whereas the solution technique presented here transforms the cross-shore velocity to a distorted spatial domain. Each of these models yield reasonable comparisons with monochromatic laboratory data. However, extensions to the coastal zone require a solution for a spectrum of skewed and asymmetric waves which produces an unsteady introduction of turbulence.

One of the first wave bottom boundary layer models to consider a spectrum of waves is that of Beach and Sternberg (1992, herein, BS92). Over each half wave period, specified by consecutive zero-crossings, the eddy viscosity is assumed time invariant and depth dependent. Consecutive 256 sec blocks of the free stream velocity are decomposed into spectral components. Smith's (1977, herein S77) monochromatic time invariant eddy viscosity model is forced with each spectral component over each half-wave period and linear superposition is used to reconstruct the complete solution. Similar spectral decomposition's have been performed by Madsen and Wikramanayake (1991). These models succeed in estimating the vertical structure of horizontal velocity under random waves, however, nonlinearities due to turbulent mixing as well as variations in turbulent mixing within a wave cycle are neglected.

One- and two- equation fully numerical turbulent kinetic energy models for monochromatic waves are reviewed in Fredsoe and Diegaard (1992). These models highlight the need for time and depth dependent turbulent mixing parameterization. Al-Salem (1994) compared the friction factor for numerical mixing length models and one equation and two equation models and found only minimal differences, implying that simple mixing length models are relatively robust. While the one and two equation models show much promise, they are currently used only in modelling simple monochromatic waves.

This paper presents an analytic solution to the governing equation of the wave bottom boundary layer dynamics under random wave forcing assuming a separable time and depth dependent eddy viscosity. Section 2 presents the equations governing the fluid dynamics in this near bed region. In section 3, the time-dependent upper boundary condition is mapped through the domain, creating a new, well-posed, solvable, initial, boundary value problem. The separation of variables technique is applied, resulting in an analytic solution for the vertical and temporal structure of the wave bottom boundary layer cross-shore velocity. The time-dependent component of the eddy viscosity is formulated in section 4. The results and discussion are presented in section 5 and the conclusions are given in section 6.

II-2. Governing Equation

The linearized one dimensional time-dependent governing equation for the wave bottom boundary layer is (TM84; S77):

$$\frac{\partial \hat{u}}{\partial t} - \frac{du_{\infty}}{dt} = \frac{1}{\rho} \frac{\partial \tau_{zx}}{\partial z}, \quad (\text{II-1})$$

where \hat{u} is the cross-shore velocity within the domain, u_{∞} is the free stream cross-shore velocity at the top of the domain, t is time, and z is the vertical coordinate (positive upward from the bed). The turbulent stress, τ_{zx} , is represented with an eddy viscosity model with

$$\tau_{zx} = \rho \nu_t \frac{\partial \hat{u}}{\partial z}, \quad (\text{II-2})$$

where ν_t is the eddy viscosity. The boundary and initial conditions are defined as

$$\hat{u}(d, t) = u_{\infty}, \quad (\text{II-3b})$$

$$\hat{u}(z_o, t) = 0, \text{ and} \quad (\text{II-3b})$$

$$\hat{u}(z, t_o) = \hat{r}(z), \quad (\text{II-3c})$$

where d is the upper bound of the domain and is greater than δ , the boundary layer thickness, z_o is the bed roughness, t_o is the initial time, and $\hat{r}(z)$ is the initial condition. A sketch of the boundary layer structure is shown in Figure II.1. The bed roughness is assumed to be known and time independent. An alternative free stream boundary condition of $\frac{\partial \hat{u}(d, t)}{\partial z} = 0$ may also be used; the derivation is presented in appendix A and is analogous to the one used here. Because of the second order nature of the boundary condition in the second formulation, transients take longer to decay and therefore the formulation presented below is recommended.

For the conditions of this solution technique to be met, the turbulent mixing coefficient, or eddy viscosity, must depend on independent characteristic length and time scales, and is modelled as

$$v_t = p(z)g(t), \quad (\text{II-4})$$

where $p(z)$ and $g(t)$ contain the vertical and temporal component of the eddy viscosity, respectively. As is historically done, we consider the specific case when the eddy viscosity is defined as the product of a temporally varying velocity scale and linearly varying length scale,

$$v_t = \kappa u_* z, \quad (\text{II-5})$$

such that $p(z)=z$ and $g(t)=\kappa u_* (t)$ and where κ is the Von Karman's constant and u_* is the time-dependent shear velocity at the bed($z=z_o$). The eddy viscosity model assumes that the generation of turbulence in the boundary layer occurs at the bed, and scales with the distance from the bed. We note that the solution technique presented here is not restricted to this particular selection of eddy viscosity model and that any separable model for the eddy viscosity may be used. The substitution for p and g will not be made until needed.

II-3. Solution

The time-dependent random nature of the free stream velocity at the upper boundary condition limits the available mathematical solution techniques. To circumvent this limitation, we map the upper time-dependent boundary condition through the domain, transforming the governing equation to eliminate the time dependency of the upper boundary condition. The transformation is defined with

$$u = \hat{u} - \left(\frac{z - z_o}{d - z_o} \right) u_\infty, \quad (\text{II-6})$$

where u is the transformed cross-shore boundary layer velocity. Inserting (II-6) into (II-1), the governing equation and boundary and initial conditions become

$$\frac{\partial u}{\partial t} - \frac{d-z}{d-z_o} \frac{du_\infty}{dt} = \frac{\partial}{\partial z} \left(v_t \frac{\partial u}{\partial z} \right) + \frac{\partial v_t}{\partial z} \frac{u_\infty}{d-z_o}, \quad (\text{II-7})$$

$$u(d,t) = 0, \quad (\text{II-8a})$$

$$u(z_o,t) = 0, \text{ and} \quad (\text{II-8b})$$

$$u(z,t_o) = r(z) = \hat{r}(z) - \frac{z - z_o}{d - z_o} u_\infty(t_o), \quad (\text{II-8c})$$

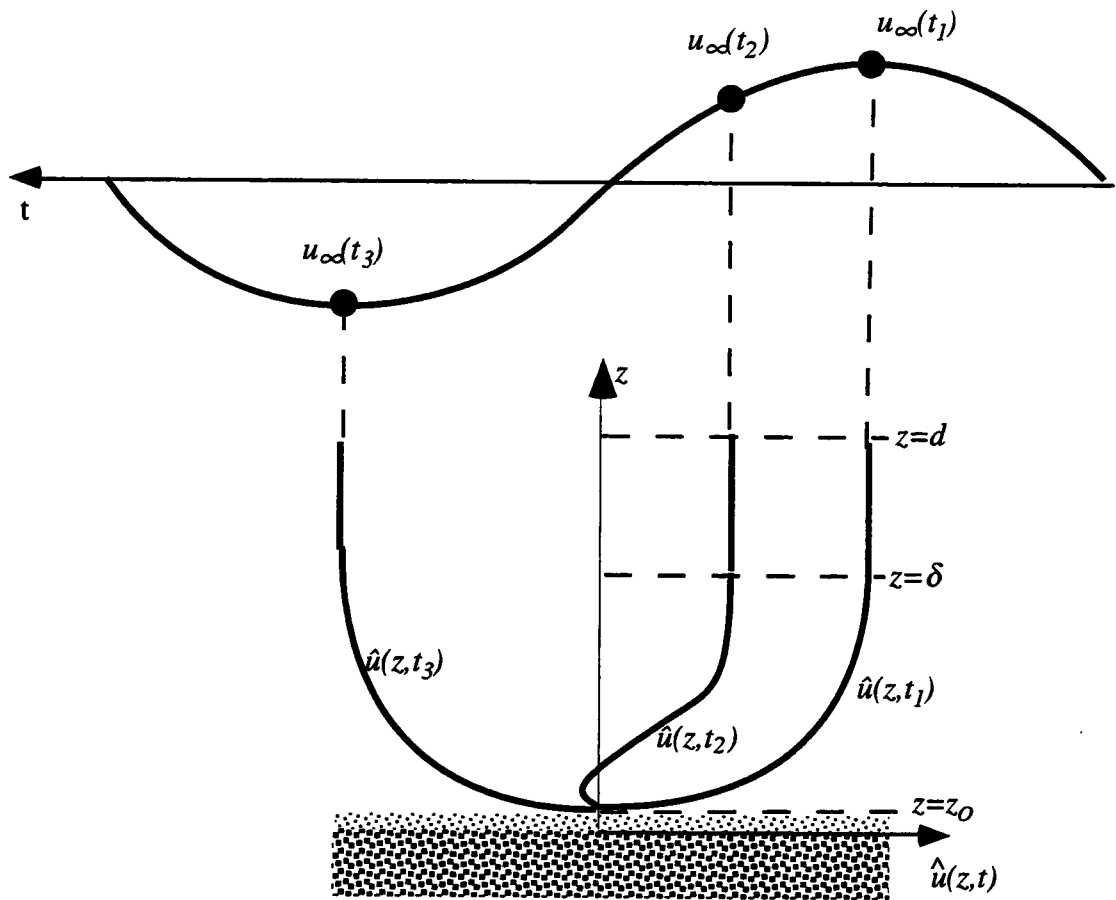


Figure II.1. A sketch of the wave bottom boundary layer structure beneath a monochromatic wave at three instants in time: t_1 , beneath the wave crest, t_2 during decelerating onshore flow, and t_3 , beneath the wave trough.

where $r(z)$ is the transformed initial condition. The added forcing terms in (II-7) result from mapping the upper boundary condition through the domain. This new governing equation is separable, Figure II.2 shows an illustration of the transformed velocity.

To solve (II-7), the homogeneous terms are moved to the left hand side and forcing terms to the right,

$$\frac{\partial u}{\partial t} - g \frac{dp}{dz} \frac{\partial u}{\partial z} - pg \frac{\partial^2 u}{\partial z^2} = \frac{d-z}{d-z_0} \frac{du_\infty}{dt} + g \frac{u_\infty}{d-z_0} \frac{dp}{dz} \quad (\text{II-9})$$

The homogeneous equation is

$$\frac{\partial u_p}{\partial t} - p'(z)g(t) \frac{\partial u_p}{\partial z} - p(z)g(t) \frac{\partial^2 u_p}{\partial z^2} = 0, \quad (\text{II-10})$$

$$u_p(d, t) = 0, \quad (1\text{II-1a})$$

$$u_p(z_0, t) = 0, \text{ and} \quad (\text{II-11b})$$

$$u_p(z, t_0) = r(z), \quad (\text{II-11c})$$

where $u_p = \Psi(z)T(t)$, is the particular solution to the homogeneous equation and is solved with the separation of variables technique. (II-10) becomes

$$\frac{\dot{T}}{gT} = \frac{p\Psi'' + p'\Psi'}{\Psi} = -\lambda^2 \quad (\text{II-12})$$

where $(\dot{})$ is the derivative with respect to time, (\prime) is the derivative with respect to z and λ is the separation constant. (II-12) is represented by two ordinary differential equations

$$\dot{T} + \lambda^2 gT = 0, \text{ and} \quad (\text{II-13a})$$

$$p\Psi'' + p'\Psi' + \lambda^2\Psi = 0. \quad (\text{II-13b})$$

The unique solution for (13a) is

$$T = Ae^{-\lambda^2 \int_0^t g(\tau) d\tau}, \quad (\text{II-14})$$

where A is an integration constant.

$\Psi(z)$ is determined by substituting for p with the previous assumption, $p(z)=z$, into (II-13b), leading to

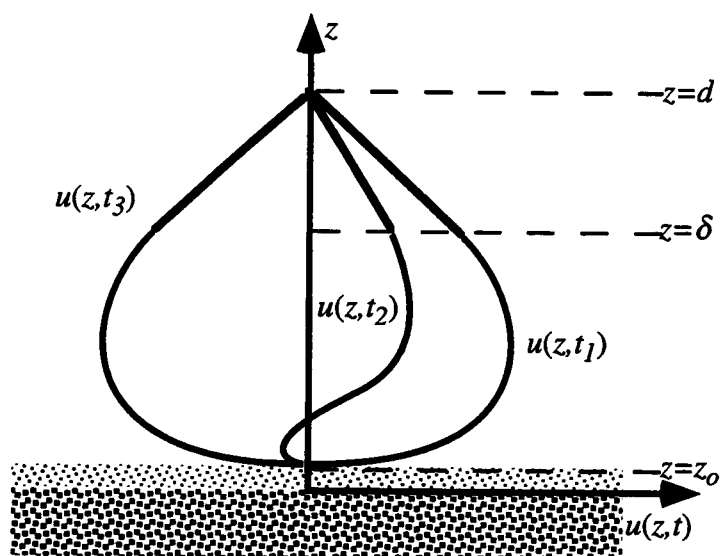


Figure II.2. A sketch of the transformed boundary layer structure at 3 instants in time corresponding to those of Figure II.1.

$$\begin{aligned}
z\Psi'' + \Psi' + \lambda^2\Psi &= 0 \\
\Psi(z_0) &= 0 \\
\Psi(d) &= 0
\end{aligned} \tag{II-15}$$

If the vertical structure of the eddy viscosity, $p(z)$, is arbitrary, a numerical solution may be required for Ψ , but is attainable. The solution for the vertically linear eddy viscosity problem is given by zeroth order Bessel functions of the first (J_0) and second kinds (Y_0)

$$\Psi = B_1 J_0(2\lambda z^{1/2}) + B_2 Y_0(2\lambda z^{1/2}), \tag{II-16}$$

where B_1 and B_2 are integration constants and are determined from the lower boundary condition. The upper boundary condition requires that the eigenvalues, λ_n , satisfy

$$J_0(2\lambda_n z_0^{1/2}) Y_0(2\lambda_n d^{1/2}) - J_0(2\lambda_n d^{1/2}) Y_0(2\lambda_n z_0^{1/2}) = 0. \tag{II-17}$$

The complete homogeneous solution becomes

$$u_p(z, t) = \sum_{n=1}^{\infty} b_n \left(Y_0(2\lambda_n z_0^{1/2}) J_0(2\lambda_n z^{1/2}) - J_0(2\lambda_n z_0^{1/2}) Y_0(2\lambda_n z^{1/2}) \right) e^{-\lambda_n^2 \int_0^t g(\tau) d\tau}, \tag{II-18}$$

where the new integration constants, b_n are

$$b_n = \frac{1}{c_n} \int_{z_0}^d r(z) \Psi_n(z) dz, \tag{II-19}$$

and the constant c_n satisfies the orthogonality condition below

$$\int_{z_0}^d \Psi_n(z) \Psi_j(z) dz = \begin{cases} 0 & \text{if } j \neq n \\ c_n & \text{if } j = n \end{cases}. \tag{II-20}$$

After the particular solution (II-18) is determined from the homogeneous equations, the non homogeneous equation are determined. Rearranging (II-7) to

$$\frac{\partial u}{\partial t} = \frac{\partial}{\partial z} \left(v_i \frac{\partial u}{\partial z} \right) + F(z, t), \tag{II-21}$$

where the forcing term, $F(z, t)$ is the right hand side of (II-9) and is a function of the free stream acceleration and velocity

$$F(z, t) \equiv \frac{d-z}{d-z_0} \frac{du_{\infty}}{dt} + g(t) \frac{u_{\infty}}{d-z_0}. \tag{II-22}$$

(II-21) is solved by assuming a series solution for the velocity of the form

$$u(z,t) = \sum_{n=1}^{\infty} a_n(t) \Psi_n(z), \quad (\text{II-23})$$

where the eigenfunction, Ψ_n , is known from (II-16), and $a_n(t)$ are the amplitude functions which are determined by substituting (II-23) into (II-21)

$$\sum_{n=1}^{\infty} \dot{a}_n \Psi_n = g \sum_{n=1}^{\infty} a_n (p \Psi_n')' + F(z,t). \quad (\text{II-24})$$

Furthermore, assume F may also be represented with a series solution as

$$F(z,t) = \sum_{n=1}^{\infty} F_n(t) \Psi_n(z), \quad (\text{II-25})$$

and F_n is determined with

$$F_n(t) = \frac{1}{c_n} \int_{z_0}^d F(z,t) \Psi_n(z) dz. \quad (\text{II-26})$$

Because $\Psi_n(d)=0$ and $\Psi_n(z_0)=0$, this definition for F will result in discontinuities at $z=d$ and $z=z_0$. Providing that the spatial step is small, and an adequate number of modes are considered, the effects of this discontinuity will be minimal.

After substituting (II-25) into (II-24) and eliminating Ψ_n , (II-24) simplifies to

$$\dot{a}_n(t) + \lambda_n^2 g(t) a_n(t) = F_n(t) \quad (\text{II-27})$$

Multiply (27) by $e^{\lambda_n^2 \int_0^t g(\tau) d\tau}$ and combine the left hand side into one derivative with respect to time

$$\frac{d}{dt} \left\{ e^{\lambda_n^2 \int_0^t g(\tau) d\tau} a_n(t) \right\} = F_n(t) e^{\lambda_n^2 \int_0^t g(\tau) d\tau}. \quad (\text{II-28})$$

Integrate (II-28) with respect to time to obtain an expression for the amplitude function

$$a_n(t) = a_n(0) e^{-\lambda_n^2 \int_0^t g(\tau) d\tau} + \int_0^t F_n(\sigma) e^{-\lambda_n^2 \int_0^t g(\tau) d\tau} d\sigma \quad (\text{II-29})$$

where the initial condition, $a_n(0)=b_n$, given in (II-19). The first term in (II-29) is the transient component which depends on the initial condition and decays to zero after the initial time, t_0 . The second term in (II-29) is a weighted sum of the forcing. The weights represent a time history of the mixing for each mode. The time history term decays with time lag and the decay rate increases with increasing bed shear velocity.

The complete solution to (II-1) is

$$\hat{u}(z,t) = \sum_{n=1}^{\infty} a_n(t) \Psi_n(z) + \frac{z - z_0}{d - z_0} u_{\infty}. \quad (\text{II-30})$$

where

$$\Psi_n(z) = Y_o(2\lambda_n z_o^{1/2})J_o(2\lambda_n z^{1/2}) - J_o(2\lambda_n z_o^{1/2})Y_o(2\lambda_n z^{1/2})$$

(II-30) is the complete solution to the governing equation for the bottom boundary layer under an arbitrary random wave field. Although the vertical dependence of the eddy viscosity, $p(z)$, has been specified as linear, no assumptions have been made about the free stream forcing or the time-dependent nature of the turbulent mixing. The time-dependent component of the eddy viscosity, $g(t)$ is formulated in the next section.

II-4. Shear Velocity Formulation

Recall from (II-5), the time-dependent component of the eddy viscosity is assumed to be $g(t) = \kappa u_*$. Here the shear velocity, u_* , is defined with the equation

$$u_* \equiv \sqrt{\frac{\tau}{\rho}}. \quad (\text{II-31})$$

Combining (II-2) and (II-31), the shear velocity becomes

$$u_* = kz \left| \frac{\partial u}{\partial z} \right|. \quad (\text{II-32})$$

At the bed, the shear velocity becomes (Townsend, 1976)

$$u_{*o}(t) = \kappa z_o \left| \frac{\partial u}{\partial z} \right|_{z=z_o}. \quad (\text{II-33})$$

Initially, $\left| \frac{\partial u}{\partial z} \right|_{z=z_o}$ is unknown and u_* is initialized, following S77 and BS92, with a constant stress boundary layer, assuming $u_* \neq f(z)$. Integrating (II-32) over the depth yields

$$\hat{u}(z, t) = \frac{u_{*o}(t)}{k} \ln \left(\frac{z}{z_o} \right). \quad (\text{II-34})$$

By assuming the velocity outside the boundary layer and boundary layer thickness are known, the first estimate of the shear velocity at the bed is given by

$$u_{*o}(t) = \frac{\kappa u_{\infty}(t)}{\ln \left(\frac{\delta(t)}{z_o} \right)} \quad (\text{II-35})$$

where δ is the boundary layer thickness. For the initial iteration, the boundary layer thickness and shear velocity at time t are assumed to be constant over each half wave period, as specified by zero crossings of the given free stream velocity (BS92) and the solution is determined by iterating on

$$\delta = \frac{u_{*o\text{ peak}}}{2\omega} \quad (\text{II-36a})$$

and

$$u_{*o\text{ peak}} = \frac{Ku_o}{\ln\left(\frac{\delta}{z_o}\right)} \quad (\text{II-36b})$$

where u_o is the peak amplitude of the free stream velocity at each half wave zero crossing.

After the first iteration of the complete solution, the velocity gradient at the bed is determined and, a new fully time-dependent u_{*o} is calculated directly from (II-33). The complete solution is iterated until u_{*o} converges.

II-5. Results and Discussion

The solution for the time and depth dependent velocities in the wave boundary layer is given by (II-30). Unless otherwise specified, the investigations presented here will assume the following parameter specifications: 1) the lower boundary of the domain, given by the bottom roughness, z_o , is assumed to be 0.1 cm and 2) the upper boundary must be at least as large as the boundary layer thickness and will be assumed to be 20 cm. For numerical efficiency, both course and fine time steps are used. The course time step was chosen as 1/8 sec to resolve the temporal structure of U_∞ and u_{*o} . For each independent mode, a finer time step which resolves the integrand in (II-29) with 100 steps is determined, yielding an equivalent numerical accuracy for each mode. The initial condition $\hat{u}(z, t_o) = \hat{r}(z)$ is approximated with a logarithmic profile (II-34)

$$\hat{r}(z) = \frac{u_{*o\text{ max}}(t_o)}{k} \ln\left(\frac{z}{z_o}\right)$$

and $r(z)$ is calculated directly from (II-8c). For increased resolution in the near bed region, the vertical spatial grid is defined with a log transform. The maximum number of modes governs the spatial resolutions.

Figure II.3 shows the vertical structure of the eigenfunctions and the temporal variations of amplitude for the first 4 modes of a 5 sec monochromatic wave with a 100 cm/s amplitude, a typical ocean wave often observed in nature. The relative amplitude of the higher modes increases during the period of flow reversal, when the boundary layer structure deviates from the simple logarithmic structure. The complete boundary layer cross-shore velocity, u , and velocity shear, $\partial u/\partial z$, profiles at several wave phases are given in Figures II-4 and II-5, respectively. Higher modes continue to be included until the variance of the amplitude function for a particular mode is less than 1% of the variance of

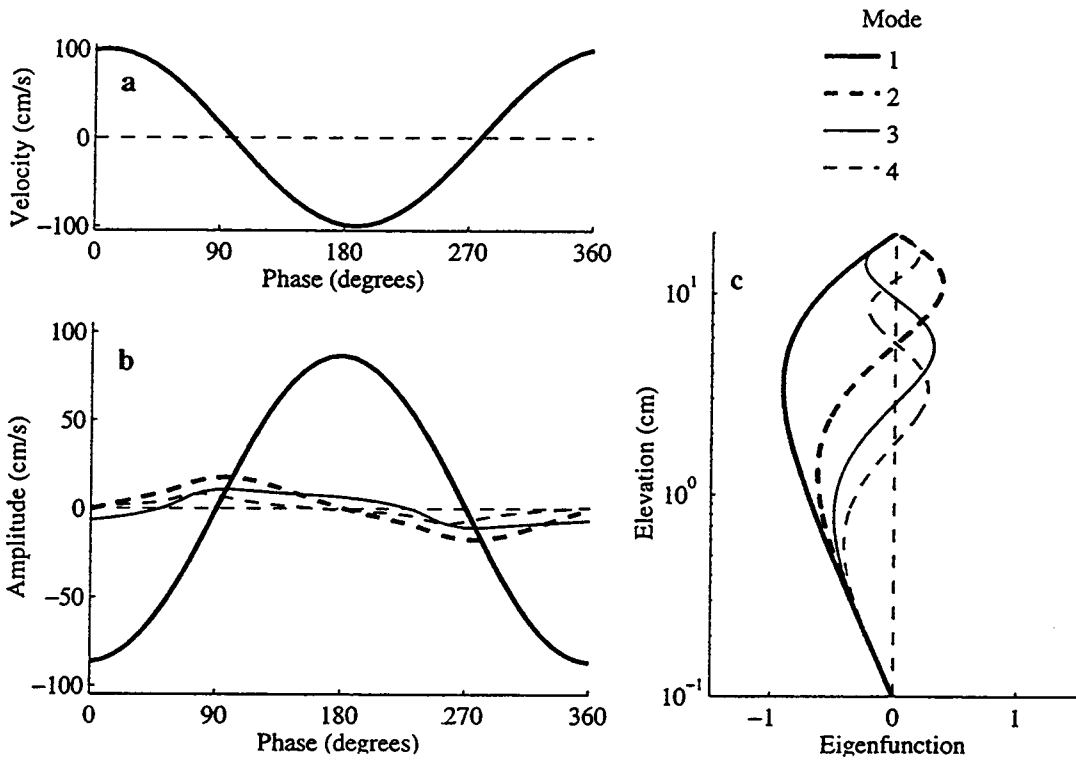


Figure II.3. Temporal and Spatial structure of predicted cross-shore velocity for the first four modes: a) input free stream velocity, U_∞ ; b) temporal amplitude, $a_n(t)$; c) spatial eigenfunction, $\Psi_n(z)$; $T=5$ s, $u_o=100$ cm/s, $z_o=0.1$ cm, $d=20$ cm, number of spatial steps =501.

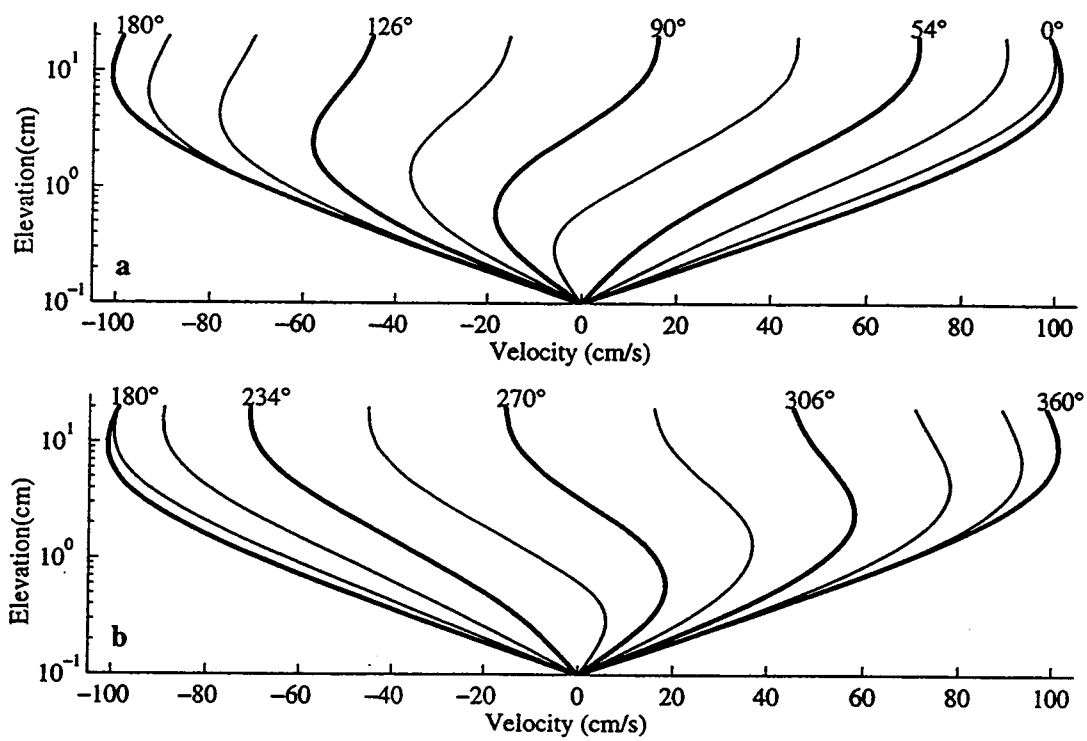


Figure II.4. Predicted cross-shore velocity, $u(z, \theta)$ at several wave phase: a) $0^\circ < \theta < 180^\circ$; b) $180^\circ < \theta < 360^\circ$.

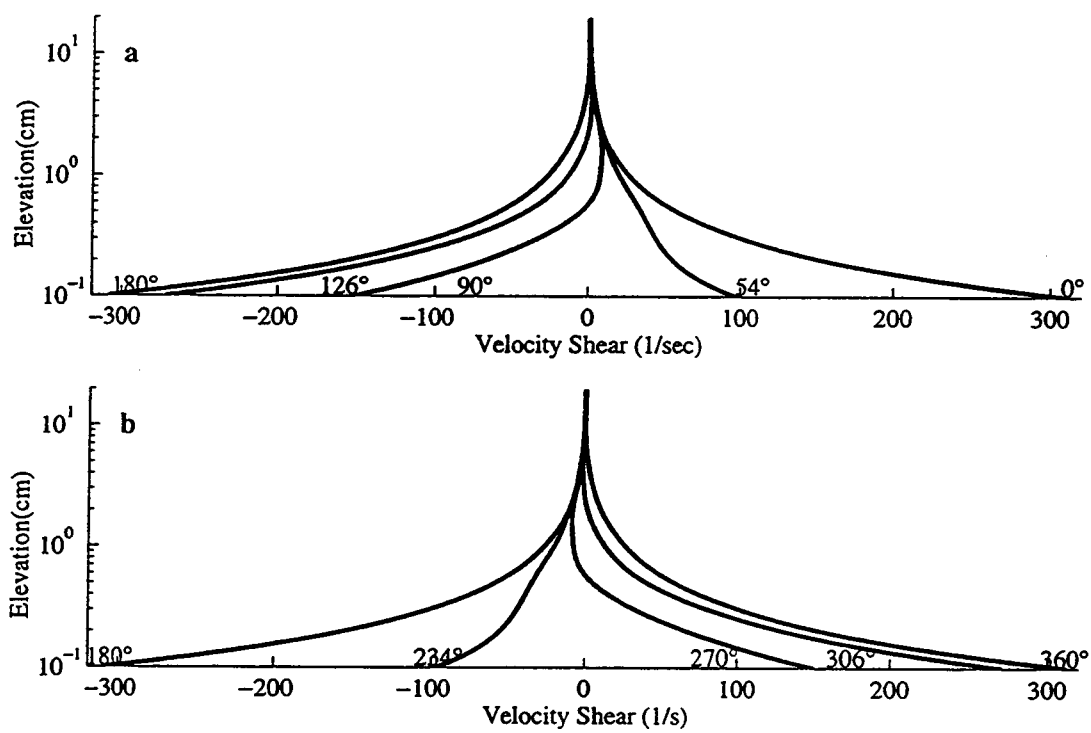


Figure II.5. Predicted velocity shear, $\partial u/\partial z$ at several wave phases: a) $0^\circ < \theta < 180^\circ$; b) $180^\circ < \theta < 360^\circ$.

the first mode. The amplitude variance for each mode normalized by the amplitude variance of mode 1 of the final iteration is given in Figure II.6a. The velocity solution is assumed to have converged when the root mean square deviation in maximum shear velocity between consecutive iterations is less than 1% of the root-mean-square of the previous iteration, this generally occurs in less than 11 iterations, Figure II.6b.

The model qualitatively reproduces the laboratory observations of Jonsson and Carlsen (1976; Figure II.7). The root mean square deviation between the model and data over both the wave phase and elevation is shown in Figure II.8. The root mean square deviation of the velocity calculated over the elevation at each phase shows the largest deviation occurs preceding the peak velocity at phases between 120° and 150° and between 300° and 330° . The root mean square deviation calculated over the wave phase at each elevation shows the best correlation at both the upper and lower boundaries and the largest deviation in the velocity overshoot region. The model's under representation of the overshoot region may possibly be attributed to the linear vertical structure of the eddy viscosity model. BS92 have increased model agreement in this region by assuming an exponentially capped eddy viscosity model. Future investigations could include tuning the vertical structure of the eddy viscosity model for better agreement to the Jonsson and Carlsen data. The model's prediction of the bed shear velocity, u_{*o} , is in good agreement (correlation coefficient is .95) with measurements, Figure II.9.

The model was used to investigate the wave bottom boundary layer response to a variety of wave conditions similar to those observed in nature. To accomplish this, the wave bottom boundary layer response to a variety of input free stream wave conditions is quantified by evaluating the temporal distribution of bed shear velocities and by evaluating the spatial and frequency structure of the variance. In the first investigation, the effect of free stream velocity and acceleration variations on the wave bottom boundary layer (herein, WBBL) are examined with three separate monochromatic waves. In the second investigation, the response of the WBBL to free stream velocities which have non-sinusoidal shapes is characterized with 36 cases of free stream velocities which have uniform variance and a variety of skewness and asymmetry values.

In the first investigation, three input monochromatic free stream wave cases ($u_\infty(t) = u_o \cos(\omega t)$) were considered with free stream root mean square velocities and accelerations ranging from 35.4 cm/s to 70.7 cm/s and from 88.6 cm/s² to 44.3 cm/s², respectively (Table II-1). The response of the WBBL to each of the cases is evaluated with the calculated bed shear velocity, u_{*o} , Figure II.10. The largest bed shear velocity occurs in case 1 when both the root mean square velocity and acceleration are largest. In (II-1) the

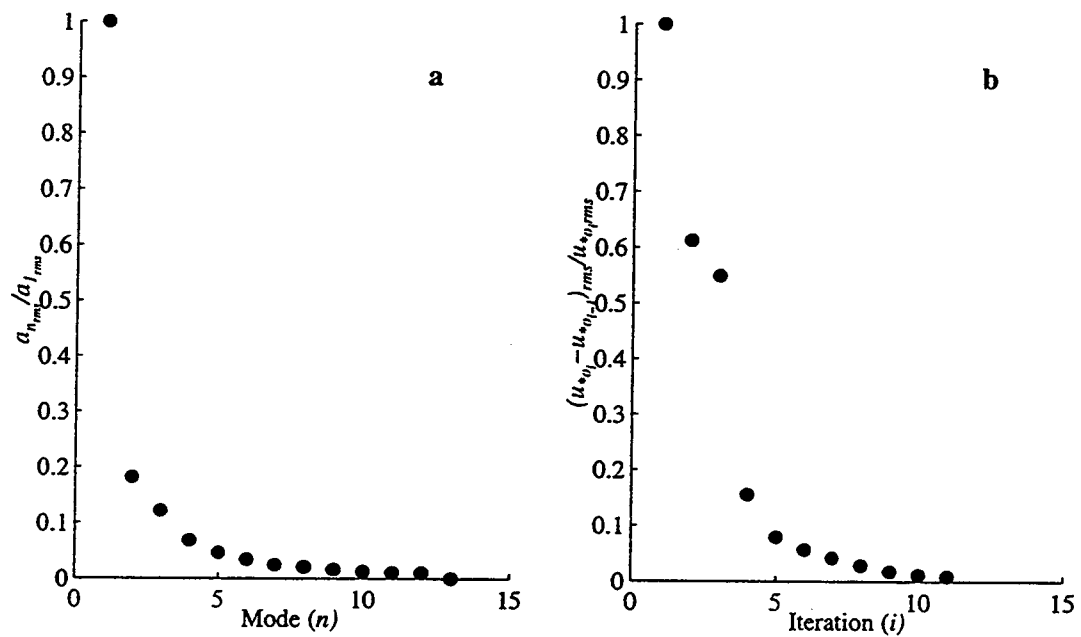


Figure II.6. a) Series convergence is assumed when the rms of a given mode amplitude ($a_{n,rms}$), $a_{n,rms}/a_{1,rms} < 1\%$.
 b) Solution convergence is assumed when the rms deviation of the bed shear velocity between two consecutive iterations $((u_{*o_i} - u_{*o_{i-1}})_{rms})$ is less than 1% of the rms of the first iteration ($u_{*o,rms}$), $(u_{*o_i} - u_{*o_{i-1}})_{rms}/u_{*o,rms} < 1\%$.

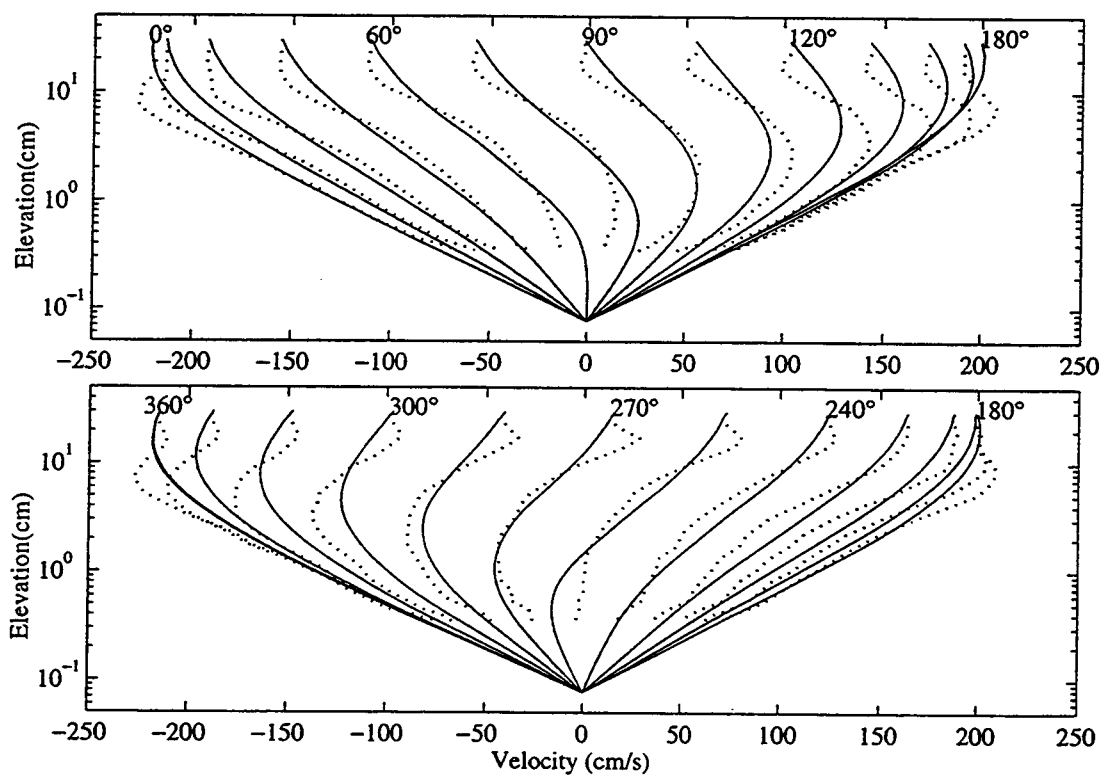


Figure II.7. Comparison between (—) model and (...) measured [Jonsson and Carlsen, 1976] cross-shore velocities over the wave phase.

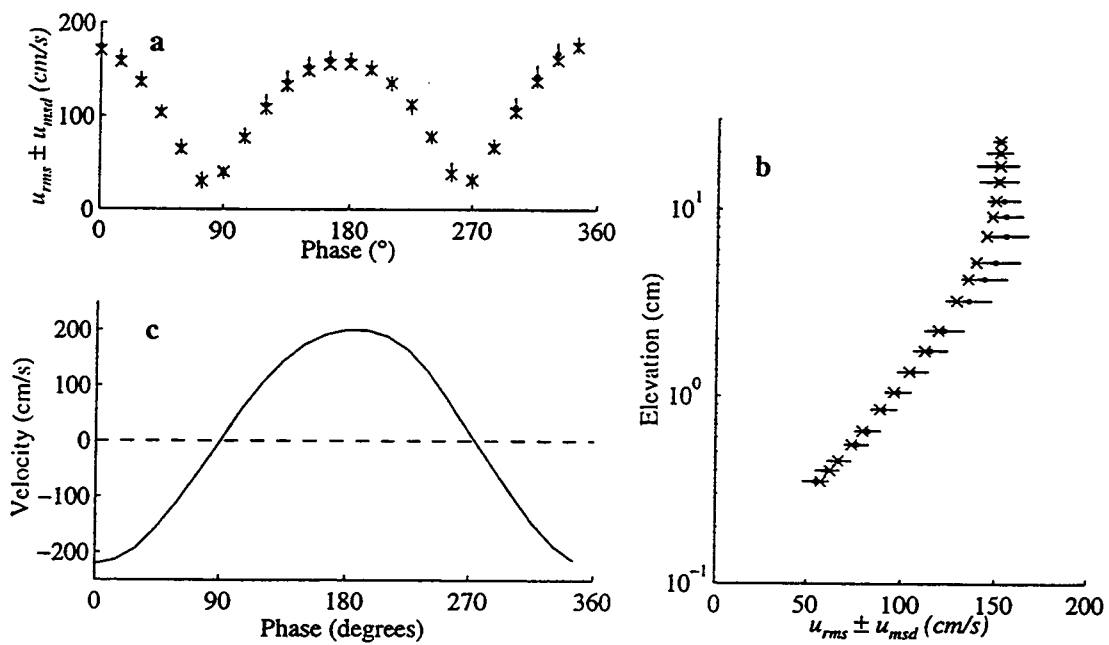


Figure II.8. Comparison of the rms velocity calculated a) over the elevation at each wave phase, $u_{rms}(\theta) \pm u_{rmsd}(\theta)$; and b) over the wave phase at each elevation, $u_{rms}(z) \pm u_{rmsd}(z)$; (*) model results and (•) measurements [Jonsson and Carlsen, 1976]. Error bars indicate one root mean square deviation (rmsd) between model results and measurements. c) Input free stream velocity, u_{∞} ;

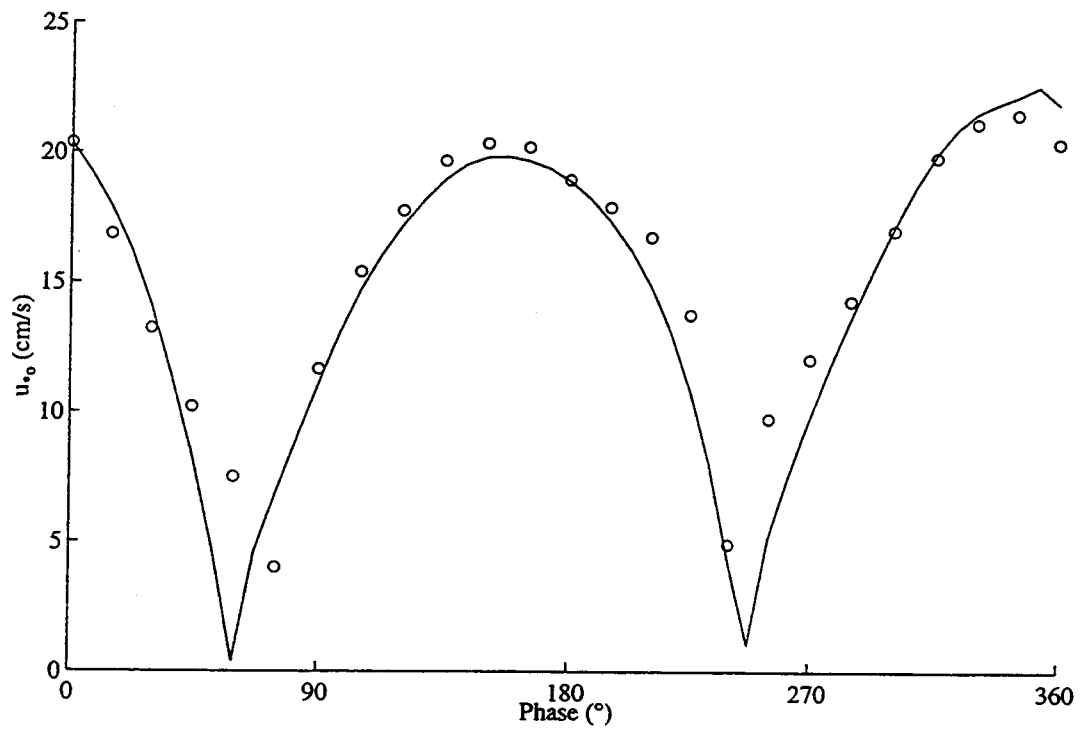


Figure II.9. The bed shear velocity, u_{*o} , over the wave phase: (o) measurements; and (—) model. The correlation coefficient between model results and measurements is 0.95.

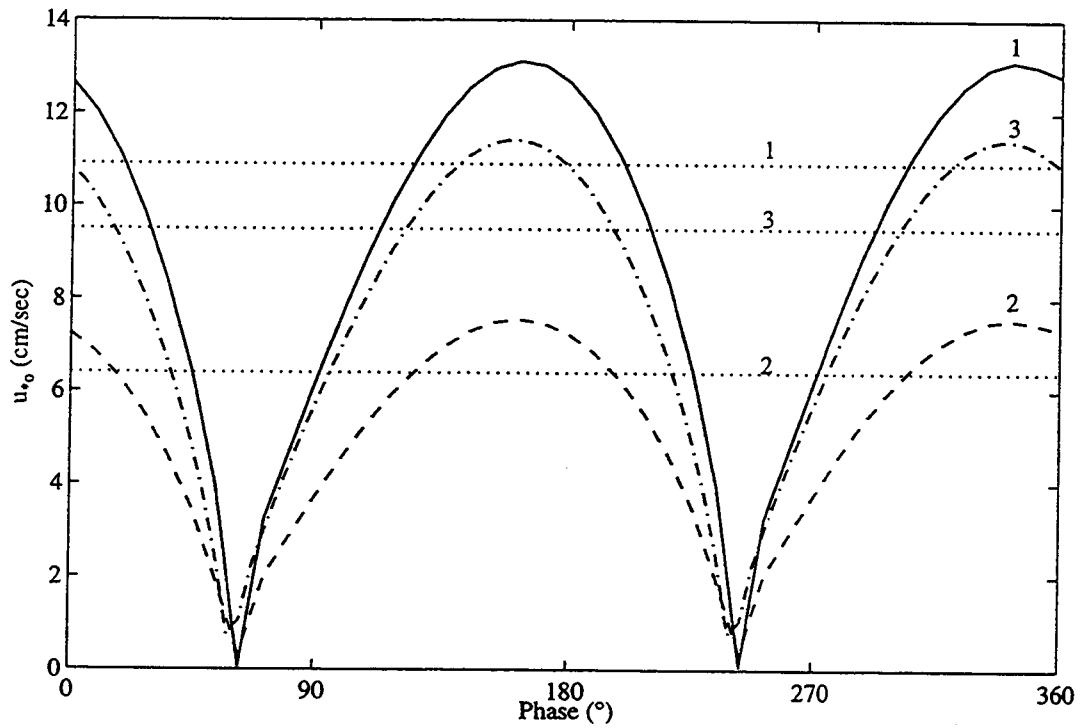


Figure II.10. Bed shear velocity, u_{*o} , for each of the three cases: (—) Case 1, $u_o=100$ cm/s, $T=5$ s; (---) Case 2, $u_o=50$ cm/s, $T=5$ s; (- · -) Case 1, $u_o=100$ cm/s, $T=10$ s; Dotted lines represent bed shear velocity calculated at peak velocity, u_o , by (36a) and (36b), u_{*opeak} for each case.

free stream acceleration forces the WBBL dynamics, consequently a correlation between the bed shear and free stream acceleration is anticipated. The shear velocity also appears correlated to the free stream velocity. This is indicated by cases 2 & 3 where the free stream acceleration is held constant and the bed shear increases with increasing free stream velocity.

case	T s	u_o cm/s	$(u_{\infty})_{rms}$ cm/s	$\left(\frac{\partial u_{\infty}}{\partial t}\right)_{rms}$ cm/s ²	δ_{smith} cm	$(u_{*o})_{peak}$ cm/s	$(u_{*o})_{rms}$ cm/s	$\langle u_{*o} \rangle$ cm/s	$(u_{*o})_{max}$ cm/s
1	5	100	70.7	88.6	4.3	10.9	9.7	9.0	13.1
2	5	50	35.4	44.3	2.5	6.4	5.6	5.2	7.57
3	10	100	70.7	44.3	7.5	9.5	8.4	7.8	11.4

Table II-1. Input wave period, T, and amplitude, u_o , conditions and rms free stream velocity, $(u_{\infty})_{rms}$, and rms acceleration, $\left(\frac{\partial u_{\infty}}{\partial t}\right)_{rms}$, for three independent wave cases. Also given is the characteristic boundary layer thickness and shear velocity as predicted by the Smith model and the rms, mean, and maximum bed shear velocity as predicted by the model presented in this paper.

Comparing the model's predicted bed shear velocities with those predicted by (II-36a) and (II-36b) (a commonly accepted method for scaling the bed shear velocity), it is found that $(u_{*o})_{peak}$ exceeds $(u_{*o})_{rms}$ by 12% to 14% (Table II-1). Also, the large temporal variations of u_{*o} as seen in observations (Figure II.5) and predicted by this model are neglected by scaling the shear velocity as uniform over the wave phase, as in (II-36a) and (II-36b).

For each monochromatic wave case, the power spectrum of the velocity at three elevations within the boundary layer is presented in Figure II.11. As expected, the energy at the fundamental frequency decreases with decreasing elevation. As z approaches z_o , the weakly nonlinear interaction of the right hand side of (II-1) between $u_{*o} \left(\propto \left| \frac{\partial u}{\partial z} \right|_{z=z_o} \right)$ and $\frac{\partial u}{\partial z}$ increases and results in transfer of energy from the fundamental to other frequencies.

As a crude approximation for illustrative purposes, assume that $\frac{\partial u}{\partial z} \Big|_{z=z_o}$ varies as a sinusoidal wave, $\sin(\omega t)$. At the bed, the right hand side of (II-1) varies with

$$\begin{aligned} \left. \frac{\partial \tau}{\partial z} \right|_{z=z_0} &\propto |\sin(\omega t)| \sin(\omega t) \\ &\approx \frac{1}{\pi} \left(\frac{8}{3} \sin(\omega t) - \frac{8}{15} \sin(3\omega t) - \frac{8}{105} \sin(5\omega t) \right) \end{aligned}$$

Hence, for a monochromatic input wave, we expect energy to be present at the odd harmonics. For a bichromatic input wave, energy would be transferred to both sum and difference frequencies of the two input primary frequencies. In Figure II.11, the 5 sec wave (cases 1 & 2), energy is present at .6 and 1 Hz and similarly, for the 10 sec wave (case 3), energy is present at .3 and .5 Hz. This result is in agreement with TM84, who observed that to match the variance at odd harmonics seen in the Jonsson and Carlsen data set, a time varying u_* must be considered.

The relative amplitude at each elevation between the third and fifth harmonics of velocity and the first harmonic of velocity show that these harmonics at the bed represent approximately 8 and 4 % of the fundamental and decay as the elevation increases, Figure II.12. Because of the phase shift in the WBBL, this weakly nonlinear interaction decreases with increasing elevation, as the phase shift between $\left. \frac{\partial u}{\partial z} \right|_{z=z_0}$ and $\frac{\partial u}{\partial z}$ increases.

The phase and amplitude of the cross-shore velocity vertical structure at the first (fundamental), third, and fifth harmonic frequencies is examined by calculating the cross spectral matrix between each elevation using the first mode of a frequency domain empirical orthogonal function (CEOF) (Wallace and Dickenson, 1972), Figure II.13. In each case, the first mode describes at least 99% of the variance. As expected, the phase shift at the first harmonic increases with decreasing elevation and is approximately 30° at the bed. In contrast to the fundamental frequency, at both the third and fifth harmonic, the amplitude approaches zero at the upper domain, satisfying the upper boundary condition of a single frequency input velocity. Additionally, the phase associated with these harmonics is larger than that of the fundamental frequency.

In nature waves are never truly monochromatic and often have peaky (skewed) and sawtooth (asymmetric) shapes. Observations of shoaling surface gravity waves, indicate that both wave velocity skewness and asymmetry increase to their maximum values at the onset of breaking (Elgar et al, 1990). At the break point, the normalized wave skewness is as large as .6 and normalized wave asymmetry is as large as 1.2. The normalized third order moments are defined with the following equations (Elgar and Guza, 1985)

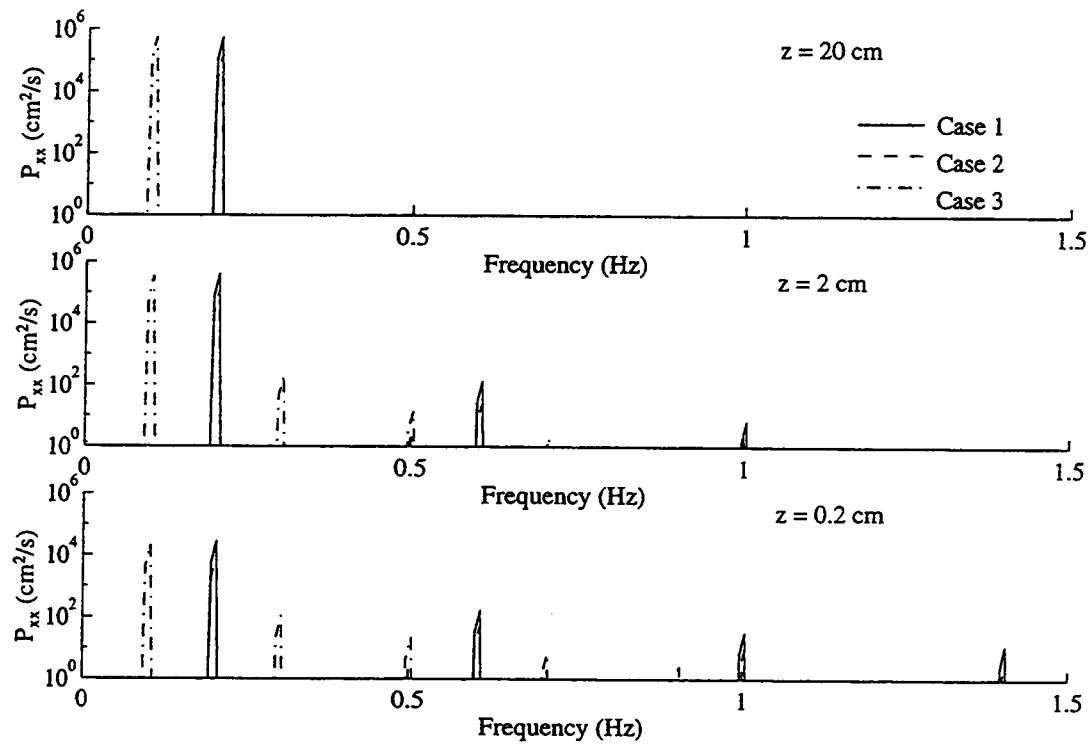


Figure II.11. Energy density spectra for each of the three cases at three elevations: Case 1, $u_0=100$ cm/s, $T=5$ s; Case 2, $u_0=50$ cm/s, $T=5$ s; Case 3, $u_0=100$ cm/s, $T=10$ s.

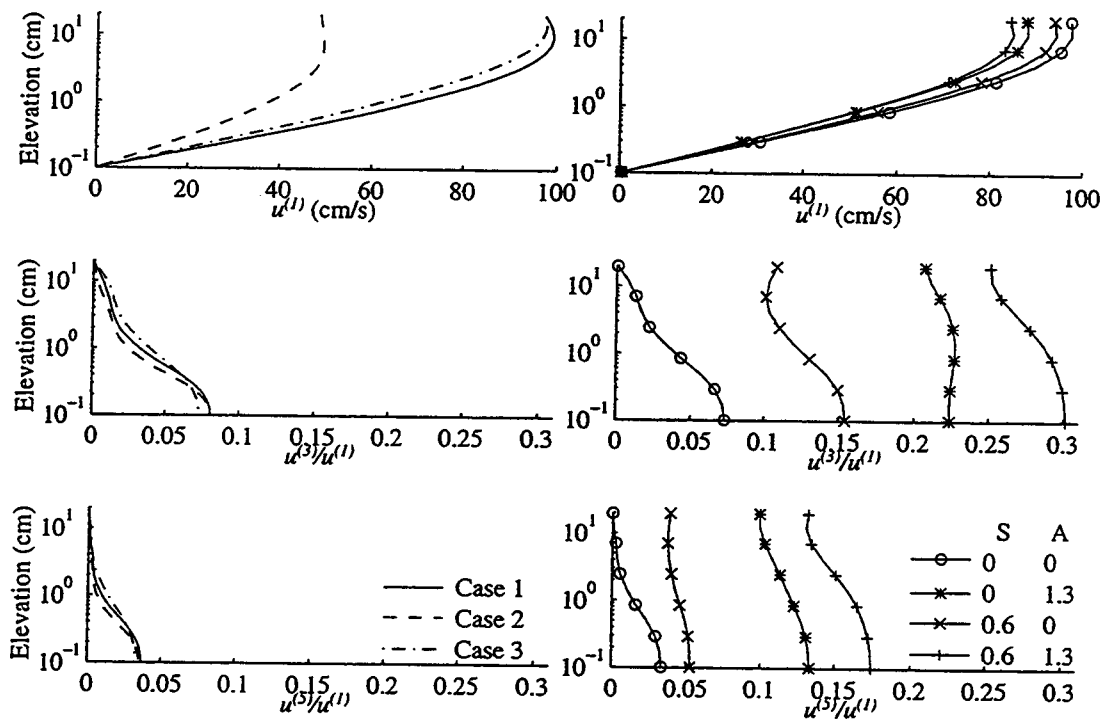


Figure II.12. The predicted amplitude of the first harmonic of velocity (top panel). The predicted relative amplitude of the third (middle panel) and fifth (bottom panel) harmonics to the first harmonic. The results for three monochromatic input waves are shown in the left panels and the results for the four skewed and asymmetric input waves are shown in the right panels. The superscripts ⁽¹⁾, ⁽³⁾, and ⁽⁵⁾ denote the first, third and fifth harmonic of velocity, respectively.

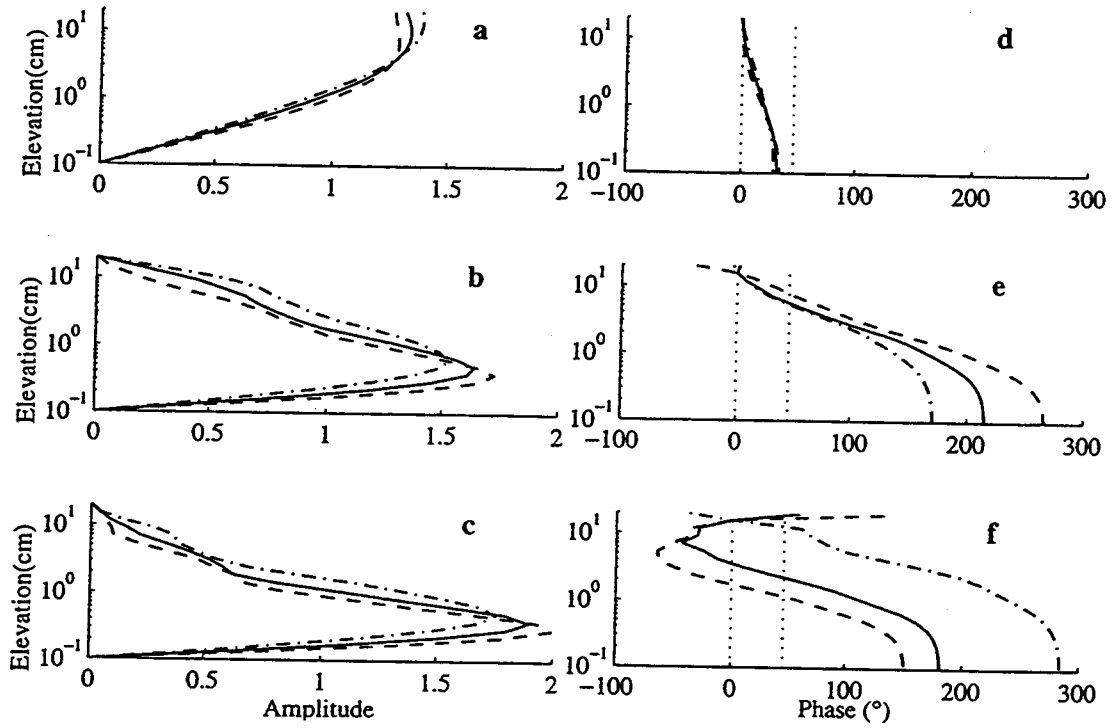


Figure II.13. The normalized frequency domain EOFs of the cross-shore velocity at the first (top panels), third (middle panels), and fifth (bottom panels) harmonic of velocity: a-c) amplitude; d-f) phase. Each line represents: (—) Case 1; (---) Case 2; (- · -) Case 3. In all cases, mode 1 describes at least 99% of the variance.

$$S = \frac{\langle u^3(t) \rangle}{\langle u^2(t) \rangle^{3/2}}$$

$$A = -\frac{\langle (H(u))^3(t) \rangle}{\langle (H(u))^2(t) \rangle^{3/2}}$$

where $H(u)$ is the Hilbert transform of u .

The effect of free stream wave skewness and asymmetry on the response of the wave bottom boundary layer is investigated for 36 uniform variance input wave conditions with normalized skewness and asymmetry values varying from 0 to .625 and 0 to 1.25, respectively. The temporal distribution and amplitude of the predicted bed shear velocity of four of the extreme cases is shown to greatly vary with input skewness and asymmetry, Figure II.14. As in the monochromatic wave cases the ratio of the third and fifth harmonics of the velocity to the first harmonic increases with decreasing elevation, Figure II.12. However, the third harmonic of velocity at the bed can be as large as 30% of the first harmonic of velocity when the combined effect of the maximum free stream velocity skewness and asymmetry, and the WBBL nonlinearities are considered. Over the range of skewness and asymmetry values investigated, the harmonic amplitude ratio is shown to increase with increasing rms free stream wave acceleration which increases with increasing skewness and asymmetry, Figure II.15. Also shown to increase with increase skewness and asymmetry is the rms bed shear velocity, $(u_{*o})_{\text{rms}}$, Figure II.15, whereas the maximum bed shear velocity primarily increases with increasing wave skewness, Figure II.14.

Energetics-based basic sediment transport models assume that the total sediment transport rate is proportional to the a dimensionless vector and the energy dissipation rate, or work done by the fluid on the bed, $\tau_o u$ (Bowen, 1980 and Baillard, 1981). The transport due to suspended load, i_s , is proportional to

$$i_s \propto u_{\infty} |\tau_o u_{\infty}| \quad (\text{II-37})$$

Commonly, the bed stress is assumed to be a quadratic function of the velocity, $\tau = \rho c \mu^2$. Using a quadratic stress law, the time averaged work done is large under skewed waves and zero under purely asymmetric waves. The model presented in this paper predicts the time varying velocity and bed shear stress, allowing for the instantaneous computation of the energy dissipation rate without assuming a quadratic shear stress. As Figure II.14 shows, in accordance with the Baillard and Bowen models, the suspended sediment transport due to the velocity and energy dissipation rate as defined in (II-37) increases with increasing free stream wave skewness, and reaches its maximum value of $3.8 \times 10^5 \text{ cm}^4/\text{s}^4$ under purely skewed waves, Figure II.15. Yet under purely asymmetric waves, the predicted time

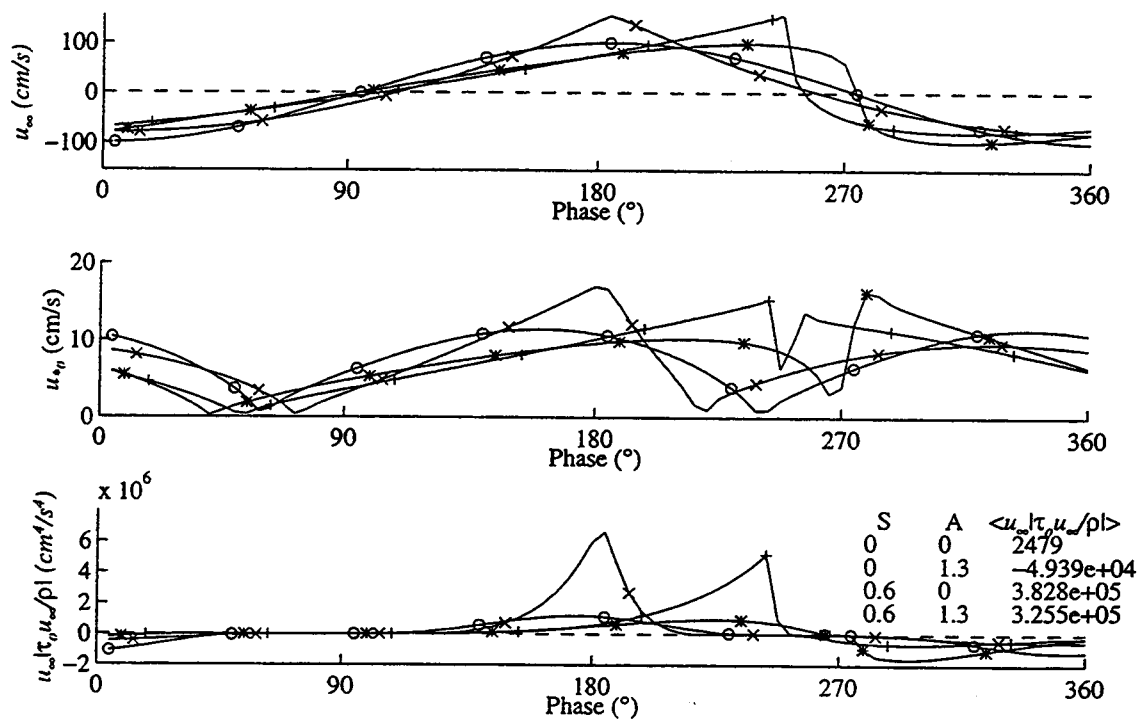


Figure II.14. Four separate input wave velocities (top panel) and the model predicted bed shear velocity (middle panels). The velocity times the work done on the bed due to stress on the bed, $u_{\infty} |\tau_0 u_{\infty}| / \rho$ is given in the bottom panel. All input waves have equal variance and different skewness and asymmetry values.

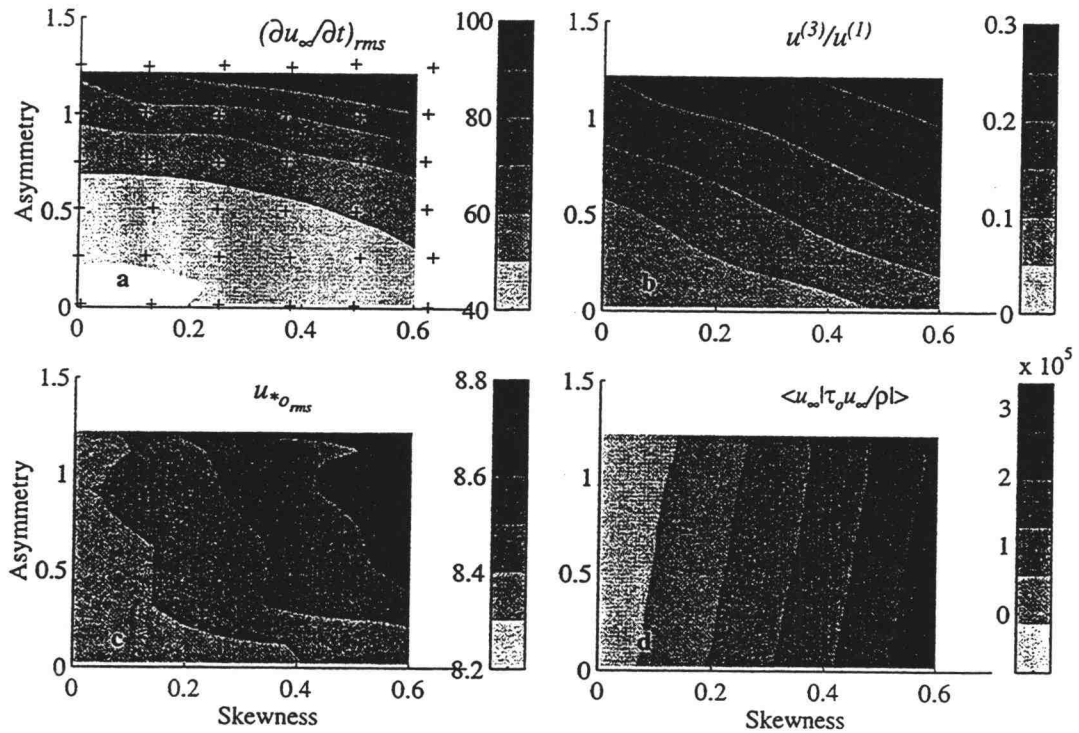


Figure II.15. Distribution of a) rms free stream acceleration, $(\partial u_\infty / \partial t)_{rms}$; b) predicted relative bed velocity of the third harmonic, $u^{(3)}/u^{(1)}$; c) rms bed shear velocity, $u_{*o,rms}$; d) relative net suspended sediment transport $\langle u_\infty |\tau_o u_\infty| / \rho l \rangle$; over free stream velocity skewness and asymmetry values ranging from 0 to 0.6 and 0 to 1.2, respectively. The 36 individual runs are indicated with + symbols.

averaged work done is considerably smaller, $-0.5 \times 10^5 \text{ cm}^4/\text{s}^4$ and directed in the offshore direction. The model predicts a convergence of net suspended load transport at the break point where the skewness is a maximum. This result is consistent with sediment models which predict the formation of sand bars at the breakpoint.

II-6. Conclusions

An analytic solution for the vertical and temporal structure of the wave bottom boundary layer, cross-shore velocity under arbitrary free stream wave forcing is derived. The eddy viscosity is represented as a separable functions of time and depth. The time-dependent boundary condition ($u(\delta, t) = u_\infty(t)$) is distributed through the solution domain with a transformation of $u(z, t)$ to create a well posed solvable initial boundary value problem with time independent boundary conditions. The transformed equation is solved with the separation of variables technique. An analytic expression for the time and depth dependent cross-shore velocity is determined. No assumption has been made about the form of the input wave velocity, so the model is able to predict the temporal and vertical cross-shore velocity structure and the temporally varying bed shear for a random wave field.

Good agreement is found between the model predicted velocity structure and bed shear velocity and laboratory measurements. The correlation between the model predicted and measured bed shear velocity is .95. Predictions of the bed shear velocity under three independent monochromatic input wave velocities indicate that bed shear velocity increases with increasing wave velocity and acceleration.

A weakly nonlinear interaction results from scaling the shear velocity with the time-dependent velocity shear at the bed. The magnitude of the nonlinear interaction becomes larger as z approaches z_0 , and at the bed, the shear stress, τ is proportional to

$$\tau \propto \left(\left| \frac{\partial u}{\partial z} \right| \frac{\partial u}{\partial z} \right)_{z=z_0}.$$

For a monochromatic free stream velocity, this interaction distributes input energy to odd harmonics. For the cases considered in this paper, the amplitude of the velocity energy density at the bed in the third harmonic is only 8% of the amplitude at the first harmonic. However, the combined effect of skewed and asymmetric input waves characteristic of those found in the coastal region and the nonlinear interactions results in amplitude ratios of as much as 30%. For monochromatic input wave velocities the effect of nonlinearities may be neglected, but for non-sinusoidal input wave velocities, as often found in nature, the energy in the higher harmonics may well have a significant effect.

The model also predicts the time-dependent structure of the bed shear velocity, which is shown to vary significantly over a wave period. The bed shear velocity is examined over a variety of skewed and asymmetric input wave forcing conditions. The rms bed shear velocity increases by as much as 11% with increasing input wave skewness and asymmetry (which also indicates increased wave acceleration). However, the maximum bed shear velocity is shown to increase with increasing wave skewness and decreasing wave asymmetry, i.e. maximum bed shear occurs under the peakiest input waves.

In agreement with energetics based sediment transport models, the suspended sediment transport rate is shown to be strongly correlated to wave skewness and reach a maximum value under maximum free stream velocity skewness. Under purely asymmetric waves, the quantity is significantly smaller but is directed in the offshore direction. In contrast, simple quadratic stress models neglect phase and amplitude variations between velocity and shear stress and predict zero work done under asymmetric waves.

The model results are encouraging and future research will include an investigation of variations in the vertical structure of the eddy viscosity model and the comparison of the model to field measurements collected during the Duck94 field experiment.

CHAPTER III: FIELD OBSERVATIONS OF THE WAVE BOTTOM BOUNDARY LAYER

Abstract

This paper presents a comprehensive set of velocity and suspended sediment observations in the surf zone wave bottom boundary layer, collected during the Duck94 field experiment on the Outer Banks of the North Carolina coast. Cross-shore velocity measurements in the wave bottom boundary layer were made using five hot film anemometers, nominally spaced from 1 to 5 cm above the bed, while the free stream velocity was measured with an electromagnetic current meter at 14 cm elevation. The time varying location of the sea bed was estimated to be roughly 1 cm with a stacked set of bed-penetrating fiber optic back scatter sensors.

The location of the bottom varied several centimeters over a 34 minute data run. Even over 4 minute segments of quasi steady statistics, occasional large waves caused short erosion and redeposition events, complicating the definition of bottom location and causing the rms velocity statistics to be non-zero below the mean bed location. This leads to obvious difficulties in comparisons with two, 1-D time-dependent, eddy viscosity wave bottom boundary layer models. For example, bottom shears based on rms amplitude decay were lower than predicted, as were phase angle leads within the boundary layer, perhaps indicative of more rapid mixing of momentum than predicted by the models. The phase and amplitude frequency response estimated using frequency domain empirical orthogonal functions show a non-linear response of the wave bottom boundary layer over the incident band. These observations are among the first coherent looks at the wave bottom boundary layer in the surf zone under conditions of significant sediment response. They highlight the added complexity of the dynamics in natural environments.

III-1. Introduction

Although the wave bottom boundary layer occupies only a small part of the overall water column ($O(10\text{ cm})$), it has an importance that has been recognized for many years. Because the wave bottom boundary layer is the region of fluid immediately next to the sea bed, its role in sediment suspension and bed form development and migration is crucial.

Theoretical investigations of the oscillatory boundary layer began with the idealized laminar flow solution due to a monochromatic wave on a flat non-erodable bottom [Batchelor, 1967]. This solution predicts an amplitude decay and a phase shift within the layer. Later investigations [Smith, 1977; Grant and Madsen, 1979] furthered this work by considering turbulent flow with vertically varying mixing and rough beds. In recent years,

investigations have further incorporated rippled beds [see review by *Sleath*, 1990], more detailed turbulence modelling [*Justesen*, 1988], and random waves [*Beach and Sternberg*, 1992; *Foster et al.*, submitted]. These improvements have been motivated by obvious inadequacies of the early assumptions to the actual coastal ocean environment.

The controlled environment of the laboratory makes basin studies attractive for oscillatory bottom boundary layer observations and most tests of the above theories have been based exclusively on laboratory measurements. One of the first and perhaps most referenced wave bottom boundary layer studies is that of *Jonsson and Carlsen* [1976]. They examined the temporal and vertical structure of a monochromatic oscillatory bottom boundary layer. Additional laboratory investigations further examined the turbulence variations over a smooth bed under monochromatic surface waves [*Hino et al.*, 1983; *Jensen et al.*, 1989]. While these laboratory studies contribute to our understanding of the wave bottom boundary layer (WBBL) under monochromatic waves, the extrapolation of these studies to a natural environment has not yet been achieved. In a comprehensive review of experimental and theoretical wave bottom boundary studies, *Sleath* [1990], concluded that conclusions based solely on laboratory measurements will probably require substantial modification as field data becomes available.

Because of the energetic and transitory nature of the surf zone, wave bottom boundary layer observations on natural beaches are much less easily obtained than their laboratory counterparts. However, in recent years the success in making these field WBBL measurements has increased. Using a hot film anemometer in the near bed region and visual observations, *Conley and Inman* [1992] identified a set of stages in the development of the fluid-granular boundary layer. They concluded that observed asymmetries in the fluid-granular boundary layer development were not directly related to asymmetries in the free stream wave velocity. WBBL observations on a dissipative Oregon beach showed that observed sediment suspension and turbulence variance events primarily occurred during the transition between offshore and onshore flow [*Foster et al.*, 1994]. Both of these investigations highlight the complex and presently unpredictable response of the wave bottom boundary layer to skewed and asymmetric surface waves in the natural environment.

The first field observations of the WBBL vertical structure are given in *Trowbridge and Aagrwal* [1995]. Using a vertical profiling Laser Doppler Velocimeter, they examined two realizations of the wave bottom boundary layer due to 9 sec waves with a free stream root mean square wave velocity of 10 cm/s in a 6 m water depth. Examining cross-shore flows, they observed an increase in phase lead and a slight decrease of variance with

increasing proximity to the bed and concluded that the observed scales were characteristic of simple theoretical wave bottom boundary models.

The observations presented here are the first surf zone measurements to examine the temporal and vertical variations of wave bottom boundary layer dynamics with simultaneous measurements of the bed elevation and vertical distribution of suspended sediment under wave conditions for which bed response is important. The unique nature of these observations allows us to evaluate predictions from both a monochromatic and a random wave bottom boundary layer models.

In this paper we evaluate two existing simple WBBL models with field observations made during the Duck94 field experiment. In section 2, two theoretical models for the wave bottom boundary layers are reviewed. In section 3, the instrumentation and the field measurement techniques are summarized. Evaluation of the two models using field observations are presented in section 4. An interpretation of field results and model comparisons are presented in the discussion, section 5, and conclusions are presented in section 6.

III-2. Models

III-2.1 WBBL theory

The one-dimensional time-dependent wave bottom boundary layer governing equation is

$$\frac{\partial u}{\partial t} - \frac{du_{\infty}}{dt} = \frac{1}{\rho} \frac{\partial \tau}{\partial z}, \quad (\text{III-1})$$

with boundary conditions,

$$u(\delta, t) = u_{\infty}, \text{ and}$$

$$u(z_0, t) = 0,$$

where $u = u(z, t)$ is the cross-shore velocity, $u_{\infty} = u_{\infty}(t)$ is the free stream velocity, z_0 is the bed roughness, and δ is the boundary layer thickness. Throughout this paper, the vertical elevation (z) is positive upwards from the bed, and the cross-shore position (x) is positive offshore. In both models evaluated here, the shear stress (τ) is estimated with an eddy viscosity model

$$\frac{\tau}{\rho} = -\langle u' w' \rangle \approx \nu_t \frac{\partial u}{\partial z}, \quad (\text{III-2})$$

where ρ is the fluid density, ν_t is the eddy viscosity, u' is the cross-shore turbulent velocity, and w' is the vertical turbulent velocity. Assuming that all turbulence is initiated at the bed

and proportional to elevation, the eddy viscosity is approximated with [Smith, 1977; Grant and Madsen, 1979]

$$v_t \equiv \kappa u_* z, \quad (\text{III-3})$$

where u_* is the bed shear velocity and $\kappa (=0.41)$ is Von Karman's constant.

III-2.2 WBBL Velocity under a Single Monochromatic Wave

The first model evaluated in this paper, based on that of Smith [1977], represents the true free stream velocity with a single representative monochromatic wave with free stream amplitude (u_f) and frequency (ω_f). The boundary layer thickness and shear velocity are parameterized with constant values defined with the equations.

$$\delta_b = \frac{u_{*1}}{2\omega_f}, \text{ and} \quad (\text{III-4})$$

$$u_{*1} = \frac{\kappa u_f}{\ln\left(\frac{\delta_b}{z_0}\right)}, \quad (\text{III-5})$$

where δ_b is the representative boundary layer thickness of the monochromatic wave, as defined in Beach and Sternberg [1992], and u_{*1} is the representative shear velocity. The cross-shore wave bottom boundary layer velocity (u_s) at the specified characteristic frequency which satisfies (III-1) is

$$u_s(z, t) = u_f \Re\left\{e^{i\omega_f t} (1 - Z(z))\right\}, \quad (\text{III-6})$$

where $Z(z)$ is the complex spatial amplitude. The spatial amplitude is determined by substituting (III-6) into (III-1) and then solving the resulting equation numerically

$$i\omega_f Z = \kappa u_{*1} \frac{\partial Z}{\partial z} + \kappa u_{*1} z \frac{\partial^2 Z}{\partial z^2}. \quad (\text{III-7})$$

Although this model can not predict the velocity structure at each instant in time under a random wave field, it is possible to predict the vertical amplitude and phase structure, as well as the boundary layer thickness, and shear velocity at the characteristic frequency. Here, we choose the characteristic frequency (ω_f) to be the peak frequency, and the amplitude (u_f) to be the root mean square (RMS) velocity over an entire record.

III-2.3 WBBL Velocity under a Random Wave Field

The second model, from Chapter II (herein FGH), is based on the same dynamics as the Smith model, but allows for an arbitrary random wave forcing. The FGH model is an analytical eigenfunction series solution which assumes the eddy viscosity is a

separable function of time and space; whereas, the Smith model assumed a time independent eddy viscosity model. As in FGH, we assume

$$v_t = \kappa u_{*o}(t)z \quad (\text{III-8})$$

where $u_{*o}(t)$ is the bed shear velocity. The complete series solution is

$$u_{FGH}(z, t) = \sum_{n=1}^{\infty} a_n(t) \Psi_n(z) + \frac{z - z_o}{d - z_o} u_{\infty}, \quad (\text{III-9})$$

where a_n is the amplitude of the n^{th} spatial eigenfunction ($\Psi_n(z)$), and d is the top of the domain and greater than the boundary layer thickness. The eigenfunction, $\Psi_n(z)$ is defined as

$$\Psi_n(z) = Y_o(2\lambda_n z_o^{1/2}) J_o(2\lambda_n z^{1/2}) - J_o(2\lambda_n z_o^{1/2}) Y_o(2\lambda_n z^{1/2}), \quad (\text{III-10})$$

where λ_n are the eigenvalues, J_o and Y_o are zero order Bessel functions of the first and second kind, respectively. The eigen values are determined by solving

$$Y_o(2\lambda_n z_o^{1/2}) J_o(2\lambda_n d^{1/2}) - J_o(2\lambda_n z_o^{1/2}) Y_o(2\lambda_n d^{1/2}) = 0. \quad (\text{III-11})$$

The amplitude is determined by

$$a_n(t) = a_n(0) e^{-\lambda_n^2 \int_c^t \kappa u_{*o}(\tau) d\tau} + \int_0^t F_n(\sigma) e^{-\lambda_n^2 \int_c^{\sigma} \kappa u_{*o}(\tau) d\tau} d\sigma, \quad (\text{III-12})$$

where the forcing is

$$F_n(t) = \frac{1}{c_n} \int_{z_o}^d \left(\frac{d-z}{d-z_o} \frac{du_{\infty}}{dt} + \kappa u_{*o}(t) \frac{u_{\infty}}{d-z_o} \right) \Psi_n(z) dz. \quad (\text{III-13})$$

c_n is the orthogonality constant and defined with the equation

$$c_n = \int_{z_o}^d \Psi_n(z) \Psi_n(z) dz \quad (\text{III-14})$$

As the bed shear velocity is initially unknown, it is estimated with (III-5) as a constant value over every free stream zero crossing. After the first iteration, the bed shear velocity is directly calculated with

$$u_{*o}(t) = \kappa z_o \left. \frac{\partial u(z, t)}{\partial z} \right|_{z=z_o} \quad (\text{III-15})$$

and iterated until the solution converges. Both models assume a constant bed elevation and known bed roughness. Using both models we will estimate the time and depth dependent cross-shore velocity, the boundary layer thickness, and the bed shear velocity.

III-3. Observations

III-3.1 Deployment

Field observations were made at the Army Corps of Engineers, Field Research Facility (FRF) in Duck, NC from 14 Aug 94 to 23 Aug 94 as part of the cooperative Duck94 experiment. During the experiment the significant wave height varied from 0.5 m to 1.5 m and the significant wave period varied from 4 s to 14 s. A variety of bed conditions were observed.

The following investigation focuses on one 34 minute run recorded on 17 Aug 94. The significant offshore wave height, angle, and period measured at the 8m depth were 0.83 m, 50° from the southeast, and 4.54 sec, respectively. The observations presented in this paper were made in 2 m water depth on the bar crest under both broken and unbroken waves. Visual observations, made using divers and an underwater video camera, indicate a generally well sorted, flat bed with infrequent ripples.

Instruments were deployed from a cantilevered arm attached to the lower boom of the Sensor Insertion System (SIS) on the pier at the FRF, Figure III.1. The angle of both the upper and lower booms were adjusted to keep sensors at least 20 m from the pier. The angle of the cantilever arm relative to the lower boom was set to assure the cantilever arm was parallel to the bed. A spike attached to the lower boom of the SIS was set into the bed with the weight of both booms, fixing the position of the array.

III-3.2 Instrumentation

WBBL velocity observations were made with a vertical array of five hot film (HF1-HF5) anemometers, in the lower 5 cm of the water column with a 1 cm array spacing. A Marsh-McBirney electromagnetic current meter (EMCM) measured the cross-shore and longshore velocity outside the boundary layer at approximately 14 cm above the bed. Sediment suspension and bed elevation were measured with a 19 sensor fiber-optic back scatter (FOBS) probe (described later). Sea surface elevation observations were made using two strain gage pressure sensors. The presence of bed forms was determined using visual observations from an underwater video camera. The relative location of all instruments is shown in Figure III.2.

Hot film anemometers estimate the local fluid speed by assuming the heat transfer between a constant temperature wire (and a protective film coating) and the ambient fluid is a function of the fluid speed. They are designed to adjust the supply of current required to maintain a constant specified temperature of the film coated wire surface. In this experiment, the .0152 mm diameter film was heated to approximately 25 °C above ambient

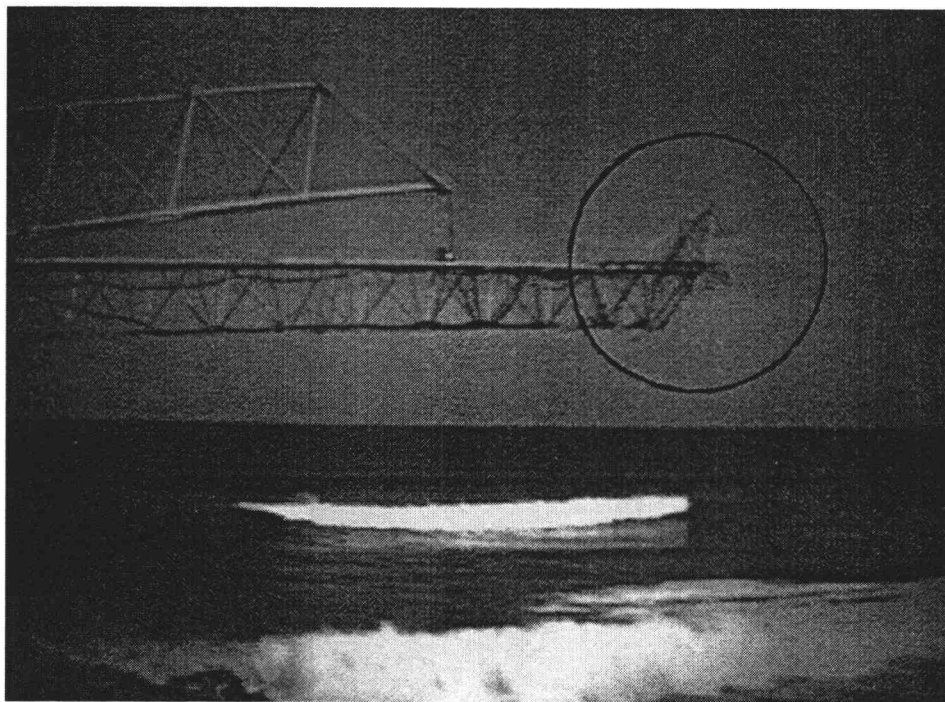


Figure III.1. Photo of instrumentation deployment from the FRF pier using the Sensor Insertion System, 22 Aug 94, (Photo courtesy of Bill Birkemeier). The circled area shows the cantilevered arm with instruments.

water temperature. The voltage output is a measure of the convective cooling of the film due to the surrounding fluid and is related to the magnitude of fluid velocity flowing past the film. The output signal for the probe with the longitudinal axis aligned in the longshore direction is defined with [George *et al.*, 1994]

$$S(t) \propto (u_T^2 + \beta v_T^2 + w_T^2)^{1/2}, \quad (\text{III-16})$$

where β is a parameter which accounts for the relative longitudinal (y) to normal (x and z) heat transfer and is assumed to be small ($\beta \ll 1$). The total cross-shore, longshore, and vertical velocities, u_T , v_T , and w_T , are partitioned into mean($\bar{\quad}$), wave($\tilde{\quad}$), and turbulent($'$) components with

$$u_T = \bar{u} + \tilde{u} + u', \quad (\text{III-17a})$$

$$v_T = \bar{v} + \tilde{v} + v', \text{ and} \quad (\text{III-17b})$$

$$w_T = \bar{w} + \tilde{w} + w'. \quad (\text{III-17c})$$

Here, it is assumed that the cross-shore velocity is the dominant wave velocity ($\tilde{u} \gg \tilde{v} \sim \tilde{w}$), and the mean velocities are small with respect to the wave velocity ($\tilde{u} \gg \bar{u}, \bar{v}, \bar{w}$). Therefore, (III-16) becomes

$$S(t) = \left((\tilde{u} + u')^2 + w'^2 \right)^{1/2}. \quad (\text{III-18})$$

Furthermore, it is assumed that the wave velocity is larger than the turbulent velocity ($\tilde{u} \gg u'$), and that turbulence is isotropic ($u' \sim v' \sim w'$) leading to

$$S(t) = \left(\tilde{u}^2 + 2\tilde{u}u' + O(u'^2) \right)^{1/2} \approx \tilde{u} + u' + O(u'^2). \quad (\text{III-19})$$

To first order it is assumed that the hot film output is a measure of the cross-shore wave and turbulent velocity magnitude. See Appendix C for an analysis of the probe's frequency response.

Sediment suspension and bed level elevation were measured with a fiber optic back scatter sensor (FOBS) probe [Beach *et al.*, 1992]. Light pulses emitted through the each of the FOBS's 19 optical fibers at 850 Hz are filtered to and sampled at 16 Hz. The instrument is composed of two distinct probes, Figure III.2. The smaller tapered lower probe contains eight 600 μm fiber optic sensors, each contained within a 2 mm stainless steel tube and vertically separated from the other sensors by 1 cm. To avoid interference between neighboring sensors, the sensor array elements are staggered around the probe. The larger, upper probe contains 11 sensors with vertical spacing varying from 2 to 6 cm.

The combination of both probes cover a total vertical range of 55 cm. The FOBS probe is calibrated in a fully turbulent, well-mixed tank with the same procedure as outlined in Beach et. al. [1992]. A transfer function between concentration and FOBS output voltage is defined with a quadratic curve.

In addition to measuring sediment suspended in the water column, the FOBS also provides for measurement of the bed elevation. By piercing the bed, bed level fluctuations of 1 cm or more are monitored as sensors are alternatively buried and exposed by bed accretion and erosion, respectively. The lower probe tapers to 2 mm at the lowest sensor, enabling the probe to pierce the bed with minimal interference and scour. When a sensor measures a sustained large concentration, it is assumed to be buried. Often, when the sensor is at the bed-water interface a concentration between the maximum saturated value and the normal background concentration is sustained.

III-3.3 Hot Film Calibration and Data Quality

Prior to each data run, the hot film probes were positioned at the same elevation as the EMCM, the boom of the SIS was lowered into position and a 10 minute calibration data set was collected. During the calibration period, the elevation of the bed was determined with the FOBS. Following the calibration period, the instruments were raised out of the water, the hot films were positioned at the desired elevation based on FOBS estimate of the bed location during the calibration run, the boom was re-lowered back into the water column, and data were recorded for 34 minutes.

Time synchronization between the 5 hot film anemometers, one pressure sensor, and the electromagnetic current meter was achieved by sampling the instruments with the same data acquisition system at 2000 Hz. The pressure sensor and current meter were fed through an optical isolator to prevent 'cross talk', as they were also sampled on another data acquisition system for a companion experiment not discussed here. The effect of the optical isolator on the gain was removed during calibration. Also removed during calibration was the effect of the internal electromagnetic current meter 5 Hz 5 pole Bessel filter. An additional pressure sensor and the FOBS were sampled at 16 Hz with a third independent data acquisition system. Both the hot film and FOBS data acquisition systems were time synchronized with a Global Positioning System (GPS) time code receiver.

The hot film sampling system included a 30.55 Hz analog one pole filter. The effect of the filter was removed by computing the fast Fourier transform (FFT) of 66000 points of data (33 seconds) for each channel and then dividing out the known response of the filter. To prevent the amplification of noise, the filter response was only removed up to

150 Hz, the typical limit of high signal to noise ratio. Consequently, each record was digitally low pass filtered in the frequency domain with a cutoff frequency of 128 Hz and resampled at twice the cutoff frequency, 256 Hz, to 8448 points before converting back to the time domain with an inverse FFT. Each 33 second segment is overlapped with the previous and following data segments by 1 second to eliminate the effect of side lobes caused by the boxcar window. The resulting effective Nyquist frequency is 128 Hz.

The hot film anemometers were calibrated over incident wave frequencies with the EMCM. Each hot film channel was block averaged to 16 Hz to remove some high frequency (turbulent) variability and maintain the variance required to resolve the sharp accelerations caused by the inherent rectification of the hot film signal, and the EMCM was digitally filtered to 2 Hz. The cross correlation between each hot film and the magnitude of the EMCM was computed over consecutive 10 second increments. Each 10 seconds of data for which the squared cross correlation coefficient was greater than 0.7 ($\gamma^2 > .7$) was used in the calibration. For the five hot film sensors in this run, from 23% to 68% of the data were accepted. Data which passed this criteria were fit to a logarithmic curve using a non-linear least squares fit ($|u| = \alpha e^{\beta(\text{volts})}$). Table III-1 gives the coefficients, α and β , for each log fit. Although the expected response for a hot film anemometer is quadratic, a logarithmic curve does not have the potential to yield a minimum within the domain (a possibility which may occur with a quadratic fit) and resulted in statistically acceptable fits. The F statistic, significance level, and root mean square deviation (rmsd) between each hot film sensor and the calibration curve are given in Table III-1. The root mean square deviation and F statistic reported in Table III-1 include the high frequency fluctuations of each HF beyond the incident band, out to 16 Hz. The uppermost hot film sensor, HF5, had an unstable gain, possibly due to oxidation of organics, resulting in a low significance level of 61.25% and consequently was excluded from further investigation. Due to the close proximity to the sea bed (and distance from surface breaking) dropouts due to bubbles were absent.

Hot Film Sensor	α (cm/s)	β (1/volts)	rmsd (cm/s)	Fstat	Sig. Level %
1	0.24	0.76	8.92	5.4	99.5
2	0.51	0.62	8.58	5.3	99.5
3	0.12	0.84	8.77	5.6	99.5
4	0.55	0.62	10.87	3.6	97.25
5	1.48	0.48	15.54	10.0	61.25

Table III-1. Hot film calibration coefficients, α and β , for each hot film sensor. The F statistic between the logarithmic transfer function and each hot film sensor yields significance levels of at least 97% in sensors 1-4.

The sign of the calibrated hot film signal is determined by searching for local minima around each zero crossing of the cross-shore EMCM velocity. Throughout this paper, the onshore directed flow is negative and offshore directed flow is positive. The cross spectrum between each calibrated, derectified hot film velocity and the cross-shore EMCM velocity shows that the two measurements are coherent out to approximately 0.8 Hz, Figure III.3. The integrated variance of the incoherent signal between each HF and the EMCM over the incident wave frequency to 1 Hz, is represented with

$$\varepsilon^2 = \int_{f=0}^{f=1} (1 - \gamma^2)(P_{HF}P_{EMCM})^{1/2} df \quad (\text{III-20})$$

where, ε is the integrated deviation between each HF and the EMCM over the frequency (f) band of interest, γ is the coherence, and P is the energy density spectrum. Good agreement exists between the calibrated, derectified cross-shore velocities as predicted by the four hot film sensors and EMCM with deviations, ε , ranging from 6-8 cm/s, Figure III.4.

Because the hot films were in the region of active sediment suspension, the effect of sediment on the probe response was determined theoretically. The results of this work are presented in Appendix B. Under a maximum sediment concentration of 160 g/l, the theoretical probe response increased by 5% and this effect was consequently neglected.

The bed elevation was determined by comparing the median concentration over consecutive 30 second records to the saturated concentration for each sensor. Saturated values were extracted from the time series by searching for sustained maximum values of

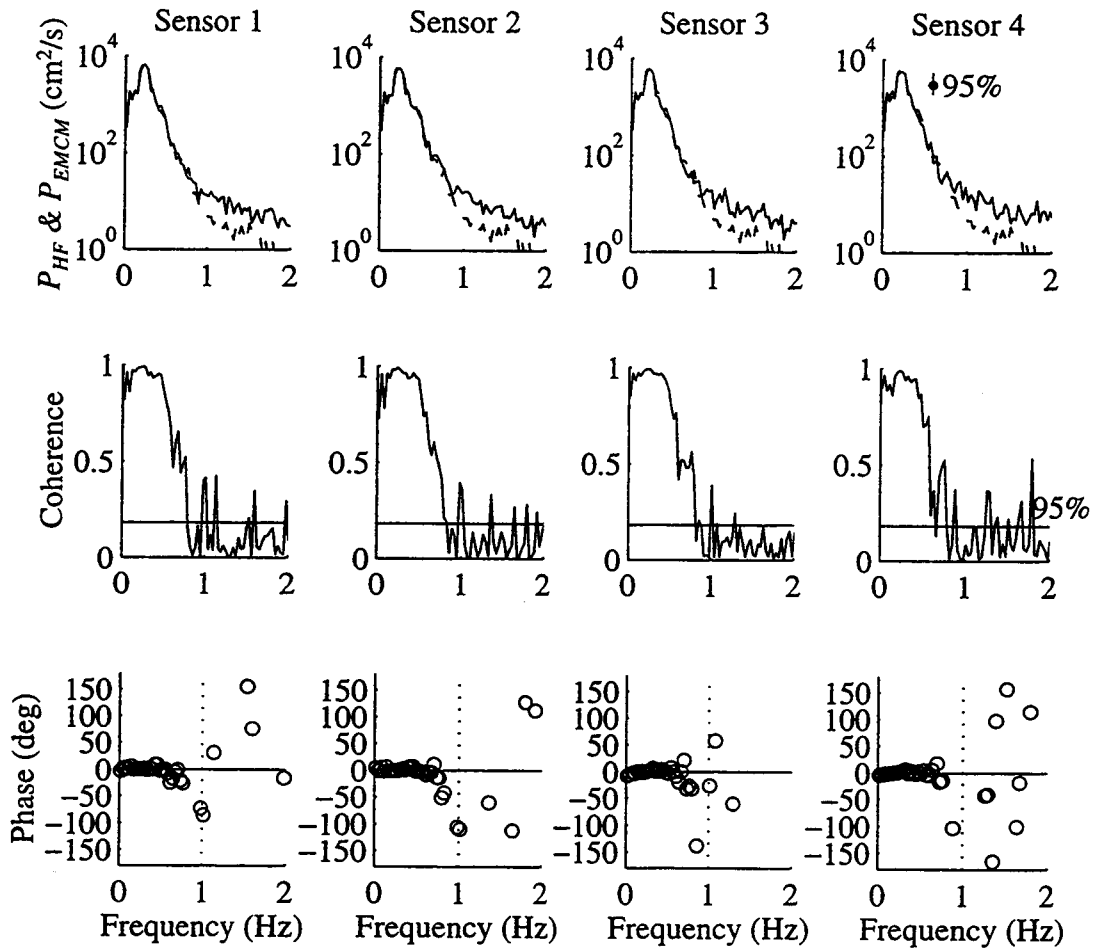


Figure III.3. Coherence and phase between the calibrated derectified cross-shore velocity as measured by hot film sensors 1-4 (—) and cross-shore velocities as measured by the electromagnetic current meter (- -). The coherence remains significant to 0.8 Hz. Each spectra has been calculated with 32 degrees of freedom.

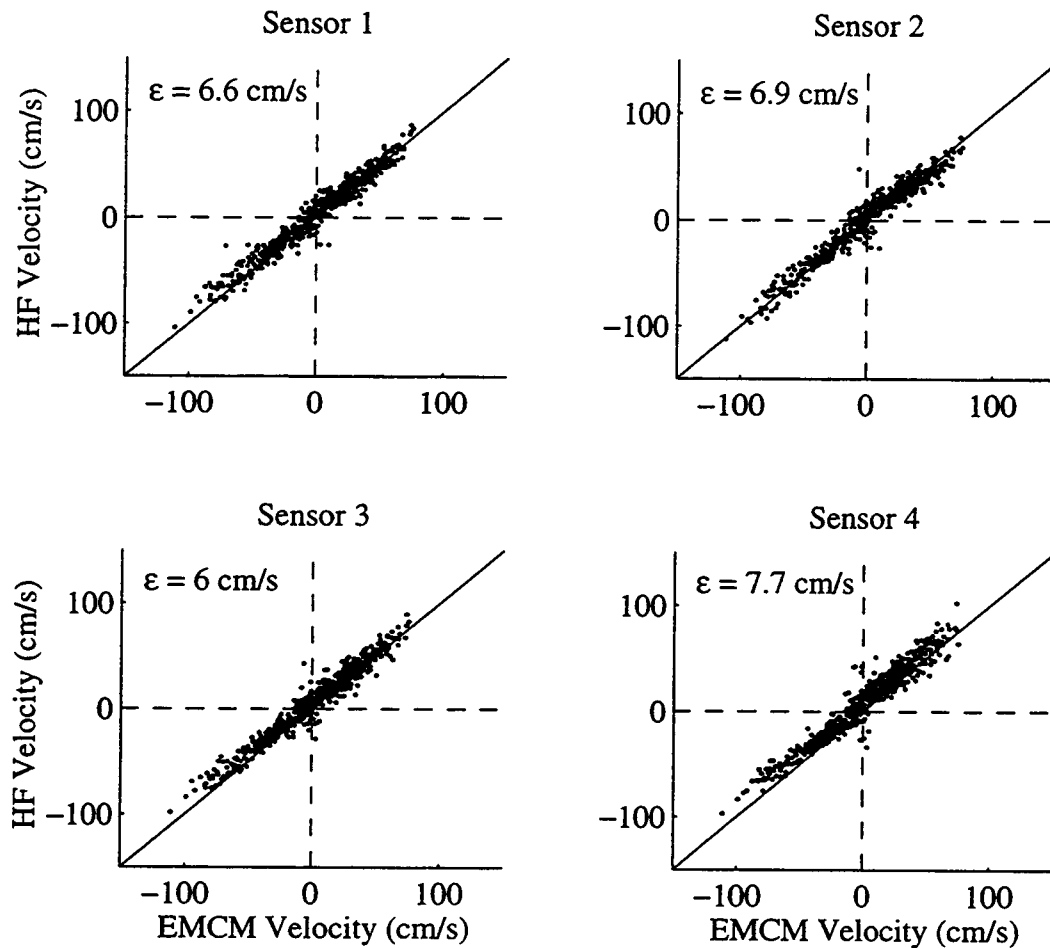


Figure III.4. Comparison of the cross-shore velocities as measured by the electromagnetic current meter (EMCM) and the calibrated, drectified cross-shore velocities as measured by hot film sensors (HF1-HF4) . Each record has been digitally low pass filtered to 1 Hz. The rms deviation, ϵ , between the EMCM and each HF is specified for each comparison.

the lower sensors which experienced burial. When the median was at least 15% of the saturated concentration, the sensor was assumed at or below the water-bed interface. This 15% criteria was determined by visually examining the record. FOBS sensor 5 was not operational, consequently a mean elevation between FOBS sensors 4 and 6 were assumed. Each FOBS sensor is independently examined to determine if it is buried. The final bed elevation is defined as the distance between the lowest hot film sensor and the bed, Figure III.5 (bottom panel). The resolution of this estimate at the FOBS probe was assumed to be \pm one half of the separation between the neighboring FOBS sensors. The maximum slope difference between the bed and instrument cantilever was estimated as 2° , resulting in an additional potential bed elevation uncertainty between the FOBS and the hot film array of 0.5 cm. This was added to the total uncertainty.

III-4. Results

III-4.1 Evidence of the WBBL

To acquaint the reader with the observations, Figure III.6 shows a two minute time series segment of the four near bed velocities, measured by the calibrated derectified hot films (HF1-4), and the free stream velocity, measured by the EMCM. The near bed velocity records show fluctuations over both wave and turbulent bands. Consistent with WBBL theoretical predictions, the nearbed HF observations show strong coherence, but with a decrease in wave amplitude decreasing with sensor elevation. Nearbed flow amplitudes are still large, at 1.3 cm above the bed there exists a strong wave signal with maximum velocity magnitudes of up to 100 cm/s. Also visible in the hot film records are the turbulent fluctuations, which are of significantly lower magnitude and generally increase with increasing free stream velocity.

An example 20 second time series, which has been filtered with a 1 Hz low pass filter to isolate the wave frequencies, also shows a decrease in amplitude with proximity to the bed, Figure III.7. Peak negative velocities (wave crest) at the lowest elevations occur prior to the peak at subsequent upper sensors. This is consistent with simple theory which predicts a phase lead relative to free stream velocity (or potential flow) with increasing proximity to the bed.

An example of the vertical structure of the cross-shore velocity over two consecutive waves in Figure III.7 (224 seconds to 234 seconds) is shown in Figure III.8. In agreement with the phase lead predicted by simple theory, the sensor closest to the bed in panels II and III reverses direction prior to the free stream velocity reversal. Larger vertical shears of the cross-shore velocity are present in the first 5 second (224.5 to 229.5 seconds) wave than in the following smaller amplitude 3.5 second (229.5 to 233 second)

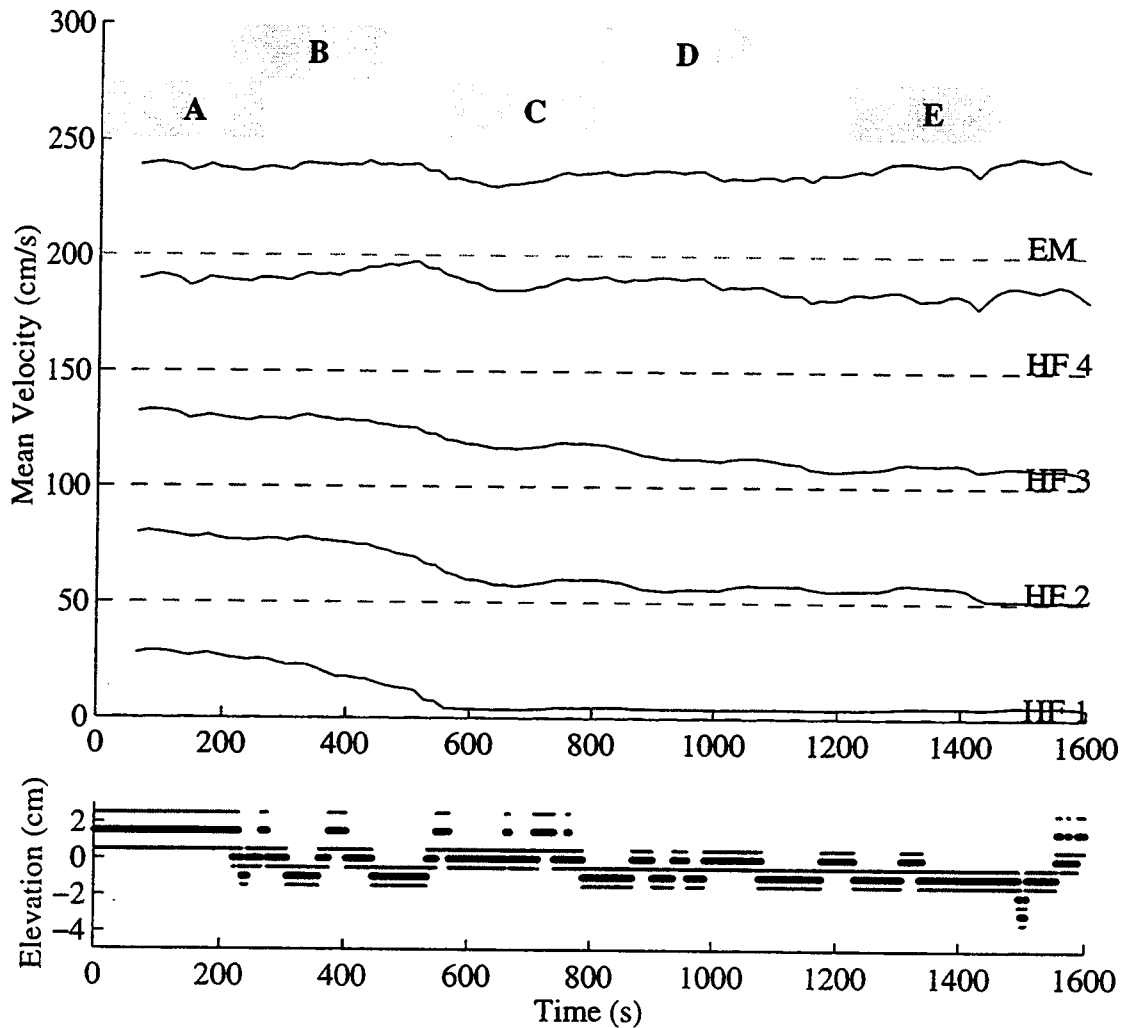


Figure III.5. Time varying mean velocity at five elevations above the bed over consecutive 128 second windows (top panel). Each record is offset from the previous by 50 cm/s. The array spacing of HF1 - HF4 is one cm. The shaded bars A-E indicated five 256 observation segments. Distance of lowest hot film (HF1) to bed as estimated by the FOBS (bottom panel). Note that negative elevations indicate that HF1 is buried. The maximum possible error bounds each estimate and is indicated with the thinner lines.

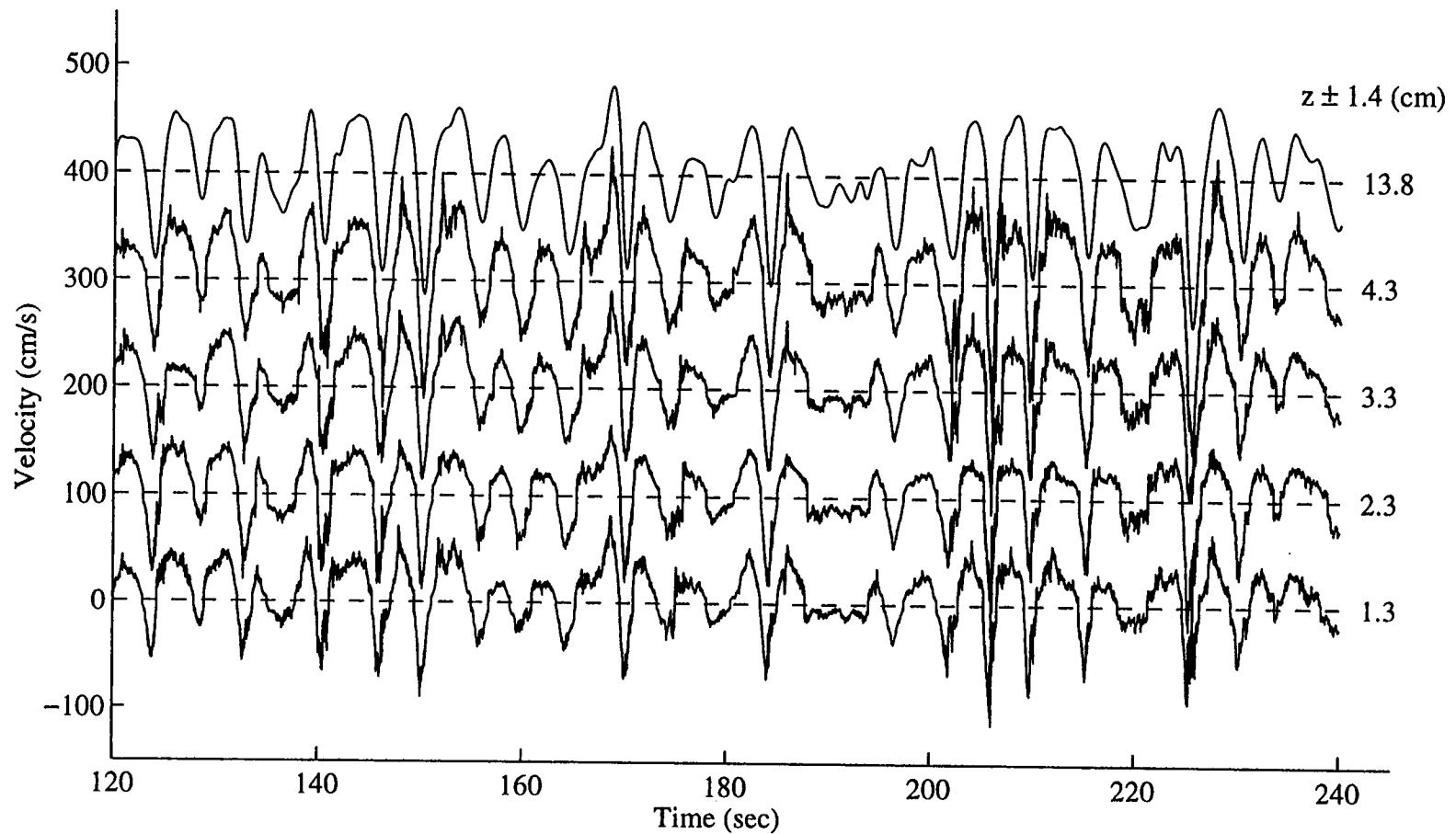


Figure III.6. A 2 minute time series of the derectified calibrated velocity as measured by 4 hot film anemometers within the wave bottom boundary layer and in the free stream as measured by an EMCM. The average distance of each sensor from the bed as measured by the FOBS over the 2 minute record is listed in the right hand column. Each time series is offset from the others by 100 cm/s. Onshore directed flow is indicated with negative velocities and offshore flow is indicated with positive velocities.

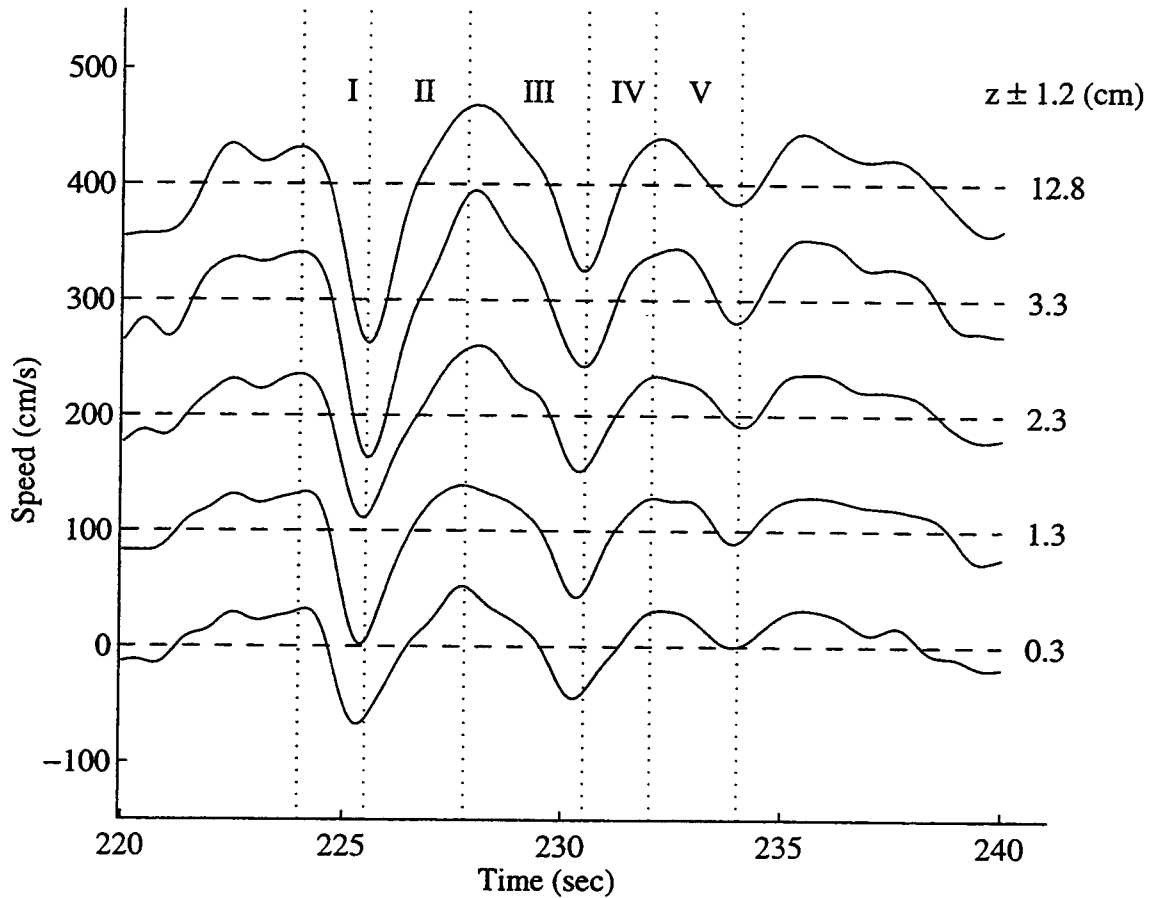


Figure III.7. An example 20 second time series of the near bed velocities showing the amplitude decay and phase lead in the lower sensors which is consistent with the simple wave bottom boundary layer theory. Each sensor has been digitally low pass filtered to removed turbulent fluctuations higher than 1 Hz. Each time series is offset from the previous by 100 cm/s.

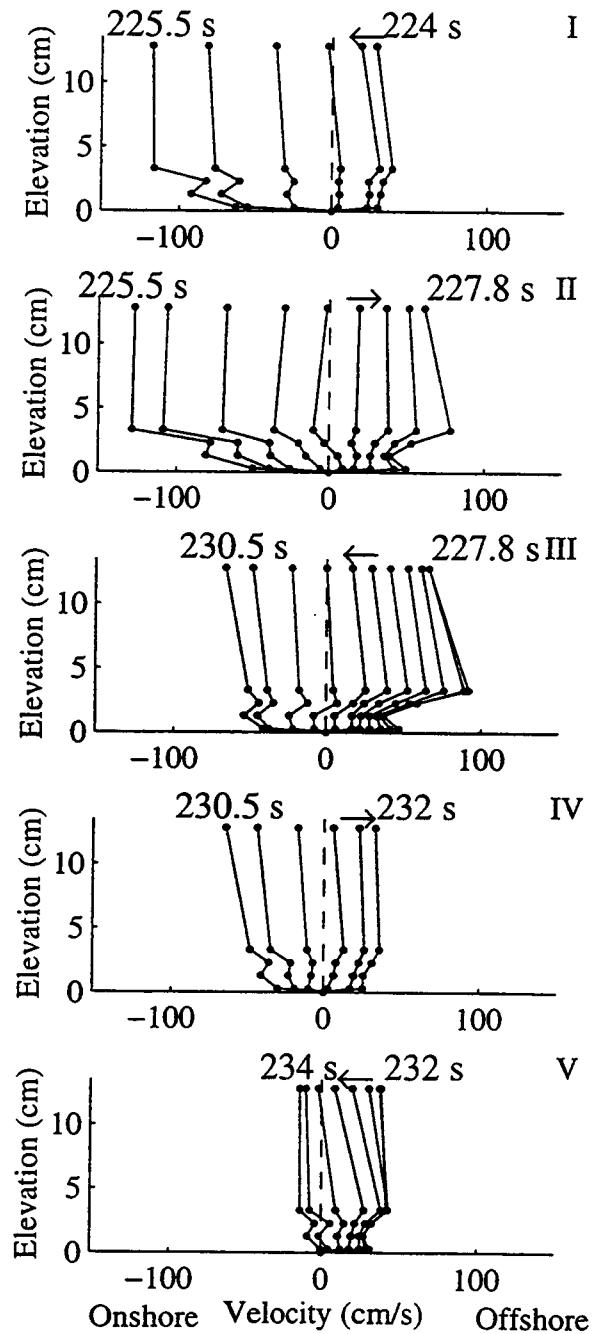


Figure III.8. Vertical structure of low passed cross-shore velocity at the five 0.25 s intervals (I, II, III, IV, V) as specified in Figure III.7. In this figure, the velocity at the seabed is been assumed to be zero. Arrows indicate the direction of time between samples.

wave. Although the general trend of the velocity is to decrease with decreasing elevation, there still exists significant complexity in the vertical structure. Large velocities are present even in the sensor which is closest to the bed, for example in panel II the velocity is as large as 50 cm/s at 0.3 cm above the bed. The scaling of these two waves suggest visual support for the premise that the boundary layer thickness and bed shear velocity scale with wave frequency and free stream wave amplitude, as in (III-4) and (III-5). This is more rigorously tested at the end of this section. Also, the change in the boundary layer structure over the two consecutive waves implies that the boundary layer may respond to changing free stream wave forcing within a wave period.

III-4.2 Statistical Boundary Layer Scalings

The seabed elevation trended upward over the course of the 34 minute record, consequently the record was partitioned into five (A-E) quasi-stationary 256 second segments of data during which the bed elevation remained constant. The variance appeared relatively uniform at each elevation and over each segment, Figure III.5. For each 256 second data segment, the bed elevation was assumed to remain steady and was represented by the average bed elevation. The input wave conditions over the 5 segments were also considered unchanged.

The velocity spectra for segments A and C show that for three of the four hot film sensors the total velocity variance decreases with proximity to the bed, Figure III.9. The velocity variance for all sensors within the WBBL in segment C is lower than that in segment A because the bed accreted between the two runs and caused the sensor array to be closer to the bed. A break in slope of the HF spectra occurs around 1 Hz and may be indicative of a shift from dominance of wave motions to dominance of turbulent motions. This break is less obvious in sensors that are closer to the bed which have lower incident band energy. As indicated in Chapter II, this may be attributed to WBBL nonlinearities whose energy transfer from the incident to higher frequencies is highest near the bed [Trowbridge and Madsen, 1984;]. Also, motions closest to the bed may have a higher frequency at which turbulence begins, due to the smaller length scales, z ($f \sim u/z$).

The rms velocity for each segment (A-E) at each elevation is shown in Figure III.10. An allowance was made for variation in the estimate of the bed elevation by adding and subtracting the time-averaged maximum error as estimated in the previous section (Figure III.5) to the average bed elevation over each record (see vertical error bars). The rms deviation, ϵ , over the incident band between the EMCM and each HF as determined during calibration (see Figure III.4) and is indicated with horizontal bars. With the exception of HF4, the variance decreased with decreasing sensor elevation, showing similar

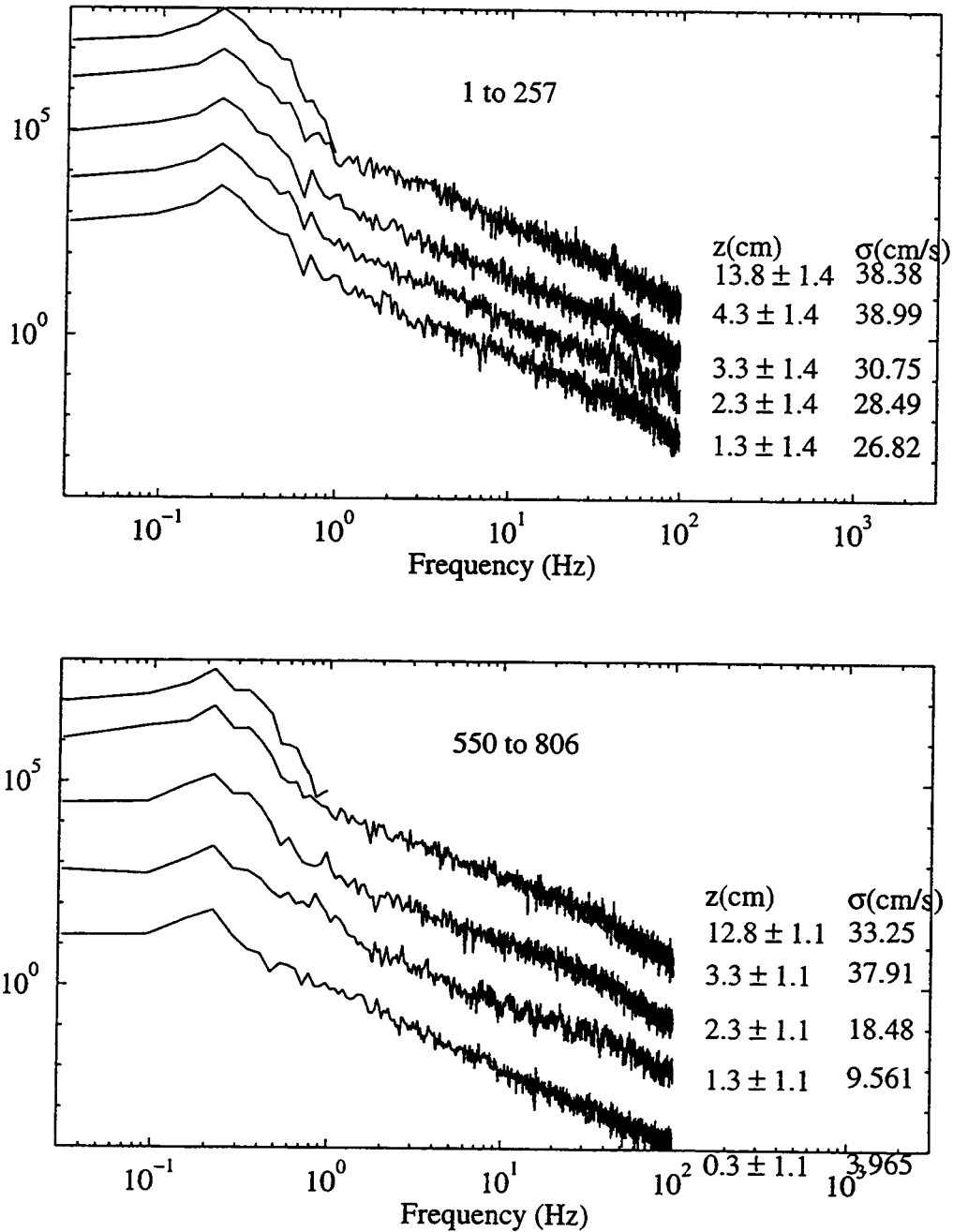


Figure III.9. Energy density spectra as a function of frequency over segments A (top) and C (bottom). Each sensor is offset by 1 decade from the previous sensor. The right hand columns show the time averaged bed elevation estimate of the record and the standard deviation at each elevation.

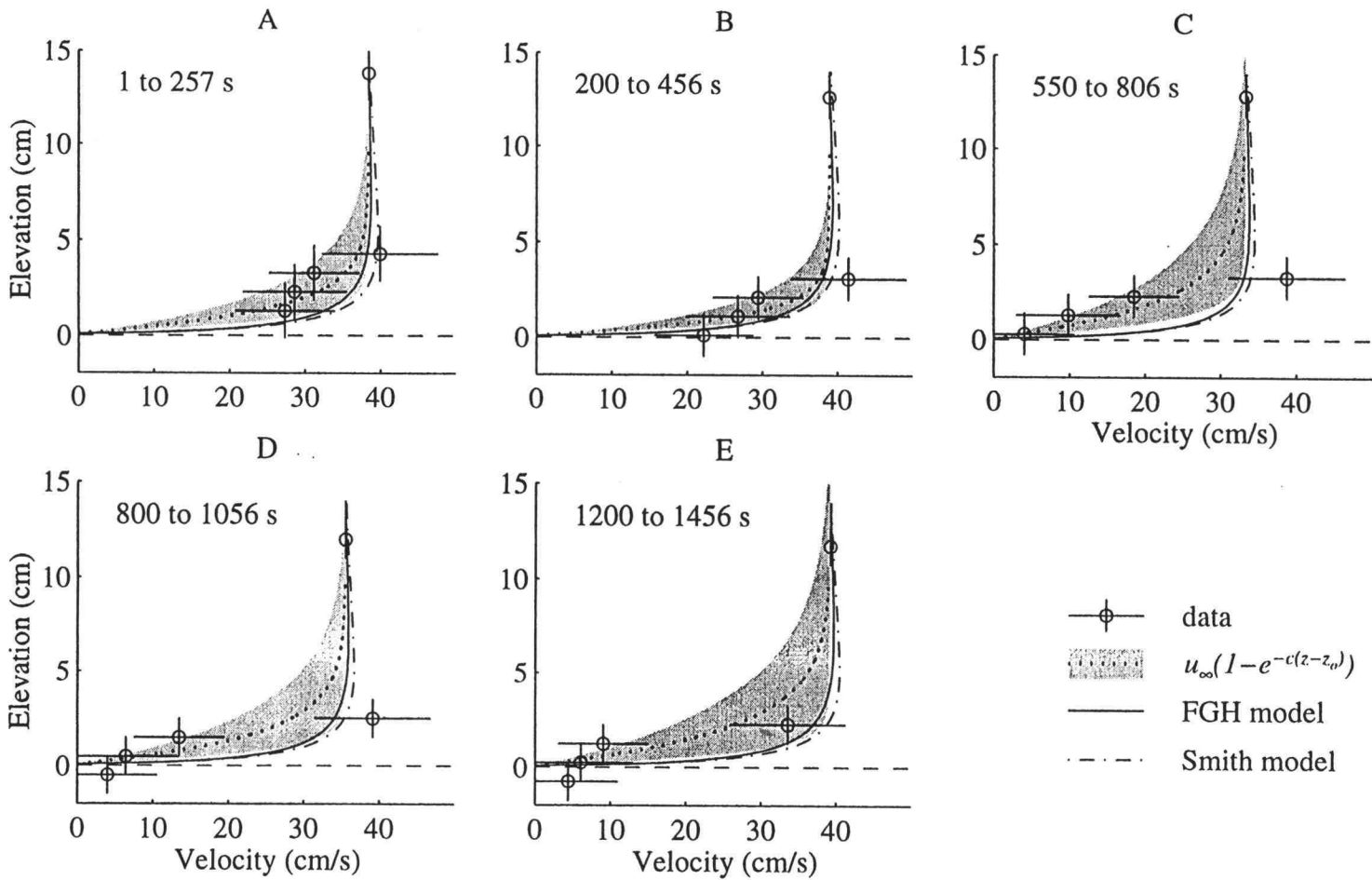


Figure III.10. The root mean square (rms) velocity over each segment (A-E) of the data (o), the Smith model (- -) and the FGH model (—). The vertical error bars indicate the maximum deviation in bed estimate of each quantity about the observations (o). The horizontal bars about the data indicate $\pm \epsilon$. The solid line represents a nonlinear least squares fit of the observations and the shaded area indicates the variation in this estimate if the bed is moved \pm maximum bed estimation error.

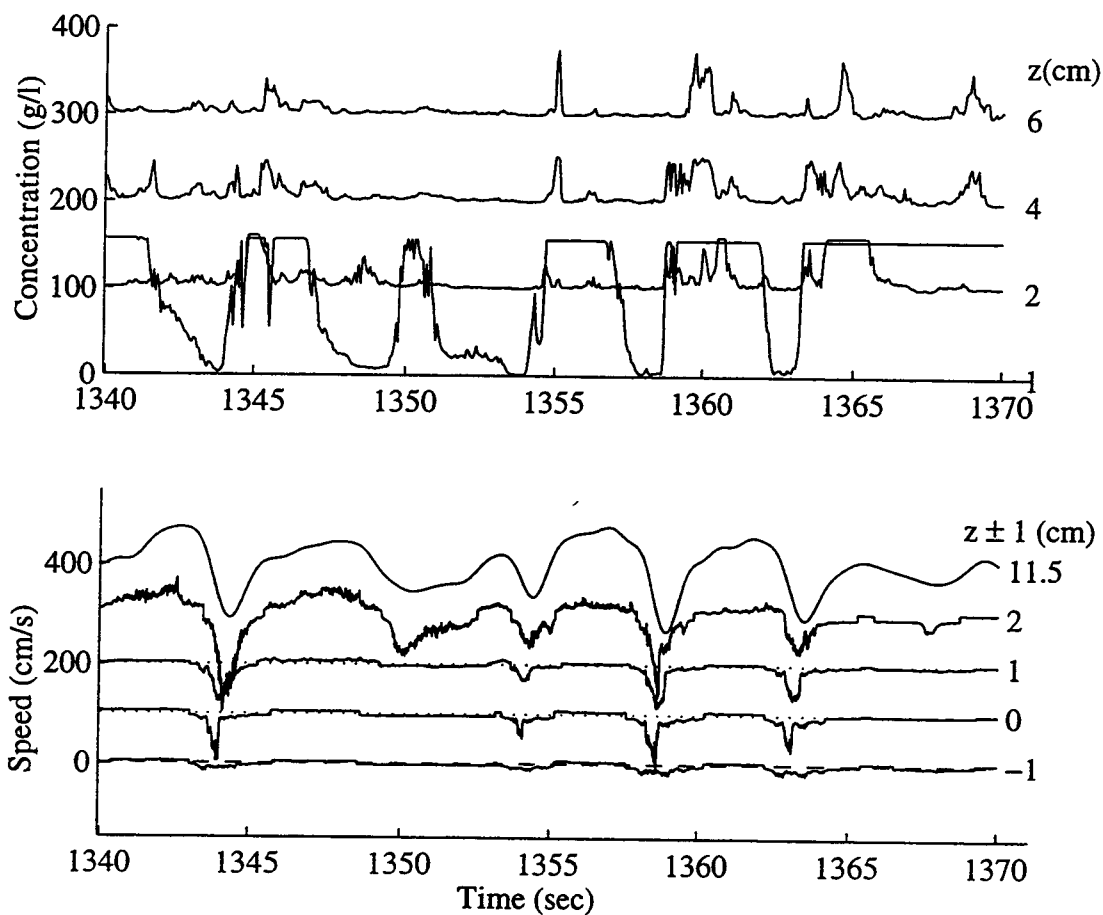


Figure III.11. A 30 second time series of velocity (top panel) and concentration (bottom panel) showing a temporary bed mobilization under several crests. Each velocity and concentration record is offset by 100 cm/s and 100 g/l, respectively. Notice that in each case a suspension event occurs following the erosion of the lowest FOBS sensor.

trends in all five segments. When a sensor is assumed to be buried (negative elevations), as in segments D and E, the rms velocity is non zero and can largely be attributed to large onshore velocities which temporarily mobilize the bed (e.g. Figure III.11). These occasional crests can mobilize the bed, expose buried sensors, and suspend sediment in the water column. Following passage of the wave the sediment settles out of the water column and reburies the sensors. This example highlights the difficulty of applying simple theory to the observations when the bed location is variable and represented with a statistical quantity. For the following, the statistics derived from the hot film observations were calculated by neglecting velocities at $z < z_o$, when the sensors were assumed to be zero.

The rms velocity observations were fit with a nonlinear least squares exponentially decaying regression model defined with

$$u(z) = u_{\infty} \left(1 - e^{-c(z-z_o)}\right), \quad (\text{III-21})$$

where c is the single free parameter. For consistency with classical theory, the velocity at the lower boundary ($z=z_o$) is forced to be zero. However, the form of (III-21) was chosen to also force the shear at the upper boundary to approach zero. The bed roughness (z_o) was fixed at 0.08 cm [Beach and Sternberg, 1992]. The shaded areas in Figure III.10 indicate the maximum deviation of the regression assuming the maximum range in bed level fluctuations.

For each data segment, the monochromatic Smith model was evaluated at the peak frequency with a free stream amplitude chosen to match the total free stream velocity variance. Bed roughness was assumed to be $z_o=0.08$ cm. The Smith model predicts an rms velocity structure of the same order of magnitude as the observations, but generally predicts larger near bed velocity shear and a smaller boundary layer thickness than is present in the observations, Figure III.10. The rms deviation between the measured and calculated rms velocity profiles as defined with

$$\left(\Delta u_{s_{rms}}(z)\right)_{rms} = \left(\frac{1}{N} \sum_{n=1}^N \left(u_{s_{rms}}(z_n) - u_{D_{rms}}(z_n)\right)^2\right)^{\frac{1}{2}}, \quad (\text{III-22})$$

where N is the number of hot films ($N=4$) and u_D is the measured velocity at each elevation. $\left(\Delta u_{s_{rms}}(z)\right)_{rms}$ has a mean value over the five segments, $\left\langle \left(\Delta u_{s_{rms}}(z)\right)_{rms} \right\rangle$, of 12.3 cm/s, and is given for each of the five segments in Table III-2. Note that $\langle a \rangle = \frac{1}{5} \sum_{p=1}^5 a_p$

indicates the average of any given quantity (a) over the five data segments, and $\bar{a} = \frac{1}{N} \sum_{n=1}^N a_n$ indicates the vertical average over the four hot film sensors. The rms velocity structure predicted by the FGH model for each data segment is also compared with

the observations and the Smith model in Figure III.10. The model is forced with the free stream velocity at 14 cm above the bed, the bed elevation is assumed constant over the record, and the bed roughness is assumed to be 0.08 cm. The rms velocity structure predicted by the FGH model is of similar shape to the Smith model, Figure III.10. As defined in (III-22), the rms deviation between the measured and FGH model predicted rms velocity has a mean value, $\langle (\Delta u_{FGH_{rms}}(z))_{rms} \rangle$, of 11.6 cm/s, and is given for each of the five segments in Table III-2. The rms deviation averaged over the HF sensor array between the time varying FGH model calculations and the observations is defined with

$$\overline{(\Delta u(z,t))_{rms}} = \frac{1}{N} \sum_{n=1}^N \left(\frac{1}{M} \sum_{m=1}^M (u_{FGH}(z_n, t_m) - u_D(z_n, t_m))^2 \right)^{\frac{1}{2}}. \quad (\text{III-23})$$

Table 3 shows statistics for the mean value, $\langle \overline{(\Delta u(z,t))_{rms}} \rangle$, 15.4 cm/s, and for each data segment.

	A	B	C	D	E	mean
$(\Delta u_{FGH_{rms}}(z - \Delta z))_{rms}$	2.8	4	6.9	8.2	4.5	5.3
$(\Delta u_{FGH_{rms}}(z))_{rms}$	5.6	10	13.3	14.1	15.1	11.6
$(\Delta u_{FGH_{rms}}(z + \Delta z))_{rms}$	7.6	8.5	18.6	18.7	20.4	14.8
$(\Delta u_{S_{rms}}(z - \Delta z))_{rms}$	3.5	3.1	6.5	7.7	4.5	5.1
$(\Delta u_{S_{rms}}(z))_{rms}$	6.9	10.2	13.7	14.5	16	12.3
$(\Delta u_{S_{rms}}(z + \Delta z))_{rms}$	8.3	9.2	19.3	19.5	21.6	15.6

Table III-2. Depth root mean square deviations between two models (u_{FGH} and u_S) and the data (u_D) $z=z\pm\Delta z$ of the rms velocity in the five segments A-E. $z-\Delta z$ indicates the sensor array is Δz closer to the bed and $z+\Delta z$ indicates the sensor array is Δz away from the bed.

	A	B	C	D	E	mean
$\overline{(\Delta u(z - \Delta z, t))_{rms}}$	14.3	19.2	11.3	9.9	9.9	12.9
$\overline{(\Delta u(z, t))_{rms}}$	13.7	16.3	16.8	14.4	15.9	15.4
$\overline{(\Delta u(z + \Delta z, t))_{rms}}$	14.7	18.8	22.3	25.7	31.6	22.6

Table III-3. Depth averaged temporal root mean square deviations between the FGH model (u_{FGH}) and the data (u_D) $z=z\pm\Delta z$ of the time varying velocity in the five segments A-E. $z-\Delta z$ indicates the sensor array is Δz closer to the bed and $z+\Delta z$ indicates the sensor array is Δz away from the bed.

The average vertical structure of the phase over each of the five segments was evaluated by determining the time of maximum correlation between each of the hot film velocities and the free stream velocity as measured by the EMCM, Figure III.12. The cross correlation is restricted to a temporal resolution equal to the sampling interval of the EMCM(1/16 s). Furthermore, considering that the true response of the EMCM is 2 Hz, the 1/16 s interval is only valid for relative comparisons between the HF sensors. In agreement with simple WBBL theory, within the WBBL the velocity phase lead increases with decreasing sensor elevation. This relationship is readily apparent in Figures III.7, 8, and 11. Time shifts of both boundary layer models also increases with proximity to the bed, but is larger than the observations by approximately a factor of two, Figure III.12. Both models predict a maximum velocity lead relative to that of the free stream velocity of .31 s at the bed.

The bed shear velocity of the rms velocity observations was determined in two ways, Figure III.13. First, u_{*o} as defined in (III-15) was determined with the exponentially decaying regression model, as given in (III-21). This quantity remains relatively uniform over the five segments and has a mean value of 1 cm/s. In addition, the bed shear velocity was estimated with a two parameter logarithmic nonlinear least squares regression model,

$$u(z) = \frac{u_{*o}}{K} \ln\left(\frac{z}{z_o}\right) \quad (\text{III-24})$$

where the two free parameters are the bed shear velocity (u_{*o}) and the bottom roughness (z_o). Both the observations and models rely on an estimate of the bed roughness (z_o), which is difficult to measure under the simplest conditions and poorly constrained under movable beds. In this paper, we have assumed a uniform value of 0.08 cm for all the

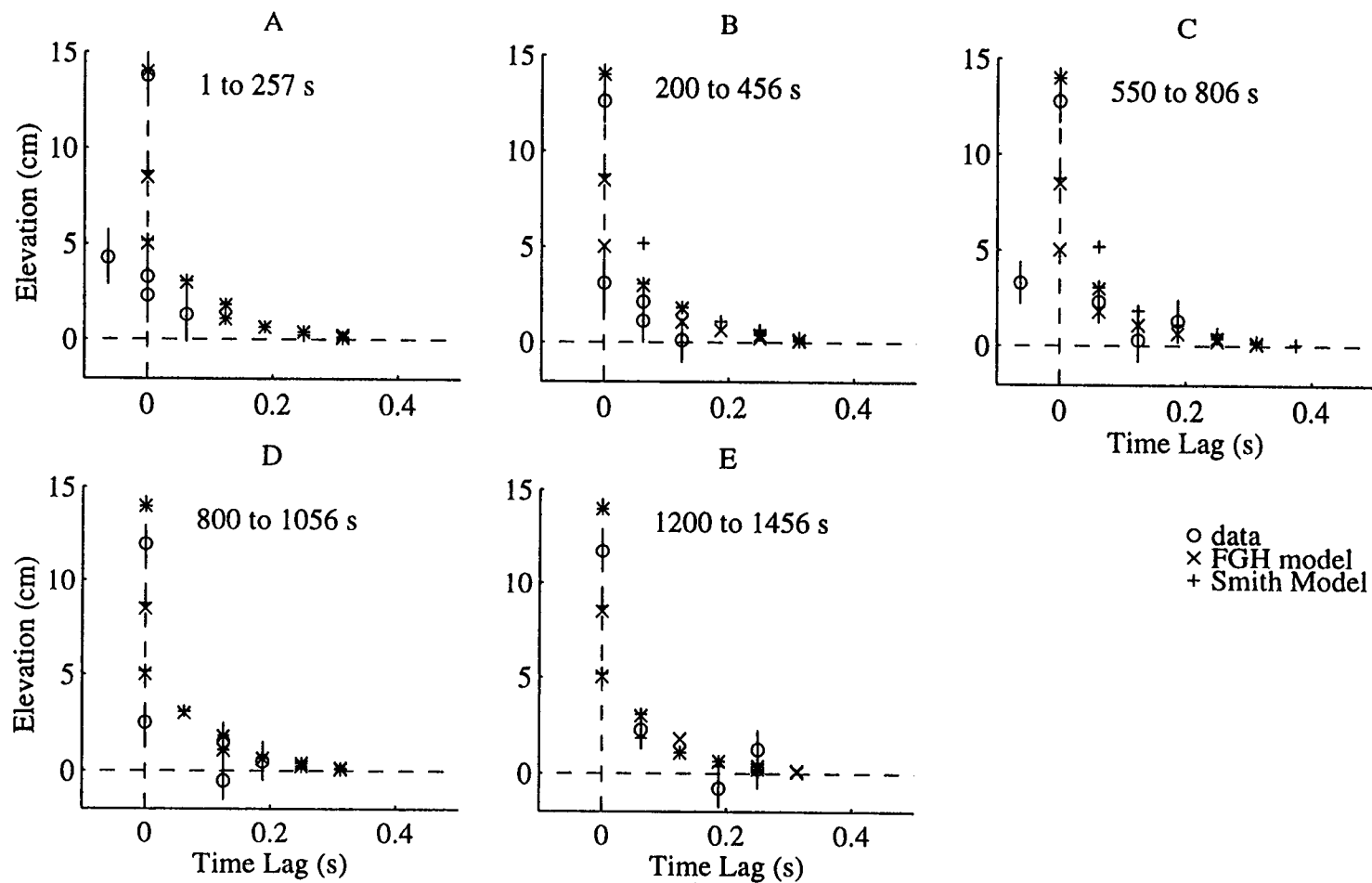


Figure III.12. The time lag at maximum correlation between the EMCM and each HF over each segment (A-E) of the data, the Smith model and the FGH model. Positive lags indicate a time lead. The vertical error bars indicate the maximum deviation of each quantity due to the maximum deviation in bed estimate about the observations (o).

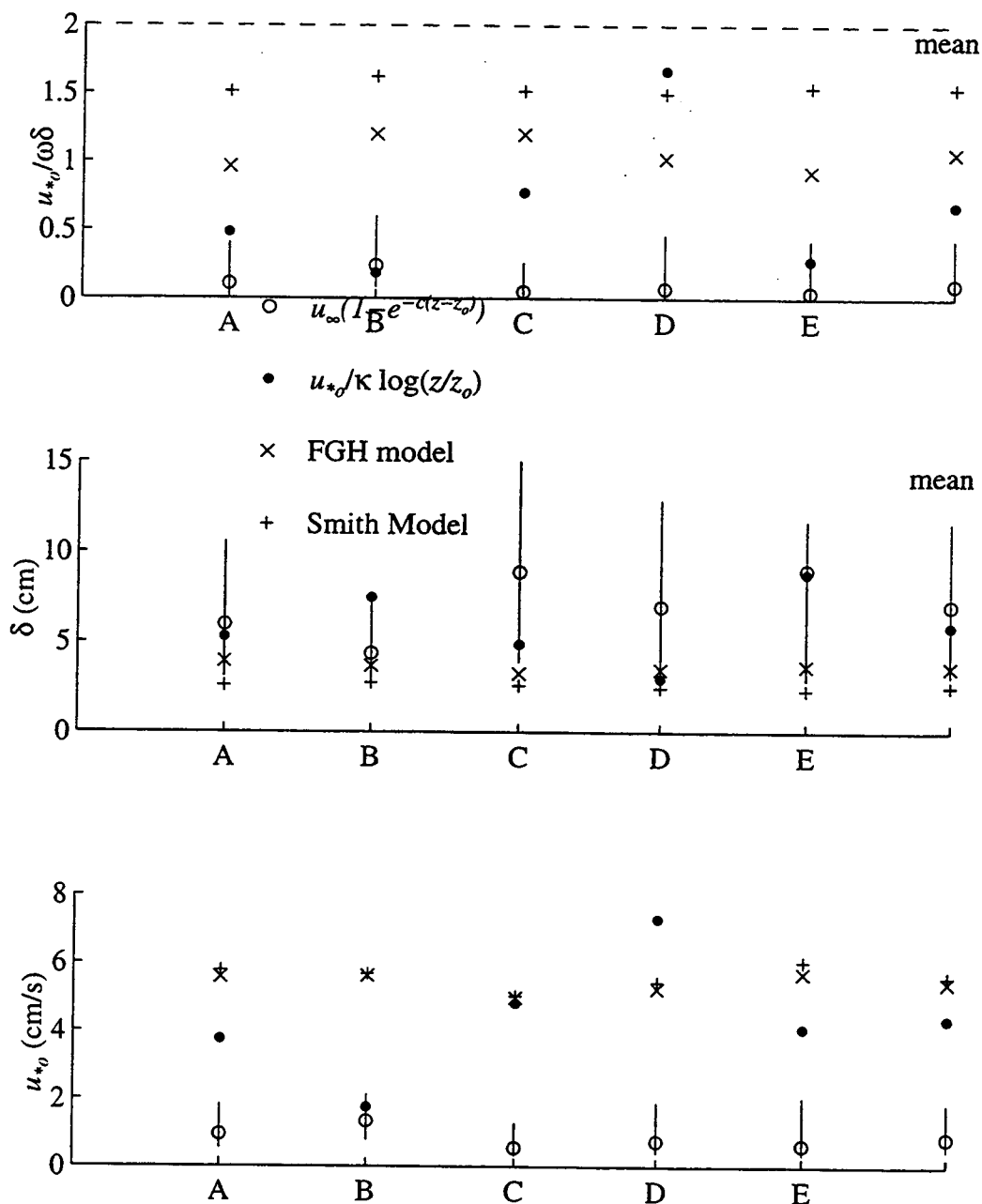


Figure III.13. The ratio of the shear length scale to the boundary layer thickness, (top panel) boundary layer thickness (middle panel), and bed shear velocity (bottom panel), of the rms velocities of the two regression models and two WBBL models for each segment (A-E). The error bars indicate the maximum deviation of each quantity about the exponential decay regression (o) due to a possible deviation in the bed estimate.

investigations, as in Beach and Sternberg [1992]. The logarithmic model is not constrained to have zero shear at the uppermost boundary, thus, only 4 HF sensors within the boundary layer were regressed. The bed shear velocity over the five segments is less stable and significantly higher than the result for the exponentially decaying regression model and has a mean value of 4.3 cm/s. The estimates of the bed shear velocity of the rms velocity with the Smith model and FGH model as determined with (III-15) vary only slightly over the five segments and of comparable magnitudes, 5.6 cm/s and 5.4 cm/s, respectively. The model predictions are significantly higher than the observations fit with the exponential formulation (III-21) and only slightly higher than the fit with the logarithmic regression model (III-24), see the bottom panel of Figure III.13.

The rms boundary layer thickness (δ), defined as the elevation at which the rms velocity reaches 99% of the free stream velocity was calculated for the observations fits and models, and is shown in Figure III.13. The average boundary layer thickness ($\langle \delta \rangle$) is 7.0 cm for the exponentially decaying regression model. There exists a large variability (3.1-11.6 cm) in the estimate of the $\langle \delta \rangle$ with the observations, because of the sensitivity of the estimate on the individual sensor gain and on the shear near the free stream. Also having high variability, the logarithmic regression predicts a smaller value of 5.9 cm. The Smith model predicts a mean boundary layer thickness of 2.2 cm and the FGH model predicts a larger value of 3.6 cm.

Equation (III-4) defines that the boundary layer (δ) is proportional to the length scale required to diffuse the shear produced at the bed ($\sim u_* / \omega$). When the velocity is a maximum and the may be considered to have a logarithmic profile, as in (III-4), the ratio $u_* / \delta \omega$ has been assumed to equal 2 by some investigators [Beach and Sternberg, 1992]. For this investigation, the shear length scale is defined with u_* / ω . The estimates of the shear length scale and the boundary layer thickness are compared in Figure III.13. The field observations indicate a shear length scale of only 10% (regression model) of the observed boundary layer thickness, whereas the FGH and Smith models predict ratios of 1.1 and 1.5, respectively. Our confidence in the estimate of u_* is greater than that of δ , consequently this would surprisingly suggest that the estimates of δ are high by a factor of 10. While there are certainly inaccuracies in the estimate of these parameters with the observations, this ratio is low by an order of magnitude and would suggest that further thought and investigation on this topic are required.

III-4.3 Frequency Structure

The amplitude and phase structure of the velocity observations and the FGH model predictions are analyzed with frequency domain empirical orthogonal functions (CEOF)

of the cross spectral matrix of segments A-E [Wallace, 1972], Figure III.14. The amplitude has a similar structure at all frequencies, although there is a slight decrease in velocity shear with increasing frequency. If each frequency were acting independently, linear theory in (III-4) and (III-5) would predict that the boundary layer thickness would roughly be proportional to the wave frequency. Of the four frequencies shown here, linear theory would predict that the boundary layer thickness should decrease from $10u_*o$ to $0.7u_*o$. These observations indicate that the frequencies are not independent of one another. The FGH model is in qualitative agreement with this and shows a decrease in the overall shear with frequency. However, as with the observations it does not show the decrease in boundary layer thickness which is predicted with linear theory.

The observations show that the phase shift, ϕ , is smallest at the incident peak ($\phi_0 < 10^\circ$). Linear theory would predict that the phase shift at a particular elevation should decrease with increasing frequency as the each sensor's relative position within the WBBL thickness increases. The observations show that at the highest frequency ϕ_0 is 30° . This also indicates that the frequencies are not acting independent of each other. Furthermore, the observations would suggest that the lead produced by the stress gradient is smaller than previously thought and consequently momentum is being mixed more rapidly within the boundary layer. This is also supported by the lower than expected shears present in the amplitude structure. The results from Chapter II would suggest that this increase in the phase is characteristic of an increasing effect of the near bed nonlinearities. However, the FGH model predicts a phase structure which is relatively constant as a function of frequency, also indicating an effect of the nonlinear terms throughout the incident band. The FGH model shows qualitative agreement at .1 and .6 Hz, but predicts significantly higher phase shifts at the dominant incident peak, .2 Hz and .4 Hz.

III-5. Conclusions

In this paper, we presented a comprehensive set of observations of the wave bottom boundary layer which were used to investigate the actual amplitude and phase structure of the surf zone WBBL, and evaluate the theoretical scalings of boundary layer thickness, bed shear velocity, and bottom roughness. The observations were made on the Outer Banks of the North Carolina coast and collected during the collective Duck94 field experiment. Velocity observations were made with a vertical array of four hot film anemometers. Simultaneous bed level measurements were made with a fiber-optic back scatter sensor probe. Over a 34 minute record, five 256 second time series were used to investigate the structure and dynamics of the wave bottom boundary layer.

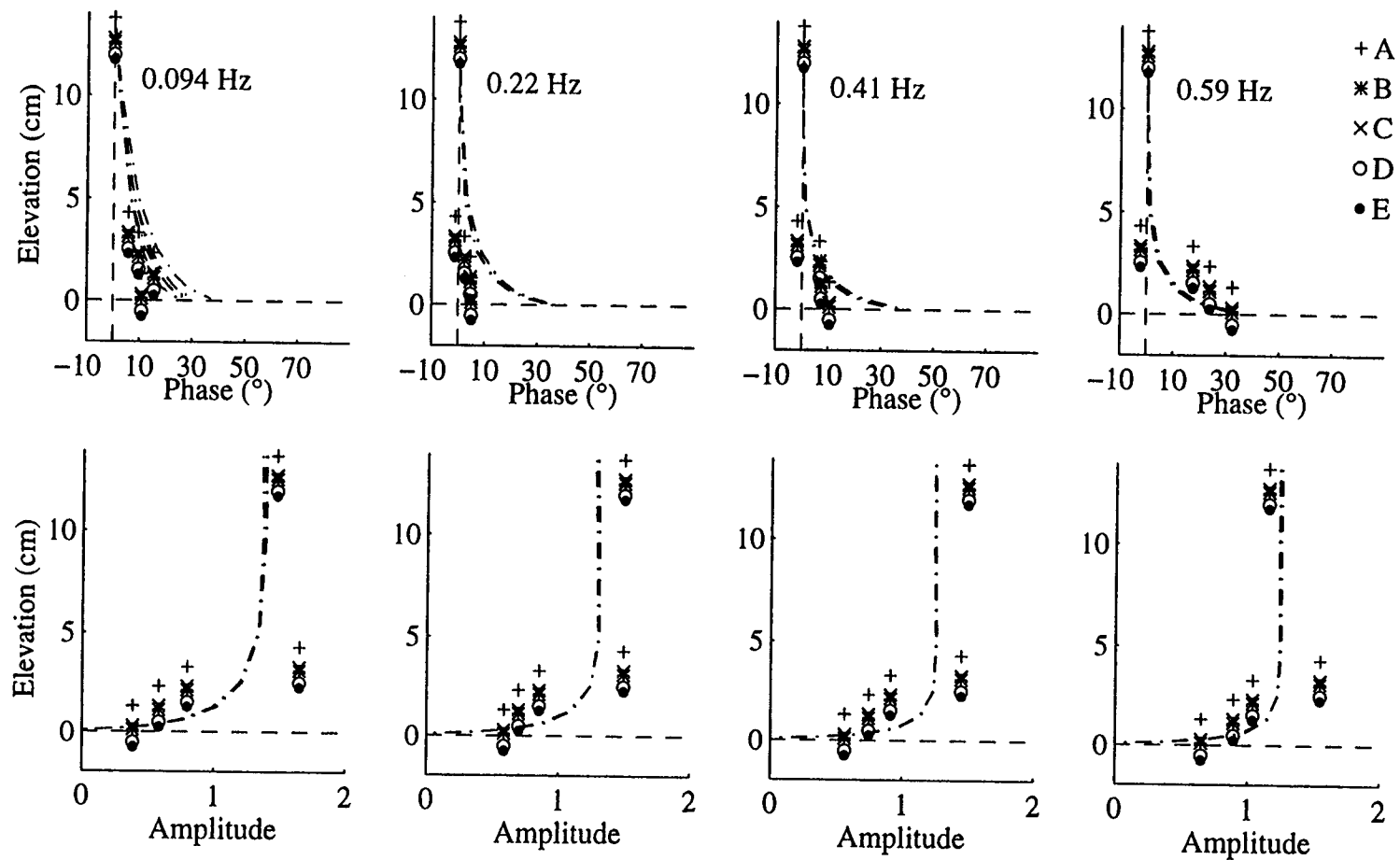


Figure III.14. The complex domain empirical orthogonal function (CEOF) of the cross spectral matrix at several frequencies within the wave frequency band. At each frequency the amplitude is in the lower panels and the phase is in the upper panels. Each cross spectral calculation is computed 32 degrees of freedom. The incident peak occurs at 0.22 Hz.

The bed elevation was shown to vary over the course of the 34 minute record. Even over shorter 4 minute records, the bed was temporally mobilized during extreme waves. This resulted in mean rms statistics which showed non-zero velocities at mean elevations which were below the assumed bed. This phenomena made comparisons with simple models difficult at best. The observations showed a decrease in rms velocity and an increase in phase with proximity to the bed.

There exists several indications which suggest that momentum was being more rapidly mixed through the WBBL than simple theory predicted. First, as shown in the rms velocity and the frequency domain empirical orthogonal functions, smaller, near linear shears were present throughout the WBBL. Secondly, smaller phase shifts were found in both the averaged time leads and the frequency phase structure.

A nonlinear exchange of momentum was supported by both the amplitude and phase frequency vertical structure. Linear theory would predict the boundary layer thickness would decrease with increasing frequency. In the observations, this would result in increasing the sensor array's relative position within the boundary layer. Consequently each sensor should show a decrease in phase and increase in amplitude relative to the free stream velocity. However, the phases were shown to increase with frequency and the vertical shears were shown to decrease slightly, indicating that the response of the WBBL is not independent of frequency.

Comparisons of the rms velocity and phase structure predicted by the two models showed essentially indistinguishable results. Depending on the true mean elevation of the bed, the rms deviation between the rms velocity observations and the FGH and Smith models ranged from 5.3 - 14.8 cm/s and 5.1 - 15.6 cm/s, respectively. Although the FGH model is computationally more intensive, it has the added appeal of predicting the WBBL temporal structure under a random wave field. The FGH model showed qualitative agreement with observations of the frequency structure of the velocity amplitude. However, predictions of the phase structure were not in agreement with the observations. The poor phase comparisons may be due to 1) the no-slip condition imposed at the bed, 2) neglecting the nonlinear advective terms, or 3) inadequate description of the actual mixing of momentum.

The observations were used to evaluate the bed shear velocity, and boundary layer thickness of the rms cross-shore velocity structure. Smaller shears in the observations yielded estimates of the bed shear velocity and boundary layer thickness of 1 cm/s and 7 cm, respectively. The observed boundary layer thickness was significantly larger than estimates of the shear length scale. Even though the confidence in the estimate of the boundary layer thickness was not high, the estimate of u_{*o} would require a boundary layer

thickness of less than 1 cm for the relationship to hold. The two models predicted similar bed shear velocities of 5.4 (FGH) and 5.6 (Smith) cm/s, significantly higher than the observations. Both of the models predicted shear length scales which are approximately equal to the predicted boundary layer thicknesses.

These observations are among the first coherent looks at wave bottom boundary layer in the surf zone under conditions of significant sediment response and highlight the added complexity of the dynamics in natural environments. Future investigations may include the quantification of the effect of bed roughness, and the temporal generation and dissipation of turbulent kinetic energy in the wave bottom boundary layer.

CHAPTER IV: OBSERVATIONS OF TURBULENCE IN THE NEARSHORE WAVE BOTTOM BOUNDARY LAYER

IV-1. Introduction

IV-1.1 Motivation

In energetics based sediment transport models, the transport of suspended sediment is assumed to be proportional to the time averaged energy dissipation by the fluid on the bottom [*Bagnold*, 1963; *Bowen*, 1980; *Baillard and Inman*, 1981],

$$i_s \propto |\mu\tau_b|, \quad (\text{IV-1})$$

where i_s is the immersed weight transport of suspended sediment, μ is the total cross-shore velocity, and τ_b is the bed stress. Because the actual bed stress is unknown, these models often rely on simple quadratic or eddy viscosity parameterizations. These models assume that the generation of turbulence is solely due to the bottom stress, and predict that the transport of suspended sediment is proportional to the strength of and will oscillate with the wave velocity. Suspended sediment field observations show concentrations which increase with increasing wave strength; however, the concentration spikes are intermittent and not simply proportional to the oscillating wave velocities [*Jaffe et al.*, 1984; *Huntley and Hanes*, 1987; *Hanes*, 1988; *Beach and Sternberg*, 1992]. These observations suggest that suspension events are a result of rapid aperiodic turbulence introduction in the near bed region. The generation of these turbulence events may have its source at the bottom due to bottom shear, within the wave bottom boundary layer due to shear instabilities, and/or near the free surface due to downward advected surface wave breaking.

As fluid moves over the bottom, the velocity approaches zero at the bed in a region called the boundary layer. This reduction of velocity produces a velocity shear which in turn generates turbulence. The continual generation of turbulence acts to provide a net Reynolds stress which acquires momentum from the free stream. Therefore, the turbulence is both caused by shear and produces shear. In other words, the turbulent energy is input at the large wavelengths and continually cascades its energy to small wavelengths until dissipation occurs at the smallest scales. In homogeneous isotropic turbulence, the velocity wavenumber spectra has been shown to follow the universal form of the Kolmogorov wavenumber spectrum:

$$\Phi(k) = \alpha \varepsilon^{2/3} k^{-5/3} \quad (\text{IV-2})$$

where α is a nominal constant (~ 0.5), ϵ is the energy dissipation rate (normalized by density), and k is the wavenumber [Tennekes and Lumley, 1972].

In a wave dominated environment, the size of the boundary layer is limited by the magnitude and period of the waves. The WBBL is under continual development due to the oscillatory nature of the velocity. The velocity oscillations and resulting shear create an unsteady generation of turbulence. Under periods of increasing generation, we expect to see a steeper slope in the velocity wavenumber spectrum because energy is being input faster than it is dissipated. But under periods of decreasing generation, we expect to see flatter slopes because energy is being dissipated faster than it is being generated.

A laboratory investigation of oscillatory flow over a smooth bed found that turbulence generation rates are highest at the beginning of flow deceleration (decreasing velocity magnitude) and that this energy is completely dissipated within the deceleration period [Hino *et al.*, 1983]. A later study of flow over a rough bed found that turbulent intensities are greatest during the flow deceleration period as well [Sleath, 1987]. Sleath's study also found that the Reynolds stress at the bed was approximately in phase with the maximum turbulent intensity. The investigation also found that during the acceleration (increasing velocity magnitude) phase of the flow, the frequency spectral energy slope followed a Kolmogorov $-5/3$ spectrum, but during the deceleration phase of the flow, the spectrum slope was significantly steeper. Under rough-bed oscillatory boundary layers, the near bed turbulent intensities and Reynolds stresses have been found to be 50 % higher than for a smooth bed [Jensen *et al.*, 1989].

The above laboratory investigations have benefited from minimally intrusive, high frequency response Laser Doppler Velocimeters and hot film anemometers. Field observations are limited by an additional constraint of selecting instruments which are capable of surviving the energetic surf zone. Only recently has instrumentation become durable enough to allow for direct turbulence observations in the surf zone. The first field investigation of the development of turbulence in a wave bottom boundary layer (WBBL), mainly relying on visual observations paired with a hot film anemometer, concluded that the flow in a fluid-granular boundary layer undergoes a transition from laminar to turbulent only under wave crests [Conley and Inman, 1992]. An Oregon coast wave bottom boundary layer investigation concluded that suspension events were well correlated with high frequency ($f > 8$ Hz) velocity variance events and that some of those events could have been triggered by a shear instability of the wave bottom boundary layer (Chapter V).

The first quantitative field observations of surf zone turbulence levels found that dissipation rates to vary from $4 \text{ cm}^2/\text{s}^3$ in the lower water column to $200 \text{ cm}^2/\text{s}^3$ at the surface (assuming a 2 m water depth) [George *et al.*, 1994]. They found that estimates of

dissipation rates made with the observations compared well to the bore dissipation model of Thornton and Guza [1983]. The observations also showed estimates of dissipation rates significantly lower than those predicted by lab studies. Dissipation rate estimates are shown to decrease with decreasing sensor elevation (although a slight increase is found at the lowermost position) through the upper 90% of the water column. If turbulence is being generated at the bed, it is conceivable that larger dissipation estimates will be found in the wave bottom boundary layer than in the lower water column.

The observations presented here are the first measurements to examine the temporal and vertical variations of bottom boundary layer dynamics and energetics with simultaneous sediment suspension measurements. A vertical array of four hot film anemometers are co-located with a vertical stack of 20 fiber optic back scatter sensors (FOBS). The unique nature of these measurements will allow us to examine the interaction between waves, turbulence and sediment suspension in the surf zone.

IV-1.2 Objectives

Using data collected during the Duck94 field experiment, we will first evaluate an eddy viscosity model for the vertical and temporal structure of shear stress and examine the consistency with suspended sediment observations. Next, we investigate evolution of the unsteady turbulent WBBL energetics over the phase of the wave. Finally, estimates of the vertical and temporal structure of dissipation rates are compared with estimates of the bed shear velocity. The field observations are summarized in section 2, the results are presented in section 3 and conclusions are given in section 4.

IV-2. Observations

The measurements were collected at the Army Corps of Engineers Field Research Facility in Duck, North Carolina on August 17, 1994 as part of the Duck94 cooperative field experiment. The offshore significant wave height, period and dominant incoming angle as measured at the 8 m array were 0.83 m, 4.54 s, and 50° from the southeast, respectively. The barred beach was composed of well sorted fine grained sand. The observations were made in 2m water depth on the bar crest under a mix of broken and unbroken waves.

Velocity and speed measurements used in this investigation were made with four TSI model 1755 constant temperature cylindrical quartz coated hot film anemometer probes stacked with a 1 cm vertical spacing, and one Marsh-McBirney electromagnetic current meter. The dominant hot film signal is a measure of the total cross-shore velocity magnitude and as used in the investigation has a frequency response of 128 Hz. The calibrated velocity magnitude of each hot film signal was derectified by searching for local

minima around windows of the free stream flow reversal. Sediment suspension was measured at a 16 Hz sampling rate with a 19 sensor fiber-optic back scatter (FOBS) probe. In addition to measuring the sediment suspended in the water column, the FOBS also pierces the bed and measures bed elevation as sensors are alternatively covered and uncovered. The presence of bed forms was determined visually with an underwater video camera. The instruments were deployed from a cantilevered arm attached to the boom of a crane located on the FRF pier. To prevent vibration, a spike attached to the end of the boom was set into the bed and held in place by the weight of the crane. A diagram of the instrumentation package is given in Figure III.2 and the reader is referred to Chapter III for a complete review of the instrumentation capabilities, deployment, and calibration.

Over the course of the 10 minute calibration record and 34 minute WBBL record, the bed underwent both erosion and accretion, causing the hot film array's relative elevation from the bed to vary. We will focus on: (1) five independent 256 sec segments of the WBBL record where the hot film gain and the bed elevation remained uniform and (2) two additional 256 second segments from the 10 minute calibration run, where the sensor elevations were outside the wave bottom boundary layer and varied from 13-17 cm above the bed (see Chapter III). The results shown below are a combination of the seven 256 s records, each with an independent bed elevation. Figure IV.1 shows an example 60 sec time series of cross-shore velocity, high frequency velocity variance, and sediment concentration at several elevations above the bed. Throughout this paper it is assumed that onshore directed flow is negative and offshore directed flow is positive. Figure IV-1 shows that the velocity magnitude decrease with sensor proximity to the bed, characteristic of theoretical boundary layers. The high frequency velocity variance, a measure of the localized turbulent energy, is determined with the variable-interval time average (VITA) technique, defined with [Blackwelder and Kaplan, 1976]

$$\hat{\text{var}}(z, t) = \frac{1}{T} \int_{t-T/2}^{t+T/2} u^2(z, s) ds - \left(\frac{1}{T} \int_{t-T/2}^{t+T/2} u(z, s) ds \right)^2 \quad (\text{IV-3})$$

where T is the window size (1/16 s for Figure IV.1), where u is the total velocity at each elevation, and t is the time of interest. This window size was selected because it is the time scale over which significant sediment response is observed with the FOBS. Following intuition, the intermittent concentration observations are coherent to the intermittent high frequency velocity variance structure. Visual inspections show that several of these events are paired with the larger wave events.

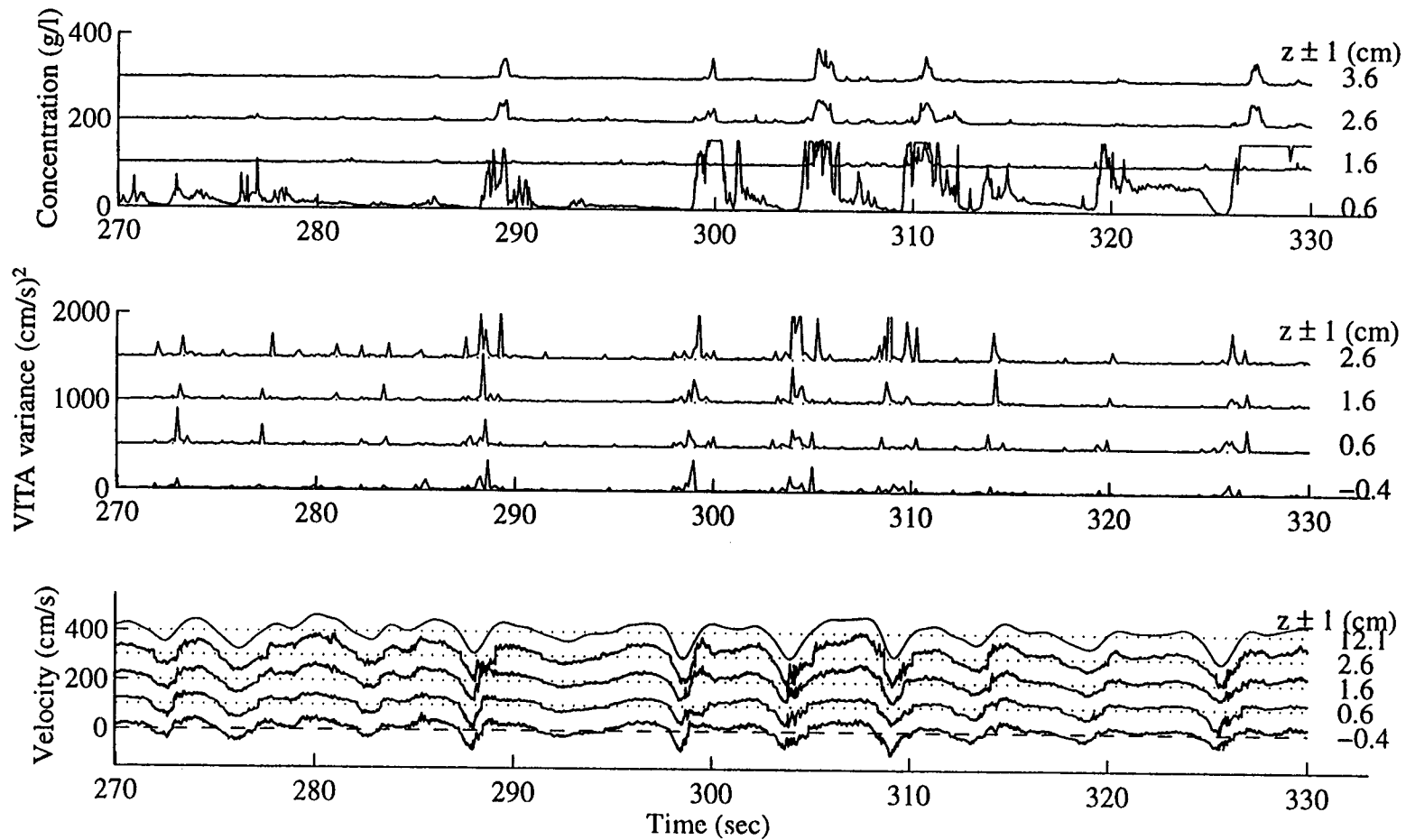


Figure IV-1. An example 60 second time series near bed cross shore velocity as measured by four hot film anemometers and the free stream velocity as measured by the EMCM (bottom panel); high frequency VITA velocity variance at four elevations above the bed (middle panel); and concentration at 4 elevations above the bed (top panel). The average distance of each sensor as from the bed as measured by the FOBS over the 60 second record is listed in the right hand column. Each velocity, variance, and concentration time series is offset by 100 cm/s, 500 (cm/s)², and 100 g/l, respectively. Onshore directed flow is defined with negative velocities and offshore directed flow is defined with positive velocities.

The frequency spectra of the four hot film sensors and the electromagnetic current meter (herein, EMCM), located in the free stream, during the first and third 256 s segments are coherent through the incident band and have decreasing variance with sensor increasing proximity to the bed (Figure III.13). A noticeable slope break occurs in the four hot film spectra at approximately 1 Hz which may indicate a change between dominance of wave and turbulent motions. This break becomes less obvious in the lowermost sensors which have a decrease in the incident band wave energy and may have a higher low frequency turbulence cutoff due to a smaller length scale.

The total velocity is partitioned into wave and turbulent motions with

$$u = U + u' \quad (IV-4)$$

where U is assumed to be the wave motions partitioned to frequencies less than 2 Hz and u' is assumed to be the turbulent motions partitioned to frequencies greater than 2 Hz.

Because it is not possible to identify a specific frequency or wavenumber break between wave and turbulent motions, we separate low frequency wave and current motions from turbulence motions at 2 Hz. This frequency cutoff will exclude the turbulent energy at the lowest turbulent frequencies; however, it will also decrease the likelihood of leaking wave motions to the following turbulence analysis. Because the wave motions have a significantly higher variance than turbulent motions, the turbulent motions lower than 2 Hz will have a negligible effect on the wave velocities. The wave and turbulent velocities are determined by defining wave motions to be the mean value over 1/2 sec windows at consecutive 1/16 s overlapping steps,

$$U(t_n) = \frac{1}{T_2} \sum_{n-T_2/2+1}^{n+T_2/2} u(t_n) \Delta t \quad (IV-5)$$

where T_2 is 1/2 s window. The remaining variance determined with (IV-4) is defined as turbulence.

IV-3. Results

The majority of turbulence investigations have been conducted in laboratories under sinusoidal waves. Consequently, it has been convenient to present the results as a function of wave phase (i.e. 0° to 360°). Because waves in the surf zone are random, this presentation technique is not possible. Figure IV.2 shows an alternative methodology, a phase plot of the free stream velocity versus acceleration from 290 to 305 seconds. In contrast to a sinusoidal wave, a wide range of velocities and accelerations are covered over this 15 second segment. In analogy to the wave phase, we propose a phase-space averaging (PSA) technique, which allows us to evaluate the magnitude and evolution of

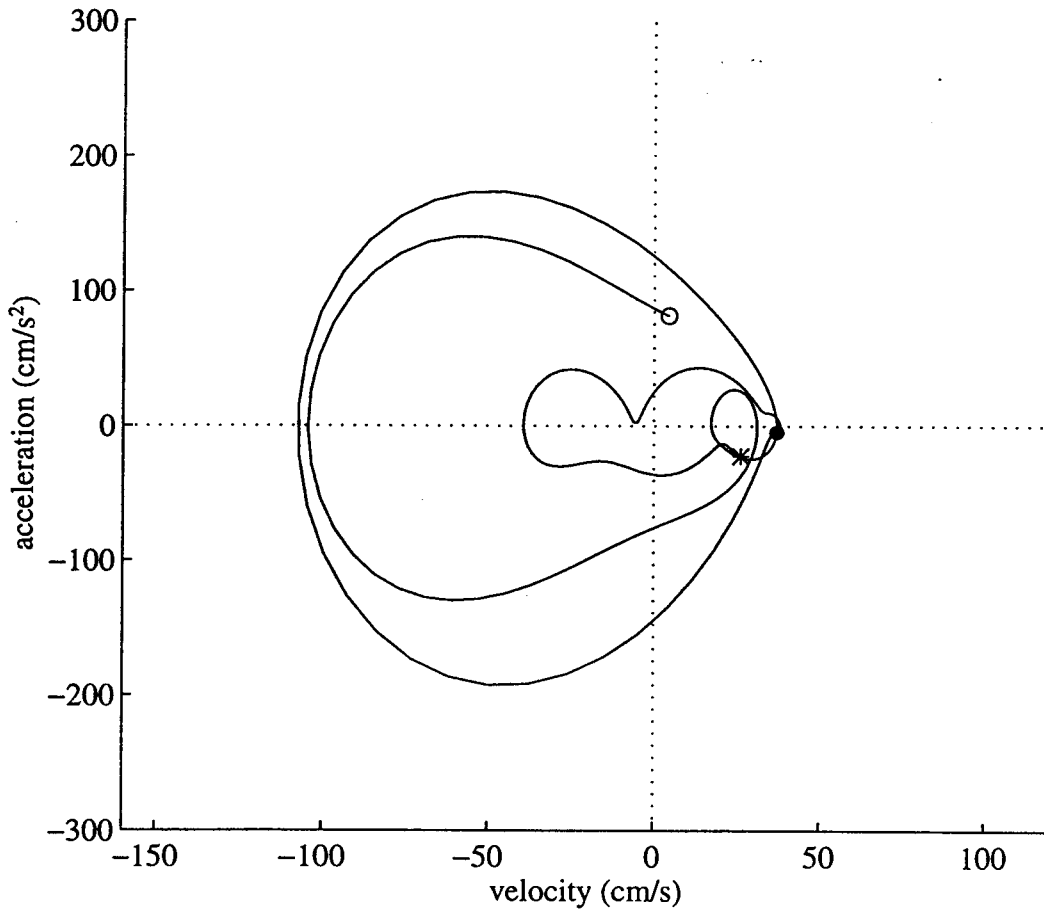


Figure IV.2. The phase space distribution of free stream velocity versus acceleration from 290 to 305 seconds. The particle velocities are moving in the clockwise direction. The symbols *, •, o denote the times 290, 300, and 305, respectively.

physical quantities, such as suspended sediment concentration, turbulent kinetic energy, and dissipation at like velocities and accelerations, and compare our results over the wave phase space. This is accomplished by binning each of the quantities (for each sensor and each data segment), at 1/16 s steps, over the free stream wave velocity (U_∞) and acceleration ($\partial U_\infty / \partial t$). The acceleration is determined in the frequency domain with a 1 Hz low pass cutoff frequency and is defined with

$$\frac{\partial U_\infty}{\partial t} = \frac{1}{2\pi} \int_{-f_{cut}}^{f_{cut}} i2\pi s \left\{ \int_{-\infty}^{\infty} U_\infty(\tau) e^{-i\tau s} d\tau \right\} e^{-is} ds, \quad (IV-6)$$

where $f_{cut} = 1$ Hz. The sample mean of the quantity in each bin is computed, producing a 'phase-space' average. For statistical stability, we require that at least three realizations be present in each observation, although this is generally not a problem. For all figures the seven velocity bins are centered on -140, -100, -60, -20, 20, 60, 100 cm/s with a ± 20 cm/s window about each bin. Similarly, the six acceleration bins are centered on -250, -150, -50, 50, 100, 150, 250 cm/s^2 with a ± 50 cm/s^2 window about each bin. The flow moves in a clockwise direction around the figure. Because the free stream velocity and acceleration are different for each of the 5 (sometimes 7) segments, not all phases will contain the same number of estimates. In describing the following results, we define acceleration as the derivative of the velocity (see (IV-6)), but the phrase 'accelerating flow' indicates flow which has an increasing velocity magnitude and similarly 'decelerating flow' indicates flow which has a decreasing velocity magnitude.

IV-3.1 Concentration

The PSA technique is performed on five concentration sensors with elevations ranging from 0 to 13 cm above the bed and over the five 256 s segments, resulting in 25 independent records, Figure IV.3. The extremely high PSA concentration near the bed are likely sensors which are fluctuating about the bed level. Curiously, the high fluid-sediment interface concentration levels (at the bed-water interface), primarily occur in all quadrants of the flow except during the onshore accelerating flow. Other than the near bed sensors, the suspension is largest following the wave crest during the positive accelerations as the flow transitions from onshore to offshore.

IV-3.2 Shear stress

In (IV-1) the transport of suspended sediment is assumed to be proportional to the shear stress, τ . Because it is not possible to solve for the Reynolds stress directly, it is commonly approximated with a zero equation turbulence closure eddy viscosity model

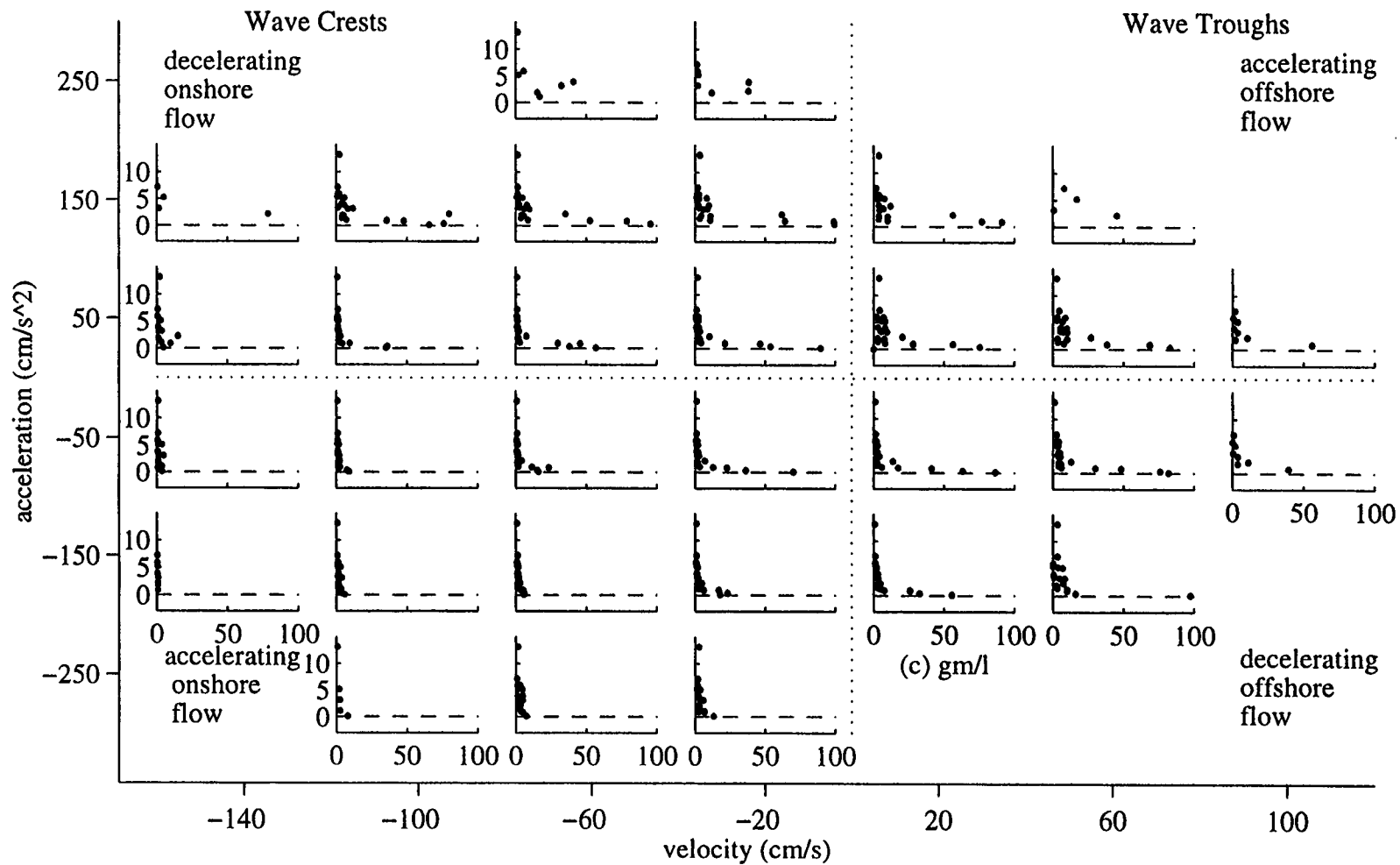


Figure IV-3. The phase space average distribution of concentration versus the sensor elevation of the five 256 second WBBL segments. The vertical axis of each independent plot is elevation from the bed, ranging from -2 to 15 cm, and the horizontal axis is concentration, ranging from 0 to 100 g/l. Each phase space average was required to have at least 3 realizations in each bin to be included.

$$\frac{\tau}{\rho} = -\langle u' w' \rangle \approx \nu_t \frac{\partial U}{\partial z}, \quad (\text{IV-7})$$

where τ is the stress, and ν_t is the eddy viscosity model. The velocity gradient, $\partial U/\partial z$ is approximated numerically as $\Delta U/\Delta z$ with the hot film array and by assuming the velocity at the bed to be zero.

The eddy viscosity is defined here with

$$\nu_t \equiv \kappa u_* z, \quad (\text{IV-8})$$

where κ is Von Karman's constant (≈ 0.41) and u_* is the bed shear velocity. The bed shear velocity is the characteristic velocity which parameterizes the velocity shear at the bed and is estimated here with (Smith, 1977)

$$u_* = \kappa z_o \left[\frac{\partial U}{\partial z} \right]_{z=z_o}. \quad (\text{IV-9})$$

Previous estimates of the bed shear velocity have been made by fitting logarithmic and exponentially decaying models to the rms velocity observations. Here, an estimate of the bed shear velocity is required at each instant in time. Because the above models are not appropriate during velocity zero crossings, the bed shear velocity is calculated by assuming that u_* may be represented with

$$\frac{\partial u(z_o, t)}{\partial z} \equiv \alpha u(z_o) + \beta u(z_o + z_1) + \gamma u(z_o + z_2), \quad (\text{IV-10})$$

where α , β , and γ are unknown constants and z_1 and z_2 are elevations of the two closest near bed velocity sensors. A Taylor series expansion is performed on each term in (IV-10) and truncated to 3 terms,

$$\frac{\Delta u(z_o, t)}{\Delta z} \equiv \alpha u(z_o) + \beta u(z_o) + \beta u_z(z_o) \frac{z_1}{1!} + \beta u_{zz}(z_o) \frac{z_1^2}{2!} + \gamma u(z_o) + \gamma u_z(z_o) \frac{z_2}{1!} + \gamma u_{zz}(z_o) \frac{z_2^2}{2!}. \quad (\text{IV-11})$$

Similar terms are collected and coefficients (α , β , and γ) are determined as

$$\alpha = \frac{-z_1^2 + z_2^2}{z_1 z_2 (z_1 - z_2)}, \quad \beta = \frac{-z_2}{z_1 (z_1 - z_2)}, \quad \text{and} \quad \gamma = \frac{z_1}{z_2 (z_1 - z_2)}. \quad (\text{IV-12})$$

(IV-12) is substituted into (IV-10). Furthermore, the velocity at the bed is assumed to be zero and (IV-10) and the bed shear estimate becomes

$$\frac{\partial u(z_o, t)}{\partial z} = -\frac{z_2}{z_1 (z_1 - z_2)} u(z_o + z_1) + \frac{z_1}{z_2 (z_1 - z_2)} u(z_o + z_2). \quad (\text{IV-13})$$

Once the bed shear velocity is estimated, the shear stress may be directly determined with (IV-7). Figure IV.4 shows the shear stress for the five segments of data at the four hot film elevations. At nearly all phases of the flow the shear increases linearly from the bed. The linear shear stress is indicative of uniform velocity shear through the water column ($\partial U/\partial z = \text{constant}$) and is in disagreement with laboratory and theoretical studies which predict that the shear decreases with increasing elevation from the bed. The largest shear stress is present under the crests and troughs of the waves although the stress is larger under the troughs than under the crests for the same velocity magnitudes (see ± 100 cm/s bin). This is likely attributed to the longer excursion time of the troughs, which allow the boundary layer to develop more fully than under the shorter duration crests. The estimated shear stress is relatively insensitive to free stream acceleration and is highly sensitive to the free stream velocity. The oscillatory nature of the estimated shear stress does not agree favorably with the PSA concentration structure which is biased towards the positive accelerations following the wave crests.

IV-3.3 Turbulent kinetic energy

Energy density frequency spectra were calculated by pre-whitening each 1/2 s window of velocity with a first difference filter and then post coloring in the frequency domain by removing the effect of the high pass time domain filter. This method proved to be the most robust method for eliminating the leakage of the dominant low frequency signal. Example PSA spectra for a single 256 s velocity record at 4 cm above the bed is shown in Figure IV.5. A line was fit to the observations with a weighted ($\log(f)$) least squares analysis, over the frequency range of 2 to 100 Hz, at each phase. Because it is not possible to show all the PSA spectra distributions from each sensor and each run, we approximate all spectra with its turbulent slope and integrated variance.

The PSA distribution of the turbulent frequency slopes is shown in Figure IV.6. The free stream slopes are in agreement with the slopes in the upper part of the wave bottom boundary layer. There exists a trend in the slopes from flatter than $-5/3$ to steeper than $-5/3$ as velocity magnitudes decrease from peak values to zero. This trend can also be seen in Figure IV.5 for a single 256 second run. The flatter slopes present under the peak velocities would suggest the energy is being dissipated more rapidly than it is being generated. Figure IV.5 suggests that the flatter slopes present at the peak velocities are a result of a decrease in energy at the low frequencies. Although this may explain how the resulting slopes are flatter, the explanation as to why remains unclear. Steeper slopes are present during the velocity zero crossings. Because the universal equilibrium theory of turbulence predicts $-5/3$ slopes of wavenumber spectra and not wave frequency spectra, this

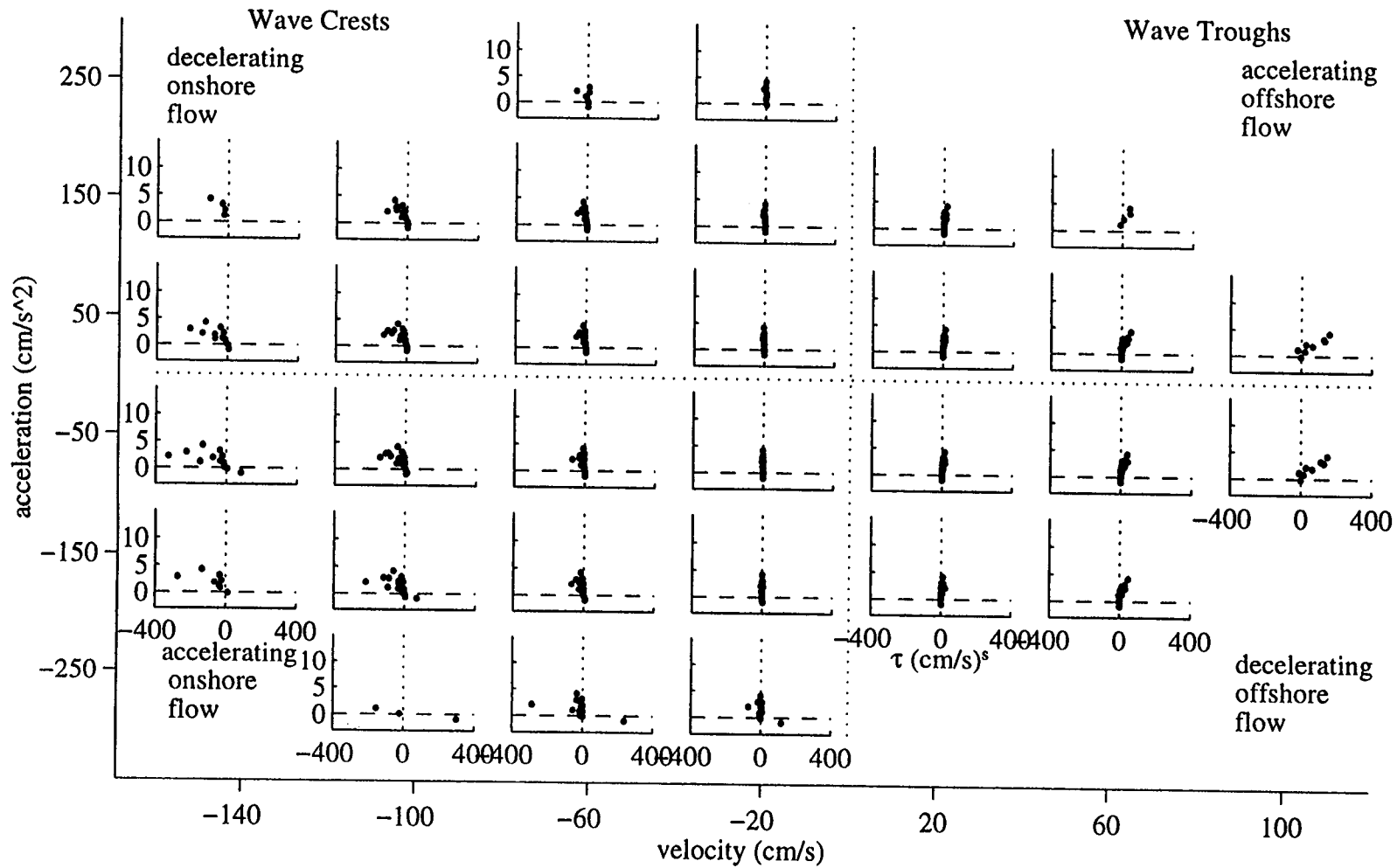


Figure IV-4. The phase space average distribution of shear stress versus the sensor elevation of the five 256 second WBBL segments. The vertical axis of each independent plot is elevation from the bed, ranging from -2 to 15 cm, and the horizontal axis is stress, ranging from -400 to 400 (cm/s)².

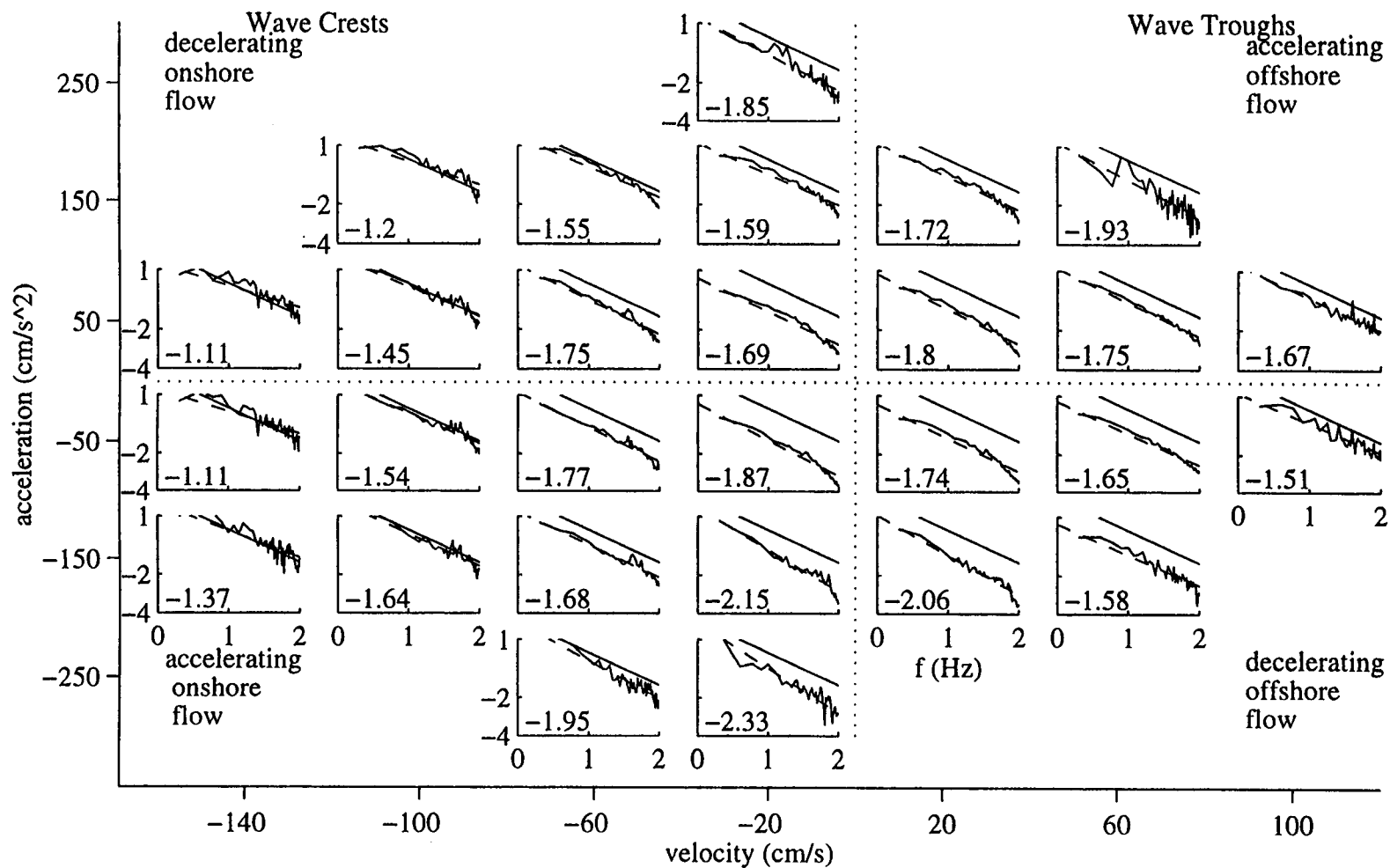


Figure IV-5. The phase space average distribution of velocity energy density spectrum at 4 cm above the bed versus frequency during one 256 second record. The vertical axis of each independent plot is energy density $((\text{cm/s})^2/\text{Hz})$ and the horizontal axis is frequency, ranging 1 to 100 Hz. The spectra were calculated over 1/2 second windows of data with a 1/16 sec overlap. The slope of each spectrum is given in the lower right hand corner of each plot.

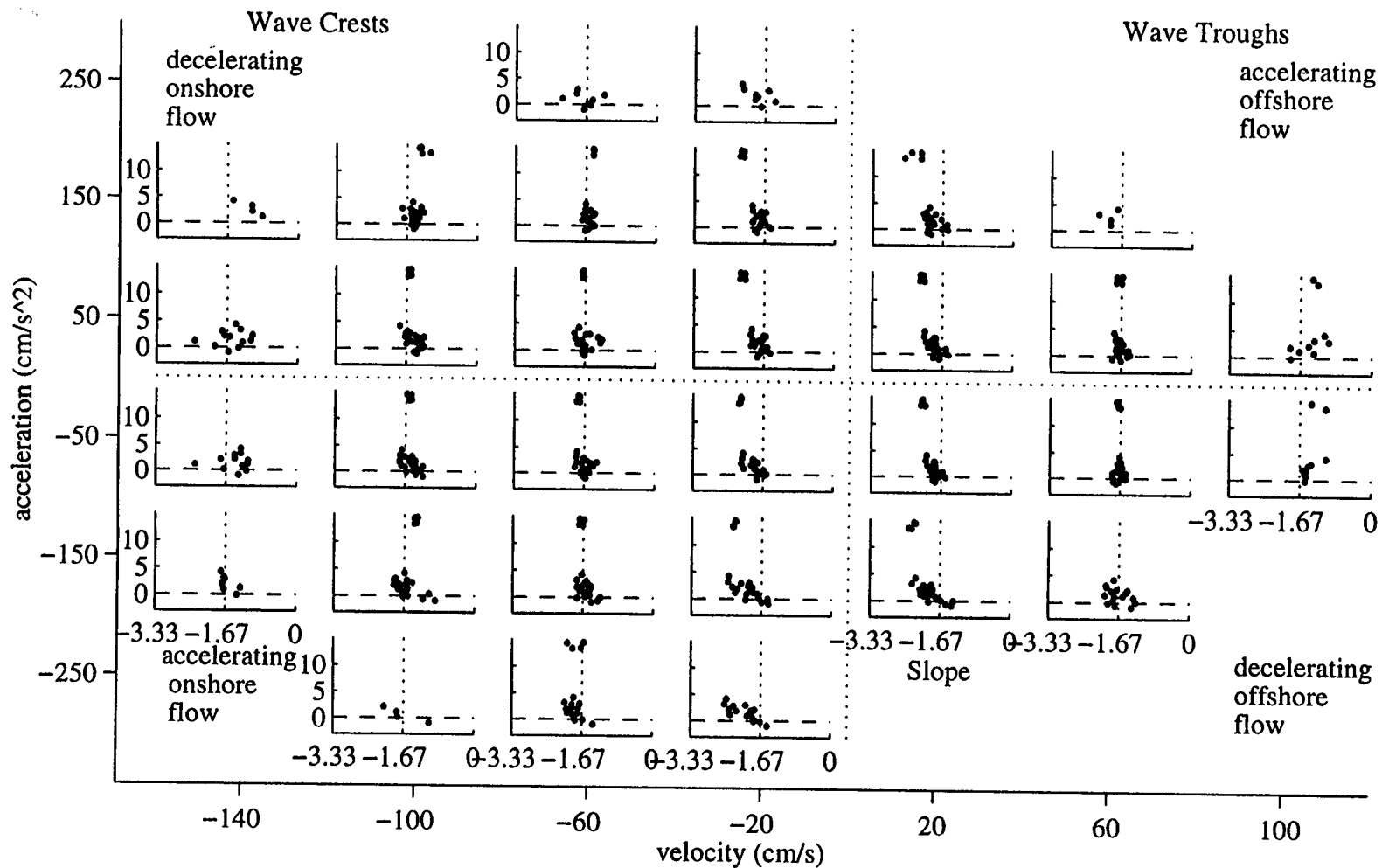


Figure IV-6. The phase space average distribution of frequency slopes versus the sensor elevation of the five 256 second WBL segments. The vertical axis of each independent plot is elevation from the bed, ranging from -2 to 15 cm, and the horizontal axis is slope, ranging from -10/3 to 0.

last observation is likely an effect of the advective velocity (U) not being large enough for the transformation to wavenumber space. The criteria needed to transform from frequency to wavenumber space is discussed in the next section. When significantly steeper slopes are present in the free stream and upper WBBL spectra, the slopes approach $-5/3$ at sensors closest to the bed and may be attributed to a decrease of local acceleration in the lowermost sensors.

The turbulent kinetic energy (TKE) ($\overline{u'u'}$) is defined as the integral of the energy frequency spectra ($\Phi(f)$) from 2 to 100 Hz. As before noted, we recognize that turbulent motions which have frequencies lower than 2 Hz will be excluded and consequently the values reported here are expected to be lower than the true magnitudes, Figure IV.7. Under mild wave conditions ($u_{\infty} < 80$ cm/s and $|\partial u_{\infty} / \partial t| < 200$ cm/s²), the turbulent kinetic energy increases linearly with elevation from the bed, and energy magnitudes in the free stream are generally lower than those in the upper elevations within the WBBL. This situation is characteristic of the bottom shear generated turbulence which scales with elevation away from the bed. Turbulence levels begin to increase following the transition from offshore to onshore flow. Under the crests peak, turbulence levels are significantly larger and more vertically uniform, than in most other wave phases.

The distribution of the turbulent kinetic energy is largest under the wave crest and decreases over the decelerating flow until reversal to offshore flow. In agreement with Hino et al. [1983] and Sleath [Sleath, 1987], the turbulent kinetic energy has significantly decreased by the time of flow reversal. These observations show that the enhanced turbulent kinetic energy levels are achieved during the latter stages of the onshore accelerating flow. Hino et al. and Sleath also observed an increasing horizontal turbulent intensity at the latter stages of the accelerating flow, and Hino et al. concluded that the turbulence was suppressed until the flow begins its decelerating phase. These observations show only mildly enhanced turbulent kinetic energy levels under the troughs for comparable velocity magnitudes to those under the crests. The lower energy levels may be indicative of a sensitivity of turbulence generation to acceleration magnitudes as well as velocity magnitudes. Unfortunately, the purely sinusoidal laboratory wave velocities leave us without comparison in attempting to explain the discrepancies between the wave crest and troughs.

IV-3.4 Dissipation Rate

Dissipation was calculated by following the technique of George, et al. [George et al., 1994]. In homogeneous isotropic turbulence, the universal form of the velocity spectra over the inertial subrange is defined with (IV-2):

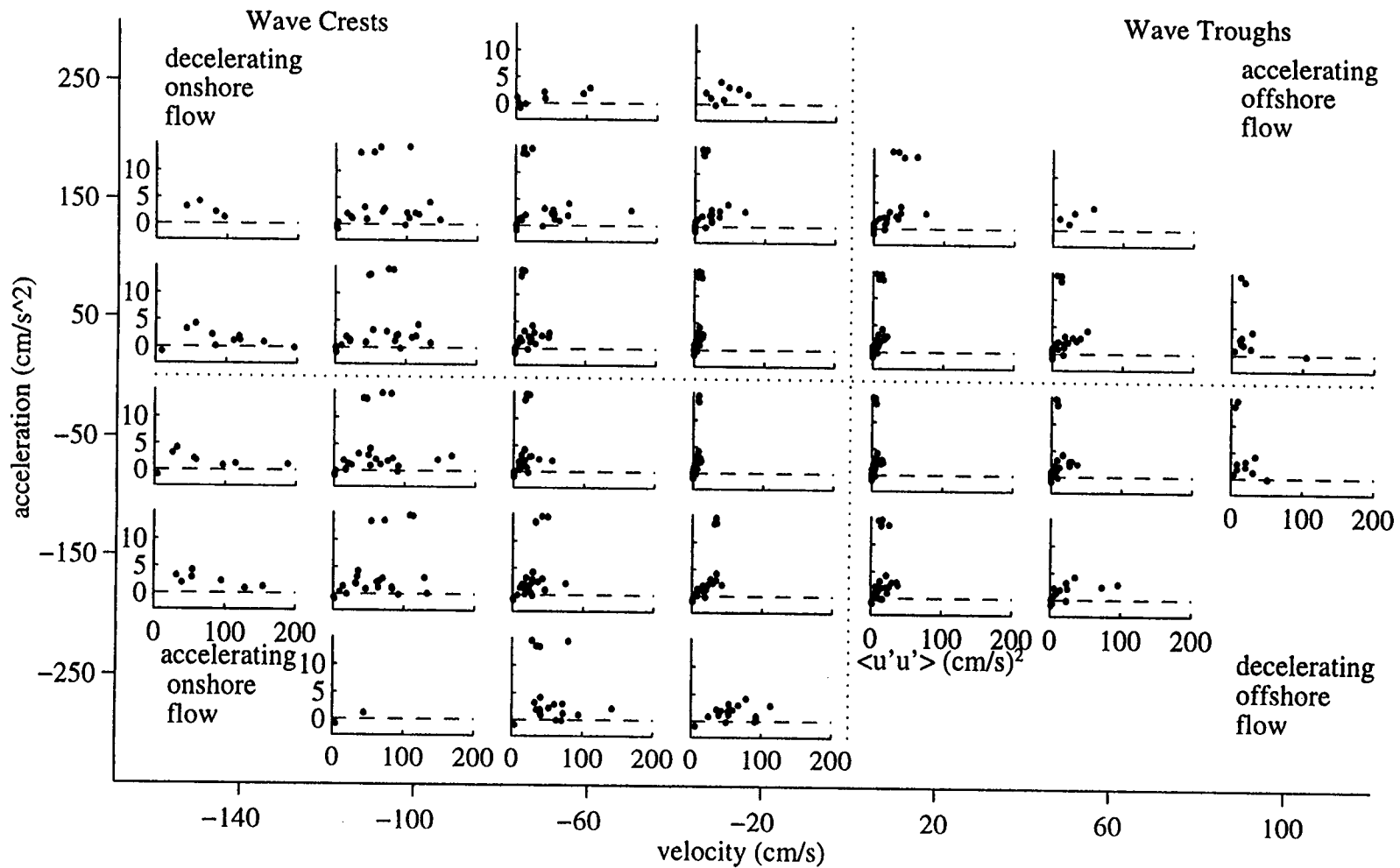


Figure IV-7. The phase space average distribution of turbulent kinetic energy versus the sensor elevation of the five 256 second WBL segments. The vertical axis of each independent plot is elevation from the bed, ranging from -2 to 15 cm, and the horizontal axis is stress, ranging from 0 to 200 (cm/s)².

$$\Phi(k) = \alpha \varepsilon^{2/3} k^{-5/3}$$

where α is a nominal constant (~ 0.5), ε is the energy dissipation, and k is the wavenumber [Tennekes and Lumley, 1972]. Commonly, the transformation of frequency spectra to wavenumber spectra is performed by using Taylor's hypothesis by assuming that the turbulence is advected past the sensor by the mean velocity (or lowest wavenumber) with

$$\Phi(k) = \frac{\Phi(f)}{2\pi/U}, \quad (\text{IV-14})$$

with

$$k = \frac{2\pi f}{U}. \quad (\text{IV-15})$$

In order for this transformation to be valid, two criteria must be met. First, the mean advection velocity must be greater than the turbulent velocity to satisfy Taylor's frozen flow hypothesis.

$$U \gg u'. \quad (\text{IV-16})$$

Secondly, George et al., modified Lin's criteria to further specify that the mean velocity (over a small window of time) must be greater than the change in velocity over the window of calculation with

$$U \gg \frac{1}{f_{lo}} \frac{\partial U}{\partial t}, \quad (\text{IV-17})$$

where f_{lo} is the lowest frequency over which the spectral calculations were determined. To satisfy this last criteria it was necessary to convert to wavenumber space only over frequencies greater 8 Hz. A 8 Hz low frequency cutoff translates to a 9° phase variation over a 5 sec wave. Furthermore, we only transform frequencies out to 100 Hz to avoid spectral roll off due to dissipation.

Following the transformation to wavenumber space, the dissipation rate is found with (IV-2) by fitting a $k^{-5/3}$ line to $\Phi(k)$, Figure IV.8. Any values for which the r^2 correlation was not significant were excluded from further analysis. Figure IV.8 shows the PSA of the dissipation estimates which passed the criteria of (IV-16) and (IV-17). Because of occasional spikes in the dissipation rate estimates, a three standard deviation filter was applied to the estimates before computing the phase space averages.

Unlike the turbulent kinetic energy distribution, the dissipation is only slightly enhanced under the wave crests. Only during the extreme wave crests can the dissipation be shown to decrease linearly with increasing sensor elevation, as is predicted in shear flow

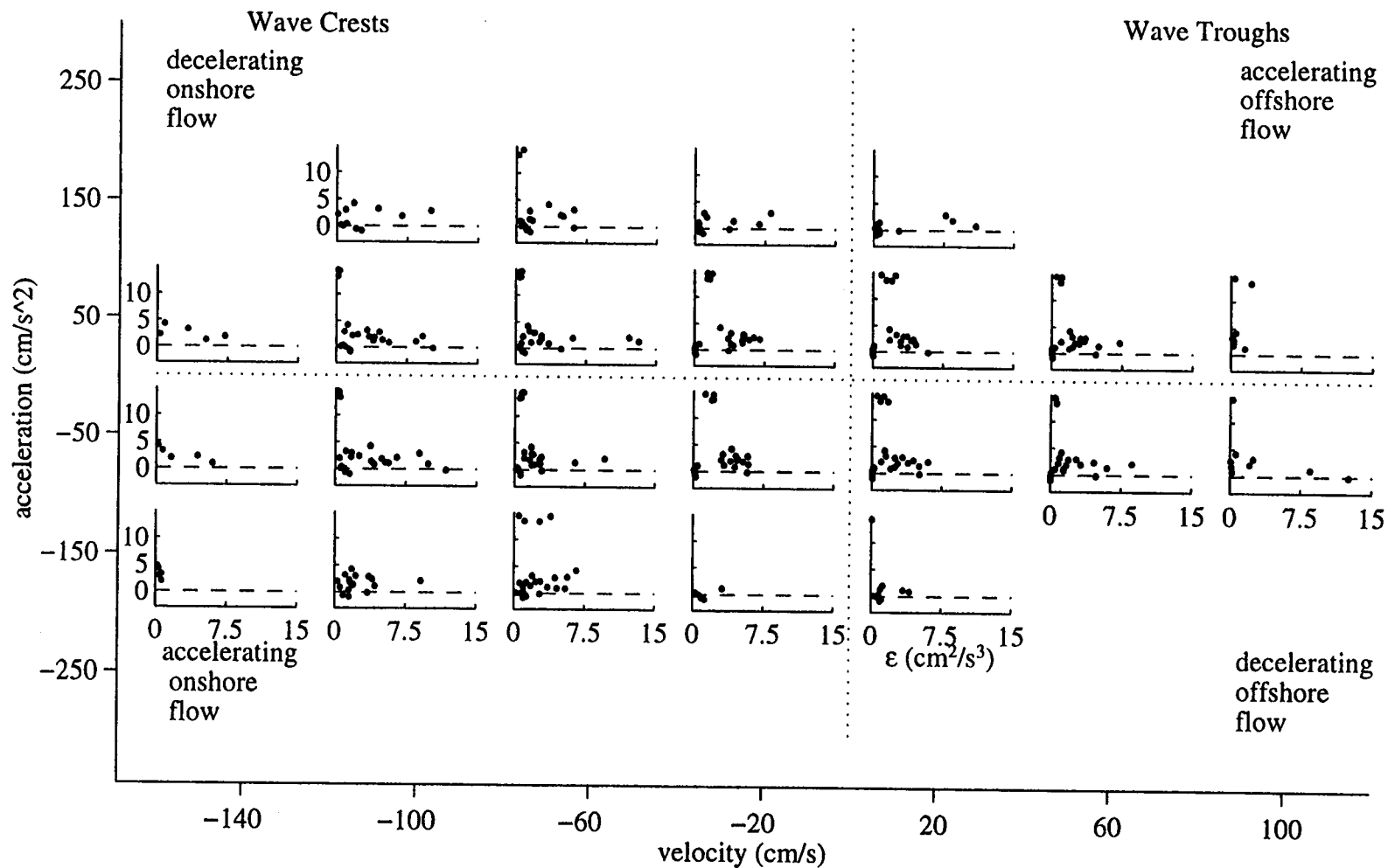


Figure IV-8. The phase space average distribution of energy dissipation rate versus the sensor elevation of the five 256 second WBL segments. The vertical axis of each independent plot is elevation from the bed, ranging from -2 to 15 cm, and the horizontal axis is stress, ranging from -0 to 15 (cm^2/s^3).

[*Tennekes and Lumley, 1972*]. Dissipation rates in the wave bottom boundary layer are shown on average to be a factor of 2 (and occasionally as much as an order of magnitude) higher than those found in the free stream flow. Significantly larger dissipation rates of $300 \text{ cm}^2/\text{s}^3$, assuming a 2 m water depth, from the surf zone wave breaking region have been observed [*George et al., 1994*]. On the continental shelf, dissipation rates in the current boundary layer which were under the influence of waves ranged from 0.001 to $0.1 \text{ cm}^2/\text{s}^3$ [*Gross et al., 1994*]. And in the ocean surface boundary layer, Anis and Moum [1995] observed dissipation rates of 0.01 to $0.1 \text{ cm}^2/\text{s}^3$. Given the large shears in the WBBL, it is not surprising that dissipation rates are significantly larger than in the current or ocean boundary layer.

IV-5. Conclusions

Using the first available turbulence observations of the wave bottom boundary layer it was found that the generation of turbulence is highly intermittent. It was possible to examine the intermittent nature of flow by applying homogenous isotropic turbulence laws over small windows of data. The time varying estimates of turbulent kinetic energy, shear stress, dissipation, and concentration were averaged over the phase space of the free stream wave.

The periods of enhanced turbulence most often occur under large wave crests. These observations show that the distribution of the turbulent kinetic energy is largest under the wave crest, and decreases over the decelerating flow phase until flow reversal to offshore flow. Enhanced turbulent kinetic energy levels are observed during the latter stages of the onshore accelerating flow. Only mildly enhanced turbulent kinetic energy levels under the troughs are observed for comparable velocity magnitudes to the those under the crests. The lower energy levels may be indicative of a sensitivity of turbulence generation to acceleration magnitudes (which are lower under the trough than under the crest) as well as velocity magnitudes. The turbulent kinetic energy observations under the crests compare favorably to those of the three laboratory studies. Unfortunately the purely sinusoidal laboratory wave velocities leave us without comparison in attempting to explain the discrepancies between the wave crest and troughs.

The shear stress was estimated with an eddy viscosity model and shown to be highly sensitive to free stream velocity and less sensitive to free stream acceleration. The peak shears occur under both the crests and troughs of the wave. For equal free stream velocity magnitudes, the stress under the troughs exceeds the stress under the crests, and is likely attributed to the longer excursion time of the troughs, which allow the boundary layer to develop more than under the shorter duration crests.

The sediment suspension observations were shown to have an intermittent structure and to be biased towards the onshore decelerating phase of the flow. This signature was shown to be coherent with and lag the turbulent kinetic energy observations. However, the concentration observations are not in agreement with the oscillatory nature of the shear stress estimates.

Dissipation rates were found to be several orders of magnitude lower than those found in the active surface breaking region of the surf zone, but orders of magnitude higher than those found in the ocean boundary layer and continental shelf current bottom boundary layer.

CHAPTER V: SEDIMENT SUSPENSION EVENTS AND SHEAR INSTABILITIES IN THE BOTTOM BOUNDARY LAYER

Abstract

The intermittent, rapid suspension of sediment in the surf zone is not well understood. Because the boundary layer is the region of fluid in direct contact with the sea bed, we believe that it plays an important role in the sediment suspension process. In this paper we examine the flow characteristics during the initiation of suspension events using field data from a recent Oregon coast experiment, and propose a hypothesis for the generation of events through a shear instability of a oscillatory bottom boundary layer.

Theoretical predictions suggest that flow in the bottom boundary layer leads that of the free stream, resulting in an inflection point (a necessary condition for a shear instability) in the vertical profile of cross-shore velocity during flow deceleration and reversal. It is during this phase of the flow that small perturbations may grow exponentially to breaking, leading to increased levels of turbulence. Bottom boundary layer shear instabilities, leading to large near bed velocity fluctuations, may be responsible for the rapidly suspended sediment. A simple linear instability analysis predicts if and when small perturbations will become unstable.

The 1993 San Marine field experiment on the Oregon coast investigated suspended sediment concentrations and high frequency near-bed fluid motions. Up to four hot film anemometers, sampled at 2000 Hz for 34 min., were located between 1 and 4 above the bed. Variance was roughly partitioned between high frequency motions (which includes turbulence) and wave motions by examining the time variation of variance within 1/8 second blocks of data. Sixty-five percent of the suspension events are correlated to variance events with an average lag of 0.75 sec. Both the suspension events and variance events are shown to occur during the offshore decelerating and onshore accelerating flow phases.

V.1 Introduction

In the surf zone, the process of sediment suspension is punctuated with rapid appearances and disappearances of high sediment concentration of sediment at elevations above typical wave boundary layers $O(5\sim 10\text{cm})$. These rapid and intermittent events cannot easily be explained or modeled as a turbulent diffusive process. Understanding

fluid-sediment interactions leading to the sediment suspension process is essential to the development of large scale sediment transport models.

While these sediment suspension events have been readily observed by numerous investigators [*Jaffe et al.*, 1984; *Huntley and Hanes*, 1987; *Beach and Sternberg*, 1988], the fluid forcing responsible for them has not. The rapid appearance and disappearance of sediment at high levels above the bed may be due to simple horizontal advection of a sediment cloud back and forth past a sensor array. However, this does not explain how the material reaches such an elevated position. In the absence of turbulence generated by bedforms or injected from the surficial wave breaking, the explanation for this phenomenon has remained relatively elusive.

The rapid appearance of suspension events may be related to a rapid generation or introduction of near-bed turbulence. Previous research has focused on the introduction of turbulence to the bottom boundary layer through wave breaking at the surface or the generation of turbulence at the bed due to bedforms. Alternatively, we explore the generation of turbulence from within the boundary layer through the breaking of a shear instability wave.

The purpose of this investigation is to characterize the fluid motions associated with individual suspension events using high frequency response, hot film anemometers paired with optical back scatter sensors. These measurements help to evaluate boundary layer shear instability as a mechanism for the rapid generation of turbulence within the bottom boundary layer which, in turn, leads to sediment suspension. The first part of the paper introduces the shear instability theory and requisite boundary conditions and background profile structure. In the second part of the paper, field data from an Oregon coast beach is presented and the viability of the shear instability mechanism for generating suspension events is evaluated.

V.2 Theory

The bottom boundary layer plays an important role in the sediment suspension process, as it is the region of fluid in contact with the bed. In traditional boundary layer theory, the excess pressure above hydrostatic inside the boundary layer is assumed constant in depth. The no slip condition at the bed, causes the fluid close to the bed to have smaller inertia and consequently, responds to free stream cross-shore pressure gradients prior to both the fluid in the upper part of the boundary layer and in the free stream layer. Thus, the boundary layer leads the free stream flow, resulting in an inflection point in the bottom boundary layer profile during flow deceleration, reversal, and subsequent

acceleration [Smith, 1977]. A sketch of a typical velocity profile within a monochromatic wave boundary layer at several wave phases is shown in Figure V.1.

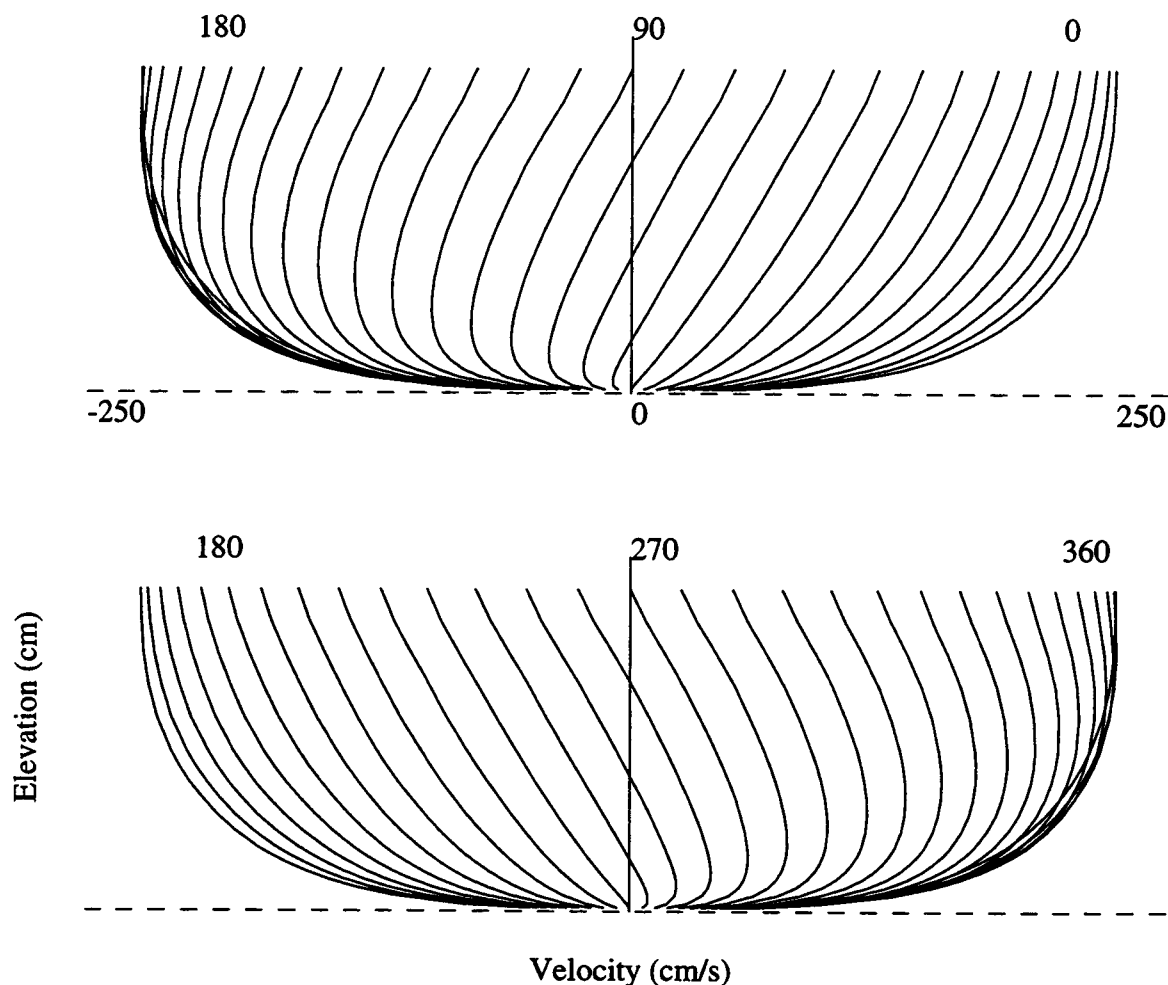


Figure V.1. Oscillatory velocities as a function of height above the bed for phase angles from 0° to 360° . Fluid response in the boundary layer leads that of the free stream velocity.

Raleigh [1880] determined that the necessary condition for an instability of inviscid parallel shear flow is that the profile contain maximum vorticity (an inflection point) within the flow region. If a velocity profile contains a large vertical shear and an inflection point, small perturbations may become unstable and grow exponentially in time. If the growth rate of the unstable wave is of large magnitude, the wave will break and generate turbulence.

A linear instability is investigated as a possible mechanism for generating large near bed velocity fluctuations leading to a rapid vertical redistribution of sediment.

This derivation will closely follow that of Bowen and Holman [1989] for instabilities of a mean alongshore current with a cross-shore variation. This analysis will examine instabilities of the bottom boundary layer cross-shore velocity with a vertical variation.

The cross-shore, u' , and vertical, w' , velocities are decomposed into mean, U and W , and perturbation components, u and w ,

$$\begin{aligned} u'(x, z, t) &= U(z) + u(x, z, t) \\ w'(x, z, t) &= w(x, z, t) \end{aligned} \quad (\text{V-1})$$

where U is the background cross-shore velocity and assumed fixed in x and t . The mean vertical velocity, W , is defined to be zero; and u and w are the cross-shore and vertical perturbation velocities, respectively. x and z are the cross-shore and vertical coordinates (x is positive offshore and z is positive upwards).

The cross-shore and vertical linear inviscid 2-d equations of motion are

$$\begin{aligned} u_t + Uu_x + wU_z &= -\frac{1}{\rho} P_x \\ w_t + Uw_x &= -\frac{1}{\rho} P_z - g \end{aligned} \quad (\text{V-2})$$

where P is the pressure; g is gravitational constant; ρ is fluid density, and the subscripts denote partial derivatives. Alongshore homogeneity is assumed. The 2-d conservation of mass equation is

$$u_x + w_z = 0. \quad (\text{V-3})$$

By cross differentiating and combining with (V-2) P is eliminated, resulting in

$$\left(\frac{\partial}{\partial t} + U \frac{\partial}{\partial x} \right) (\nabla^2 \Psi) = U_{zz} \Psi_x \quad (\text{V-4})$$

where the stream function, Ψ , is defined in terms of u as,

$$\begin{aligned} u &\equiv -\Psi_z \\ w &\equiv \Psi_x. \end{aligned} \quad (\text{V-5})$$

The perturbation solution is assumed to be

$$\Psi = \Re e \left\{ \psi(z) e^{i(kx - \sigma t)} \right\}, \quad (\text{V-6})$$

where k and σ are defined as the cross-shore perturbation wave number and cross-shore perturbation frequency. k is assumed real, and σ and ψ are assumed complex, $\sigma = \sigma_r + i\sigma_i$ and $\psi = \psi_r + i\psi_i$. After expanding (V-4) becomes

$$\left(-\frac{\sigma}{k} + U\right)(\psi_{zz} - k^2\psi) = U_{zz}\psi \quad (7)$$

Ψ will grow exponentially in time when σ_i is greater than zero.

V.3 Model Formulation

A simple one dimensional, time-dependent, turbulent diffusion model is employed to approximate the velocity structure within the bottom boundary layer (BBL) [Smith, 1977; Beach and Sternberg, 1992]. In calculating the boundary layer velocity profiles, the cross-shore velocity time series (at $z=14$ cm) is decomposed into a series of onshore/offshore half wave segments. Each half wave segment is identified with the half-period defined as the time between zero crossings, and the amplitude defined as the maximum velocity of the free stream profile filtered to 0.5 Hz. Use the amplitude and period to iteratively approximate the bed shear velocity ($u_o = u_{*max} \ln(\delta/z_o)$), and boundary layer thickness ($\delta = u_{*max}/(2\omega)$). The bottom roughness, z_o is held constant at 0.0766. The eddy viscosity, for each half wave segment, increases linearly away from the bed with an exponential decay above the wave boundary layer [Beach and Sternberg, 1992]. The model yields the vertical velocity structure of the cross-shore velocity through the BBL to the free stream for each time within the segment interval. Subsequent profiles from the next half wave period are merged to form a continuous time series over the 34 minute run.

Because the boundary layer model approximates each half wave as a sinusoid, important asymmetries in natural wave accelerations (always larger during the transition to onshore flow) are neglected.

Based on predictions by the boundary layer model, the velocity profile contains an inflection point for up to approximately $T/4$, where T is the wave period, Figure V.1. As a simple illustration, assume the cross-shore velocity profile is fixed for the entire $T/4$ secs (which it is not). For a perturbation amplitude to grow to be 100 times its original amplitude, the growth rate, σ_i , would have to be $18.4/T$ or greater. For a 10 sec wave, the growth rate would be 1.84 Hz.

Using a steady-background instability model on oscillatory background flow problem requires that the perturbation time and cross-shore length scales be much smaller than the mean (in this case oscillatory) flow scales. Neglecting time-dependent background flow terms in the instability model, assumes that the oscillatory cross-shore vertical profile

is fixed at each time instant, requiring that the instability grow much faster than the boundary layer changes. The linear instability analysis is performed on each modeled velocity profile at each 1/8 sec time step. The primary goal of this analysis is to determine whether the model will predict instabilities with rapid growth rates over the wavelength range of 2 cm to 50 cm. This wavelength range was selected because we expect instability length scales to be of order boundary layer thickness.

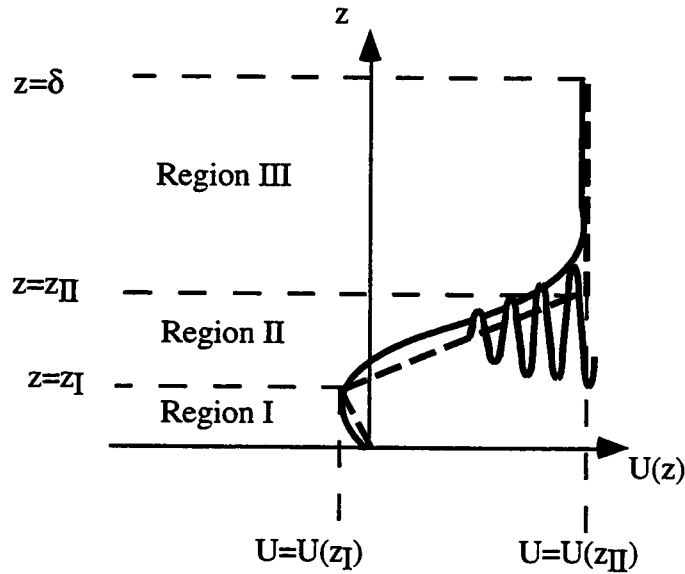


Figure V.2. Boundary layer geometry showing the three regions of the linear analysis.

To model the shear instability, the modeled boundary layer velocity profile is approximated with three linear regions, Figure V.2. Region I is defined at the lower limit by $U(0)=0$ and at the upper limit by searching upwards for a local extremum, $U(z_I)$ at z_I . The slope of the line in region II is defined as the maximum vorticity (maximum vertical shear), by searching upwards from z_I and the upper limit determined by projecting the line up to the free stream velocity, $U(z_{II})$. The velocity in region III is defined as constant, $U(z_{II})$ and bounded at the boundary layer thickness, δ . In each linear region, (V-7) reduces to

$$\psi_{zz} - k^2 \psi = 0. \quad (\text{V-8})$$

The solution for each region is

$$\begin{aligned}
 \text{Region I:} & \quad \psi_I = A_1 \sinh(kz) \\
 \text{Region II:} & \quad \psi_{II} = A_2 \sinh(kz) + B_2 \cosh(kz) \\
 \text{Region III:} & \quad \psi_{III} = A_3 e^{-kz}
 \end{aligned}$$

where A_1 , A_2 , A_3 , and B_2 are integration constants and determined with the boundary conditions. The perturbation frequency, σ , may be solved in terms of the perturbation wavenumber, k .

V.4 Field study

V-4.1 Location

A field study was conducted in the inner surf zone of a dissipative beach on the central Oregon coast during September 21-28, 1993. The San Marine beach runs north-south and is exposed to North Pacific storm and swell conditions. The September 26, 1993 offshore significant wave height and dominant period were 1.5 m and 7 sec, as recorded by wave buoy at Newport (38 km north of San Marine). The average beach slope was 1/50. Previous studies have found the sediment to be very well sorted with a mean grain size of 0.23 mm (Beach and Sternberg, 1988). The sea bed was smooth and without ripples or scour holes.

Instrumentation

Instrumentation consisted of 1 Marsh-McBirney electromagnetic current meter, 1 strain gauge-type pressure transducer, 3 ducted impeller current meters (SM), 3 optical back scatter sensors (OBS), up to 4 hot film anemometers, 1 underwater laser, and 1 underwater video camera. The hot films were sampled at 2000 Hz and all other instruments were sampled at 8 Hz.

The instruments were mounted to a cross bar supported by two pipes jettied in the alongshore with a 6 m separation (Fig. 3). Instrument orientation and maintenance was performed at low tide and data were recorded for approximately 2 hours during high tide. Data from 26 Sept 1993, when two hot films were deployed at 1 and 2 cm from the bed, will be discussed below. Three pairs of OBS (C1, C2, & C3) and current meter (SM1, SM2, & SM3) were located at $z=4, 9$, and 14 cm, respectively. The electromagnetic current meter (EM1) was 14 cm off the bed.

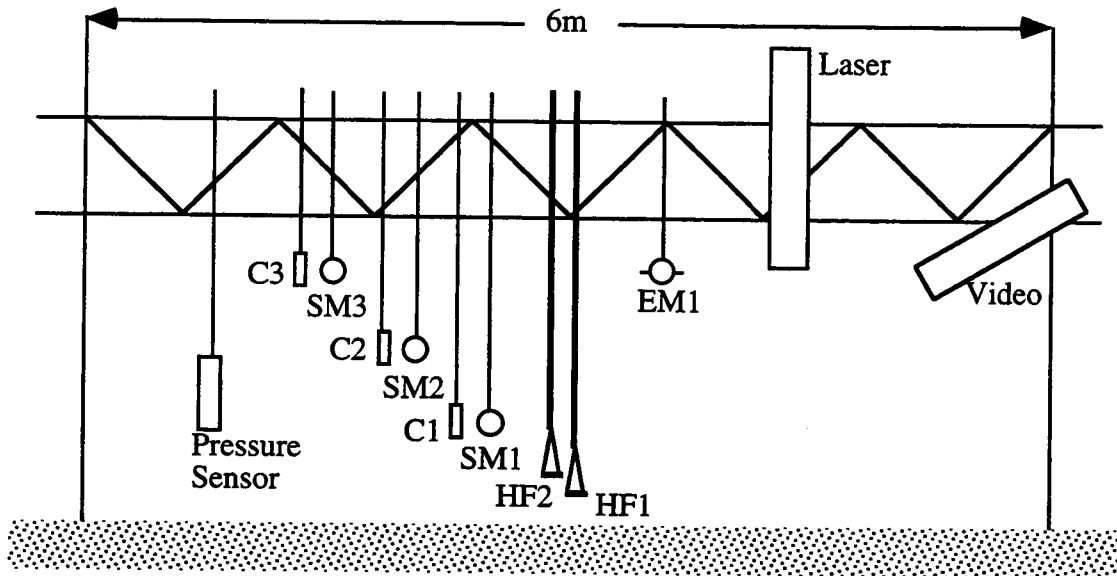


Figure V.3. Sketch of instrumentation deployment on 26 Sept 93, shows the configuration of 3 OBS concentration sensors(C1, C2, & C3), 3 ducted impeller current meters (SM1, SM2, & SM3), 2 Hot Film Anemometers (HF1 & HF 2), 1 electromagnetic current meter(EM1),.

V-4.2 Hot Film Calibration

The hot film anemometers were calibrated to the electromagnetic current meter in situ [George *et al.*, 1994]. Each hot film probe was calibrated for 10 minutes at $z=14$ cm, then lowered to the desired elevation. The output of each hot film sensor, HF1 and HF2, was block averaged to 8 Hz and plotted versus the rectified current meter data, EM1, ($z=14$ cm). A best fit exponential curve was fit to the paired data and used as the transfer function from output (volts) to speed (cm/s). This technique only calibrates the magnitude of the velocity(speed), as the hot films are rectified and direction is unknown. Maximum observed velocities occasionally exceeded the range of hot films (± 187 cm/s, HF1, and ± 287 cm/s, HF2).

V.5 Results and Discussion

A five minute time series of the SM1 and EM1 velocities and the C1 and C2 suspended sediment concentration is shown in Figures V.4a, 4f, and 4g, respectively. HF1 and HF2 are block-averaged to 8 Hz and are shown in Figure V.4c. For visual comparison to Figure V.4c, SM1 is rectified and shown in Figure V.4b. Offshore directed flow is positive.

Each 2000 Hz hot film time series is variance-partitioned into an 8 Hz variance time series by merging the variance of subsequent 1/8 sec intervals. The variance time series characterizes the levels of high frequency velocity fluctuations within each 1/8 sec interval, over time (Figures V-4d and V-4e). A sensitivity analysis determined that partitioning the variance over larger time intervals affected only the magnitude of variance and not the occurrence of a variance event. This investigation is only concerned with the initiation of turbulence events.

An event based analysis defined suspension events to have concentration greater than 10 gm/l at $z=4$ cm and variance events to have velocity variance exceeding $300 \text{ cm}^2/\text{sec}^2$ at $z = 2$ cm. The 8 Hz time series of velocity variance is similar to the suspended sediment time series as both contain rapid intermittent events. Sixty-five percent of the suspension events are correlated with variance events and lag the variance events by 0.75 secs.

An expanded view of the time series from Figure V.4 is shown in Figure V.5. The concentration event at 8.5 minutes follows a backwash of long duration and occurs near the period of rapid flow reversal. During this period of flow deceleration, reversal, and subsequent acceleration, the velocity sensors at $z=1, 2,$ and 4 (HF1, HF2, and SM1) reverse direction prior to the velocity at sensor $z=14$ (EM1), and are of large magnitude. This large magnitude signal, at the sensors 4 cm and lower, precludes the variance and suspension events. Bottom boundary layer theory predicts the phase lead, however does not predict the large onshore accelerations which follow. The long backwash and rapid flow reversal are the background velocity conditions which could lead to a shear instability. The large velocity magnitude of the lower sensors could have been a result of exponential growth of a small perturbation, a shear instability.

To characterize the background cross-shore flow associated with events, the velocity versus acceleration at the initiation of suspension events are plotted in Figure V.6a. The initiation of the sediment and variance events is determined by manually searching back in time from the event, as specified earlier, until the sediment concentration is 2 gm/l, at $z=4$ cm, and the variance is $20 \text{ cm}^2/\text{sec}^2$, at $z=2$ cm. The majority of the suspension events occur during the offshore decelerating and during the onshore accelerating phases of the flow. Figure V.6b is similar to Figure V.6a but shows the velocity versus acceleration of the free stream flow at the initiation of variance events, at $z=2$ cm, which are correlated to the suspension events. These events occur during the offshore decelerating and onshore accelerating phases of the flow, and slightly lead the suspension events.

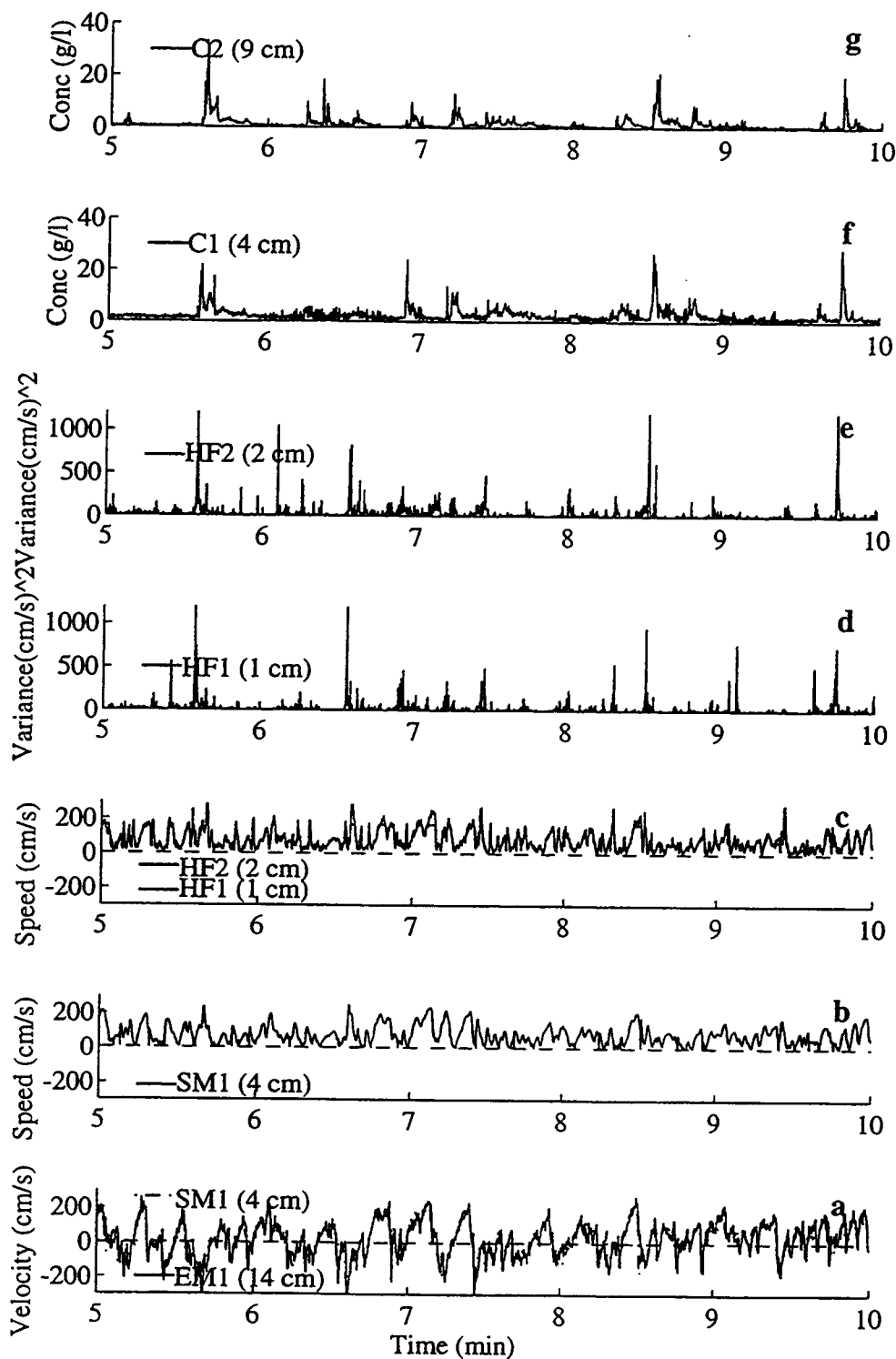


Figure V-4. Five minute time series, as recorded on 26 Sept 93, of: a) velocity at SM1 and EM1 b) speed at SM1 (rectified) c) speed at HF1 and HF2 d) variance partitioned at HF1 e) variance partitioned at HF2 f) concentration at C1 g) concentration at C2.

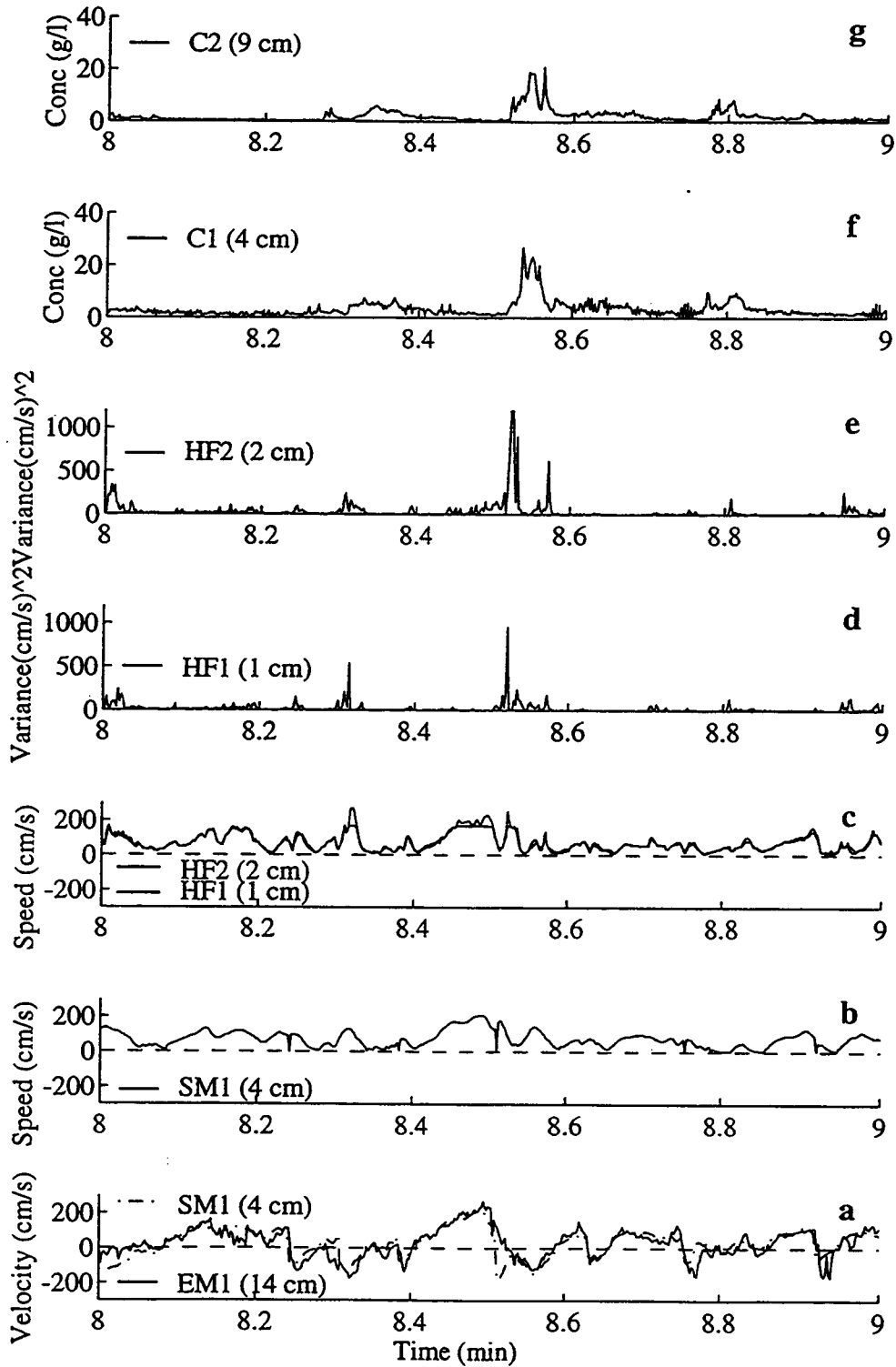


Figure V-5. One minute time series, as recorded on 26 Sept 93, of: a) velocity at SM1 and EM1 b) speed at SM1 (rectified) c) speed at HF1 and HF2 d) variance partitioned at HF1 e) variance partitioned at HF2 f) concentration at C1 g) concentration at C2.

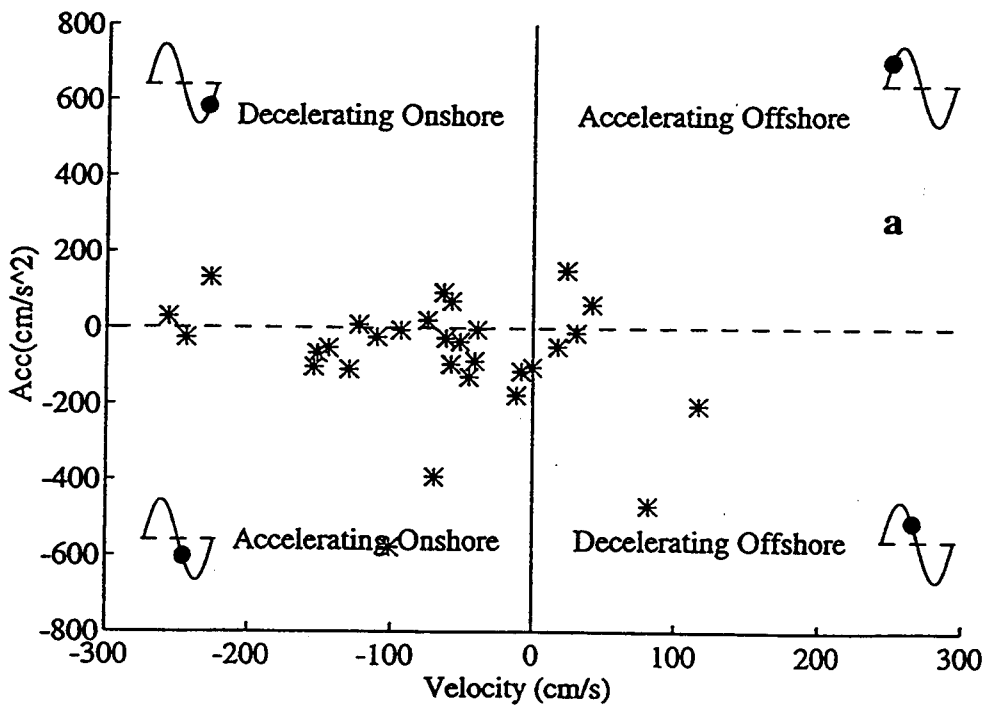
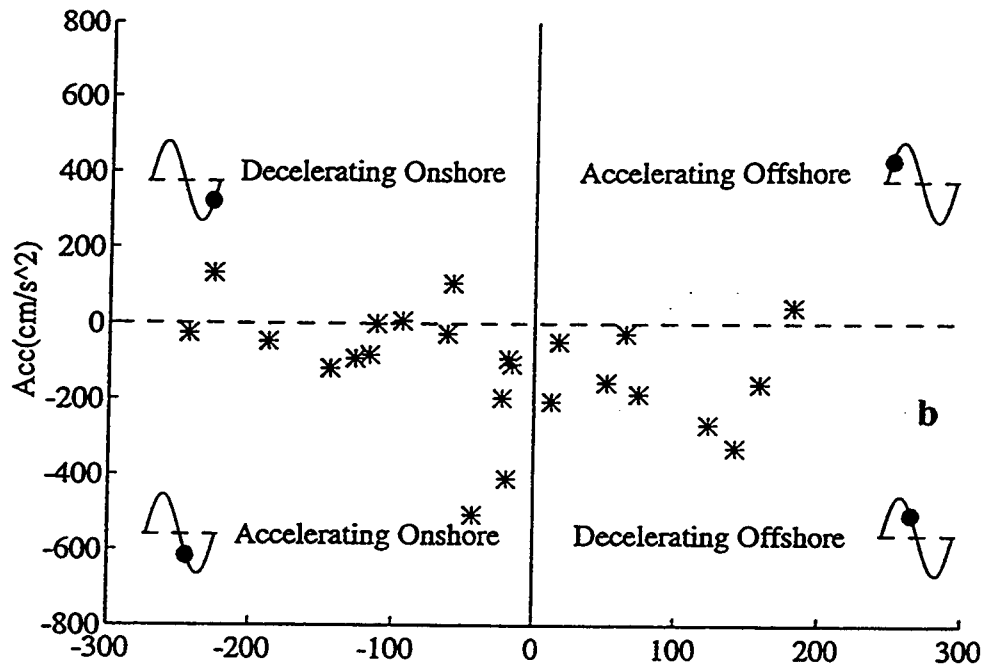


Figure V-6. Velocity versus acceleration of 0.5 Hz filtered EM1 sensor at the initiation of: a) suspended sediment events & b) variance events.

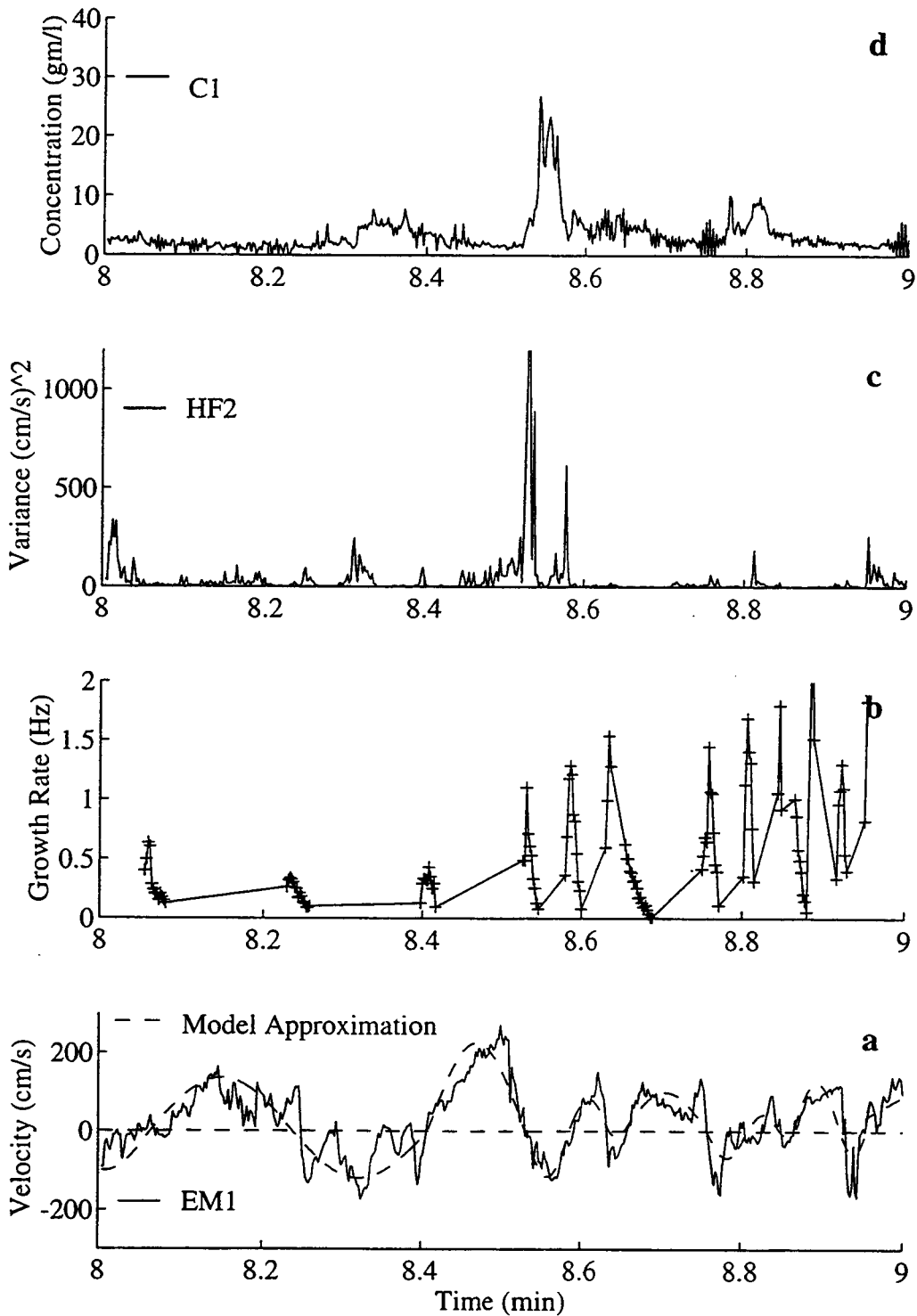


Figure V-7. Time series as recorded on 26 Sept 93 of: a) velocity of EM1 & boundary layer model approximation of EM1 b) predicted growth rates c) variance partitioned at HF2 d) concentration at C1.

The shear instability hypothesis predicts instabilities to occur when the velocity profile has an inflection point. Surf zone waves are asymmetric and consequently, the cross-shore deceleration is largest during the transition between offshore to onshore flow (from positive velocity to negative velocity). It is during this flow phase that we expect the shear in the bottom boundary layer to be the largest. If the shear instability hypothesis is valid, we expect the initiation of variance and suspension events to occur during the transition from offshore to onshore flow when the pressure gradients are the largest, Figures V.6a and 6b.

The imaginary frequencies, or growth rates, predicted by the linear instability analysis, when z_I is less than 6 cm, are presented in Figure V.7b. The suspended sediment concentration at $z=4$ cm is shown in Figure V.7d, the velocity variance at $z=2$ is shown in Figure 7c, and the free stream velocity and the modeled velocity (for the boundary layer model) at $z=14$ are presented in Figure V.7a. Instabilities are predicted more frequently than variance and suspension events occur. The prediction does not guarantee the instability development. The predicted instabilities from 8.6 to 9 min. are associated with low amplitude small period waves with rapid decelerations. Instability predictions during this time segment are results of the simplifying assumptions required for the bottom boundary layer model and for the linear time-independent instability model. Also, the predicted instabilities are of smaller magnitude or of shorter duration, than required to cause a perturbation to magnify 100 times. However, instability amplitudes are large enough to yield order of magnitude increases in initial perturbations. Consequently, the shear instability remains a viable hypothesis for the generation of large near bed velocities.

V.6 Summary

Field observations of sediment concentration in the surf zone can be episodic in nature, with rapid appearances and disappearances of high concentrations above the wave bottom boundary layer. One possible explanation for these events is a bottom boundary layer shear instability during flow reversal. The viability of this mechanism is evaluated with data from the inner surf zone of a dissipative Oregon beach. Data includes paired current meter velocities and suspended sediment concentrations at $z=4,9$, and 14 cm above the bed; and hot film anemometer speeds at $z=1$ and 2 cm.

Each 2000 Hz hot film time series is variance partitioned into an 8 Hz variance time series by combining the variance of subsequent 1/8 sec intervals. This variance time series characterizes levels of high frequency fluctuations contained within each segment. The episodic time series is correlated to the suspension events and leads by 0.75 secs.

The boundary layer leads the free stream and results in an inflection point in the vertical cross-shore velocity profile during flow deceleration, reversal, and subsequent acceleration. If the shear contained within the profile during this phase of the flow is large enough, small perturbations may become unstable and grow exponentially in time. Plots of the free stream velocity versus acceleration at the initiation of variance and sediment suspension events show the majority of the events occur during the transition to onshore flow. Wave asymmetries cause the cross-shore decelerations to be larger during the transition to onshore flow.

The existence of instabilities during the period of flow reversal was modeled through a simple linear instability analysis of a time varying bottom boundary layer. At each time, small perturbations were superimposed on a modeled boundary layer cross-shore velocity profile and instability growth rates were predicted over wavelengths of 2 to 50 cm. Predicted growth rates are large enough to yield an order of magnitude increase in initial perturbation amplitudes. Instabilities are predicted more frequently than variance and suspension events occur. Some of the instabilities which occur under small waves may be attributed to the simplifying assumptions required for the bottom boundary layer model and for the linear time-independent instability model. Nevertheless, the hypothesis is encouraging as the instabilities have reasonable wavelengths and growth rates and occur during the time of flow reversal.

The ultimate goals of this ongoing project are to examine the link between turbulence generation and sediment suspension. Future investigations will utilize more sophisticated bottom boundary layer models, explore time-dependent numerical instability models and compare predicted instability wave numbers and frequencies to an array of the hot films.

CHAPTER VI: CONCLUSIONS

This thesis characterizes the dynamics of the surf zone wave bottom boundary layer using a combination of theory and field observations. The main conclusions can be summarized from each chapter as follows:

- 1) The linearized one dimensional time-dependent wave bottom boundary layer equation was solved analytically assuming a linear time-dependent eddy viscosity model. Predictions of the velocity structure and bed shear velocity are in good agreement with the laboratory data. Comparisons of the model with field observations show reasonable estimates of the rms velocity distribution. However, the model is limited by assuming zero velocity at the bed and that turbulence generation is solely due to bottom shear. The model shows that under the presence of skewed and asymmetric waves the energy of the cross-shore velocity in the higher harmonics can be as large as 30% of the fundamental.
- 2) Field observations from an North Carolina, Outer Banks, investigation are among the first coherent examinations of the vertical and temporal structure of the nearshore wave bottom boundary layer. The observations showed a decrease in rms velocity and an increase in phase with proximity to the bed, characteristic of simple theoretical predictions. However, smaller vertical shears (by a factor of 5) and smaller phase shifts (by a factor of 3) of the cross-shore velocity structure are indicative of more rapid turbulence generation than predictions by simple eddy viscosity models. The observations illustrate the complex dynamics of wave bottom boundary layers under significant sediment response and bed mobilization. The amplitude and phase structure of the wave bottom boundary layer as a function of frequency suggests that the region is nonlinear.
- 3) Measurements of the turbulent kinetic energy in the wave bottom boundary layer indicate a highly intermittent structure. Through most phases of the cross-shore flow, the turbulent kinetic energy increases linearly from the bed. However, enhanced turbulence levels are observed under the larger wave crests. These occasions of enhanced turbulence are well correlated to active sediment suspension events. The stress, as estimated by an eddy viscosity model, does not appear to be well correlated to the turbulence levels or suspended sediment concentration, and instead oscillates with the free stream wave field. Estimates of dissipation rates are shown to be two orders of magnitude less than those observed in an actively breaking surf zone wave, one to two orders of magnitude greater

than those observed in the deep ocean boundary layer, and one to three orders of magnitude greater than those observed in a continental shelf current boundary layer.

4) An Oregon coast field experiment showed an intermittent high frequency velocity variance structure which was correlated to suspended sediment events. A linear shear instability analysis determined that during the period of flow reversal, there exists a potential for generating turbulence due to shear instabilities of the vertical structure of cross-shore velocity profile. Less than 25% of the velocity variance and concentration events are at the correct flow phases to be due to shear instabilities. It is not possible to determine if the other 75% of the events are a result of shear instabilities generated elsewhere and advected past the instrument array, or a result of some other generation mechanism such as advected turbulence due to broken waves or bottom generated turbulence.

In addition to the above conclusions, this work identifies the potential for several future directions. Specifically, the analytic model in Chapter II would benefit from an investigation of the role of convective accelerations ($u\partial u/\partial x$). Chapter III highlights the added complexity of wave bottom boundary layer dynamics over erodable beds. Future investigations could include: 1) the effect of of time varying bed elevation on the root-mean-square velocity statistics at fixed instrument locations and 2) the modelling of the wave bottom boundary layer under a continuum of sediment-induced stratification. In Chapter IV, no separation is made between the response of the boundary layer and suspended sediment levels to broken and unbroken waves. As a first step, video observations of the free surface should be compared with the sediment and turbulence observations shown in this thesis. Better prediction of shear instabilities in Chapter V could be achieved with a numerical linear analysis and/or a fully numerical nonlinear analysis. Finally, all of the observations presented in this thesis were collected at a single location. Future investigations which examine the evolution of the wave bottom boundary layer across the surf zone will further our understanding of the nearshore boundary layer dynamics.

BIBLIOGRAPHY

- Anis, A., and J.N. Moum, Surface wave-turbulence interactions: Scaling $\varepsilon(z)$ near the sea surface, *Journal of Physical Oceanography*, 25, 2025-2045, 1995.
- Bagnold, R.A., Mechanics of marine sedimentation, in *The Sea*, edited by M.N. Hill, pp. 507-528, Wiley-Interscience, New York, 1963.
- Baillard, J.A., and D.L. Inman, An energetics bedload transport model for a plane sloping beach: Local transport, *Journal of Geophysical Research*, 86, 2035, 1981.
- Batchelor, G.K., *An Introduction to Fluid Dynamics*, 615 pp., Cambridge University Press, Cambridge, 1967.
- Beach, R.A., and R.W. Sternberg, Suspended sediment transport in the surf zone: Response to cross-shore infragravity motion, *Marine Geology*, 80, 61-79, 1988.
- Beach, R.A., and R.W. Sternberg, Suspended sediment transport in the surf zone: Response to incident wave and longshore current interaction, *Marine Geology*, 108, 275-294, 1992.
- Beach, R.A., R.W. Sternberg, and R. Johnson, A fiber optic sensor for monitoring suspended sediment, *Marine Geology*, 103, 513-520, 1992.
- Blackwelder, R.F., and R.E. Kaplan, On the wall structure of the turbulent boundary layer, *Journal of Fluid Mechanics*, 76, 89-112, 1976.
- Bowen, A.J., Simple models of nearshore sedimentation; beach profiles and longshore bars, in *The Coastline of Canada*, edited by S.B. McCann, pp. 1-11, Geological Survey of Canada, 1980.
- Bowen, A.J., and R.A. Holman, Shear instabilities of the mean longshore current, 1. Theory, *Journal of Geophysical Research*, 94 (C12), 18,023-18,030, 1989.
- Conley, D.C., and D.L. Inman, Field observations of the fluid-granular boundary layer under near-breaking waves, *Journal of Geophysical Research*, 97 (C6), 9631-9643, 1992.
- Foster, D., R. Holman, and R. Beach, Correlation between sediment suspension events and shear instabilities in the bottom boundary layer of the surf zone, in *Coastal Dynamics '94*, ASCE, Barcelona, Spain, 1994.
- George, R., R.E. Flick, and R.T. Guza, Observations of turbulence in the surf zone, *Journal of Geophysical Research*, 99 (C1), 801-810, 1994.
- Grant, W.D., and O.S. Madsen, Combined wave and current interaction with a rough bottom, *Journal of Geophysical Research*, 84 (C4), 1797-1808, 1979.
- Gross, T.F., A.J. Williams, and E.A. Terray, Bottom boundary layer spectral dissipation estimates in the presence of wave motions, *Continental Shelf Research*, 14 (10/11), 1239-1256, 1994.

- Hanes, D.M., Intermittent sediment suspension and its implications to sand tracer dispersal in wave-dominated environments, *Marine Geology*, 81, 175-183, 1988.
- Hino, M., M. Kashiwayanagi, A. Nakayama, and T. Hara, Experiments on the turbulent statistics and the structure of a reciprocating oscillatory flow, *Journal of Fluid Mechanics*, 131, 363-400, 1983.
- Huntley, D.A., and D.M. Hanes, Direct measurements of suspended sediment transport, in *Coastal Sediments*, pp. 723-737, ASCE, New Orleans, 1987.
- Jaffe, B.E., R.W. Sternberg, and A.H. Sallenger, The role of suspended sediment in shore-normal beach profile changes, in *Proceedings of the 19th International Conference on Coastal Engineering*, pp. 1983-1996, ASCE, Houston, Texas, 1984.
- Jensen, B.L., B.M. Sumer, and J. Fredsoe, Turbulent oscillatory boundary layers at high Reynolds numbers, *Journal of Fluid Mechanics*, 206, 265-298, 1989.
- Jonsson, I.G., and N.A. Carlsen, Experimental and theoretical investigations in an oscillatory turbulent boundary layer, *Journal of Hydraulic Research*, 14, 45-60, 1976.
- Justesen, P., Prediction of turbulent oscillatory flow over rough beds, *Coastal Engineering*, 12, 257-284, 1988.
- Lueck, R.G., Heated anemometry and thermometry in water, Ph.D. thesis, University of British Columbia, 1979.
- Rayleigh, L., and J.W. Strutt), On the stability, or instability, of certain fluid motions, *Proceedings of the London Mathematical Society*, 11, 57-70, 1880.
- Sleath, J.F.A., Turbulent oscillatory flow over rough beds, *Journal of Fluid Mechanics*, 182 (369-410), 1987.
- Sleath, J.F.A., Seabed boundary layers, in *Ocean Engineering Science*, edited by B.L.a.D.M. Hanes, pp. 693-728, John Wiley, New York, 1990.
- Smith, J.D., Modeling of sediment transport on continental shelves, in *Marine Modelling*, edited by I.N.M. E.D. Goldberg, J.J. O'Brien, and J.H. Steele, pp. 539-577, John Wiley, New York, 1977.
- Tennekes, H., and J.L. Lumley, *A First Course in Turbulence*, 300 pp., The MIT Press, Cambridge, Mass., 1972.
- Thornton, E.B., and R.T. Guza, Transformation of wave height distribution, *Journal of Geophysical Research*, 88 (C10), 5925-5938, 1983.
- Trowbridge, J., and O.S. Madsen, Turbulent wave boundary layers 1. Model formulation and first-order solution, *Journal of Geophysical Research*, 88 (C5), 7989-7997, 1984.
- Trowbridge, J.H., and Y.C. Agrawal, Glimpses of a wave boundary layer, *Journal of Geophysical Research*, 100 (C10), 20,729-20,743, 1995.
- Wallace, J.M., Empirical orthogonal representation of time series in the frequency domain. Part II: Application to the study of tropical wave disturbances, *Journal of Applied Meteorology*, 11 (6), 893-900, 1972.

APPENDICES

APPENDIX A

The second formulation bounds the solution with a zero vertical gradient at some elevation outside the boundary layer. The boundary and initial conditions are defined to be

$$\begin{aligned}\frac{\partial \hat{u}(d,t)}{\partial z} &= 0 \\ \hat{u}(z_o,t) &= 0 \\ \hat{u}(z,t_o) &= \hat{r}(z)\end{aligned}\tag{A-1 a, b\& c}$$

where d is a given elevation outside the boundary layer, z_o is the bed roughness, t_o is the initial time, and $r(z)$ is the initial condition. The same separable eddy viscosity model as given in (4) is used. In this formulation, a variable transformation is not necessary as the boundary conditions are time independent. As before, separate the homogeneous and non-homogeneous terms of (1),

$$\frac{\partial \hat{u}_2}{\partial t} - g \frac{dp}{dz} \frac{\partial \hat{u}_2}{\partial z} - gp \frac{\partial^2 \hat{u}_2}{\partial z^2} = \frac{du_\infty}{dt}\tag{A-2}$$

where u_2 is the complete solution for formulation two. The non-homogeneous term, simpler than in formulation one, is independent of z and the homogeneous equation is identical to QE (10)

$$\frac{\partial u_{2p}}{\partial t} - p'(z)g(t) \frac{\partial u_{2p}}{\partial z} - p(z)g(t) \frac{\partial^2 u_{2p}}{\partial z^2} = 0\tag{A-3}$$

with boundary conditions of

$$\begin{aligned}\frac{\partial u_{2p}(d,t)}{\partial z} &= 0 \\ u_{2p}(z_o,t) &= 0 \\ u_{2p}(z,t_o) &= r(z)\end{aligned}\tag{A-4}$$

Solution Formulation Two

As in the previous derivation, solve for the particular solution, $u_{p2} = \Psi(z)T(t)$ with the separation of variables technique. In this formulation, the determination of the eigenvalue, λ , is determined by searching a combination of zero and first order Bessel functions for zero crossings

$$J_0(2\lambda_{2n}z_0^{1/2})Y_1(2\lambda_{2n}d^{1/2}) - J_1(2\lambda_{2n}d^{1/2})Y_0(2\lambda_{2n}z_0^{1/2}) = 0 \quad (\text{A-5})$$

$$u_{2p}(z,t) = \sum_{n=1}^{\infty} b_{2n} \left(Y_0(2\lambda_{2n}z_0^{1/2})J_0(2\lambda_{2n}z^{1/2}) - J_0(2\lambda_{2n}z_0^{1/2})Y_0(2\lambda_{2n}z^{1/2}) \right) e^{-\lambda_{2n}^2 \int_0^t g(\tau) d\tau} \quad (\text{A-6})$$

where the integration constant and orthogonality condition have the same form as (II-19) and (II-20), respectively,

$$b_{2n} = \frac{1}{c_{2n}} \int_{z_0}^d h(z) \Psi_{2n}(z) dz$$

$$\int_{z_0}^d \Psi_{2n}(z) \Psi_{2j}(z) dz = \begin{cases} 0 & \text{if } j \neq n \\ c_{2n} & \text{if } j = n \end{cases}$$

The non homogeneous component of the solution given by

$$\frac{\partial u}{\partial t} = \frac{\partial}{\partial z} \left(v, \frac{\partial u}{\partial z} \right) + F_2(t) \quad (\text{A-7})$$

where the forcing term, $F_2(t)$ is

$$F_2(t) = \frac{du_{\infty}}{dt}. \quad (\text{A-8})$$

Assume the same series solution form of (II-23) and substitute into (II-39)

$$\sum_{n=1}^{\infty} \dot{a}_{2n} \Psi_{2n} = g \sum_{n=1}^{\infty} a_{2n} (p \Psi_{2n}') + F_2(t) \quad (\text{A-9})$$

where ' denotes a derivative with respect to z and $\dot{}$ denotes a derivative with respect to time. Assume F may be represented as

$$F_2(z,t) = \sum_{n=1}^{\infty} F_{2n}(t) \Psi_{2n}(z) \quad (\text{A-10})$$

such that F_{2n} is

$$F_{2n}(t) = \frac{F_2(t)}{c_{2n}} \int_{z_0}^d \Psi_{2n}(z) dz \quad (\text{A-11})$$

Following the same procedure as given in section 2, the complete solution of (A-1) is

$$\hat{u}_2(z,t) = \sum_{n=1}^{\infty} a_{2n}(t) \Psi_{2n}(z) \quad (\text{A-12})$$

recall from (II-29) and (II-31)

$$a_{2n}(t) = a_{2n}(0) e^{-\lambda_{2n}^2 \int_0^t g(\tau) d\tau} + \int_0^t F_{2n}(\sigma) e^{-\lambda_{2n}^2 \int_{\sigma}^t g(\tau) d\tau} d\sigma$$

$$\Psi_{2n}(z) = Y_0(2\lambda_{2n}z_0^{1/2}) J_0(2\lambda_{2n}z^{1/2}) - J_0(2\lambda_{2n}z_0^{1/2}) Y_0(2\lambda_{2n}z^{1/2})$$

Both models use the identical shear velocity formulation as given in section 5. The eigenvalues in second formulation are less than in formulation one, resulting in a much slower rate of decay than for that of formulation one. Also, because of the second order nature of the upper boundary condition, convergence errors may occur at large times. As such, we suggest formulation one.

1979).

APPENDIX B

The effect of sediment on the response of the hot film was quantified with the following simple heat transfer theory. The power supplied to the hot film is assumed to be balanced by the conduction and forced convection heat transfer from the film per unit time (Lueck,

$$\text{Power} = \frac{V^2}{R} = \pi k l \Delta \theta \text{Nu}, \quad (\text{B-1})$$

where the V is the output voltage, R is the resistance of the hot film, k is the thermal conductivity of the ambient fluid, $\Delta \theta$ is the overheat temperature, l ($=2.03$ mm) is the length of the hot film probe, and Nu is the non-dimensional Nusselt number representing the dimensionless temperature gradient at the film surface. The Nusselt number for flow around a cylinder is assumed to be (Hinze, 1975)

$$\text{Nu} = 0.42 \text{Pr}^{1/2} + 0.57 \text{Pr}^{1/2} \text{Re}^{1/2} \quad (\text{B-2})$$

where, $\text{Pr} = \frac{\nu}{\kappa}$ is the Prandtl number, $\text{Re} = \frac{ud}{\nu}$ is the Reynolds number, $\kappa = \frac{k}{\rho C_p}$ is the

thermal diffusivity, ν is the kinematic viscosity, ρ is the fluid density, C_p is the specific heat of the fluid, and d ($=0.152$ mm) is the diameter of the hot film. The theoretical output voltage of a hot film sensor in a well mixed sediment laden fluid normalized by that in a sediment-free seawater is

$$\frac{V_{ws}}{V_w} = \sqrt{\frac{k_{ws} \text{Nu}_{ws}}{k_w \text{Nu}_w}}. \quad (\text{B-3})$$

The physical properties for seawater(_w), sediment(_s), and seawater with sediment (_{ws}) are given in Table B-1. The relative output voltage for the hot film in a maximum 160 g/l sediment laden seawater is 1.05 and is largely insensitive to velocity variations, Figure B-1.

	Density ρ (kg/m ³)	Thermal Conductivity k (W/m°C)	Kinematic Viscosity ν (m ² /s)	Specific Heat C_p (Ws/kg°C)
seawater	1025	.6	1.3e-6	820
sediment	2650	5.7**	1.3e-6	4200
seawater with sediment	$\phi\rho_s + (1-\phi)\rho_w$	$k_w \frac{k_s + 2k_w - 2\phi(k_w - k_s)}{k_s + 2k_w + \phi(k_w - k_s)}$ *	1.3e-6	$\phi C_{p_s} + (1-\phi)C_{p_w}$

Table B-1. Assumed physical properties of seawater and sediment. ϕ is the relative sediment volume and ϕ is the relative sediment weight. (* Cheng and Vachon, 1970; ** CRC Handbook of Physics and Chemistry)

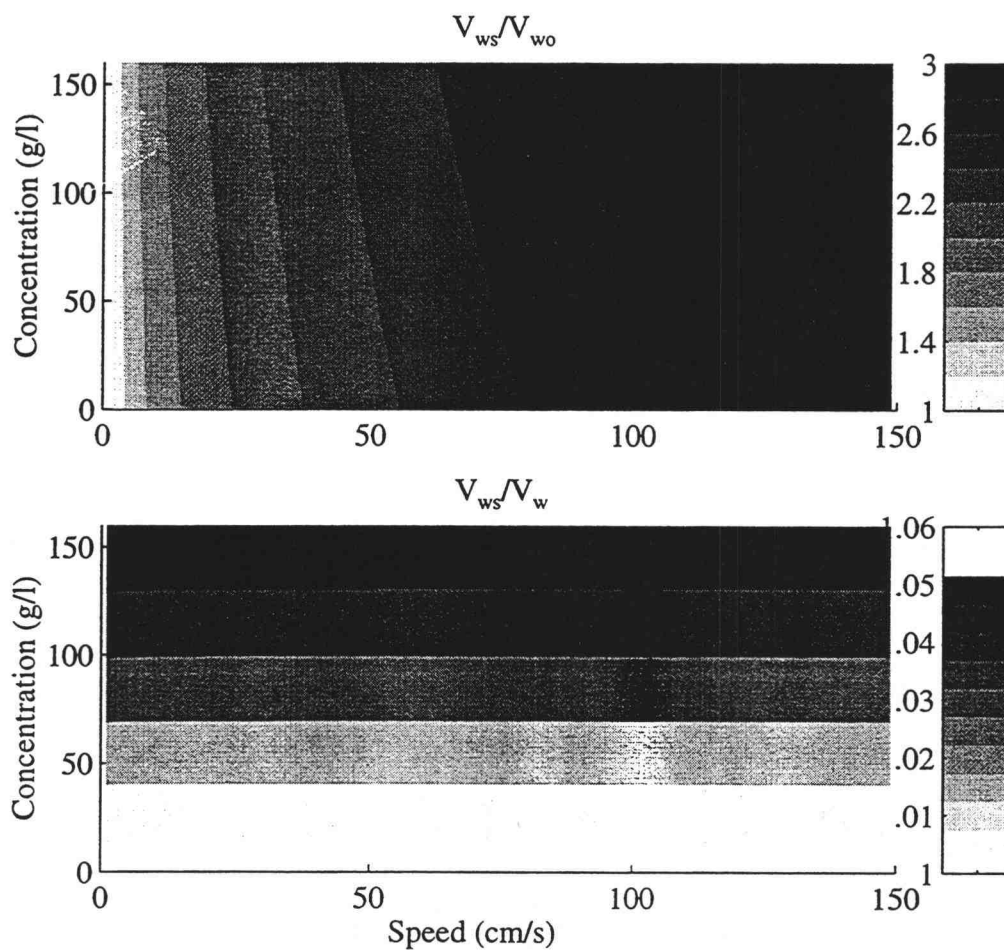


Figure B-1. The relative increase in output voltage of theoretical hot film probe in seawater and sediment with given concentration to output voltage in seawater only at zero fluid speed (top panel) and the relative increase in output voltage of theoretical hot film probe in seawater and sediment with given concentration to output voltage in seawater only at each speed (bottom panel).

APPENDIX C

All wave bottom boundary layer velocity measurements were made with TSI model 1755 constant temperature cylindrical quartz coated hot film anemometer probes. The frequency response of each hot film was determined by considering the effect of the unsteady nature of the flow, the thermal boundary layer, and the quartz film coating.

According to Lueck [1979], the viscous boundary layer over a cylindrical probe may be considered to exhibit quasi-steady behavior when

$$\frac{\omega d}{u} < 5 \quad (C-1)$$

where ω is the wave frequency, d ($=0.152$ mm) is the film diameter, and u is the wave velocity. Substituting the film diameter into (C-1) yields

$$\frac{\omega}{u} < 33,000 \quad (C-2)$$

Considering a conservative upper wave frequency limit of 1 Hz, (C-1) would be satisfied for wave velocities of greater than 3.03×10^{-5} m/s. Therefore, it is assumed that the probe response is quasi-steady.

The high frequency cut off of the hot film to the thermal boundary layer is estimated with (Fingerson and Freymouth, 1983)

$$f_{\delta} \approx \frac{u}{2\pi d} \quad (C-3)$$

where f_{δ} is the high frequency cut off response of the film. For the films used in these investigations, the frequency response of the film, as estimated in (C-3), decreases linearly with the fluid velocity is $f_{\delta} \approx 1048u$. According to (C-3), the velocity would have to be greater than 9.5 cm/s to maintain a minimum frequency response of 100 Hz. However, the observations have shown that under all velocities the signal to noise ratio remains high until 150 Hz. In Chapter V, the highest frequency used in calculations is 100 Hz.